STATE OF CALIFORNIA • DEPARTMENT OF TRANSPORTATION

TECHNICAL REPORT DOCUMENTATION PAGE

TR-0003 (REV 04/2024)

1. REPORT NUMBER CA25-4417	2. GOVERNMENT ASSOCIATION NUMBER	3. RECIPIENT'S CATALOG NUMBER
4. TITLE AND SUBTITLE New Near-Fault Adjustment Factors for Caltrans Seismic Design Criteria (SDC)		5. REPORT DATE December 2025
		6. PERFORMING ORGANIZATION CODE
7. AUTHOR Silvia Mazzoni, Esra Zengin, Mahdi Bahrampouri, Yousef Bozorgnia		8. PERFORMING ORGANIZATION REPORT NO. GIRS-2025-04
9. PERFORMING ORGANIZATION NAME AND ADDRESS Natural Hazards Risk and Resiliency Research Center (NHR3), Department of Civil and Environmental Engineering University of California, Los Angeles 404 Westwood Plaza, Los Angeles, CA 90095		10. WORK UNIT NUMBER
		11. CONTRACT OR GRANT NUMBER 65A0774 TO 010
12. SPONSORING AGENCY AND ADDRESS California Department of Transportation 1120 N St., Sacramento, CA 95814		13. TYPE OF REPORT AND PERIOD COVERED Final Report 4/02/2024 - 2/28/2025
		14. SPONSORING AGENCY CODE

15. SUPPLEMENTARY NOTES

16. ABSTRACT

This report covers analyses of Caltrans' near-fault adjustment factors as recommended in the Caltrans Seismic Design Criteria. The report has two large chapters. Chapter 1 builds on prior the University of California Los Angeles studies that performed probabilistic seismic hazard analyses at numerous California sites across a range of return periods and multiple site classes. Using that dataset, the chapter develops simplified, distance- and period-dependent models that quantify directivity amplification of elastic response spectra statewide. Because many bridges are expected to respond inelastically during major earthquakes, the models are further adapted to capture period elongation consistent with typical bridge ductility demands. In Chapter 2, the impacts of the near-fault directivity factors proposed in Chapter 1 were evaluated on the seismic performance of two Caltrans ordinary long-span bridge configurations: a single-column bent and a two-column bent. Using nonlinear time history analysis (NTHA), three-dimensional bridge models were evaluated under 20 bidirectional near-fault ground motions, scaled to three different target spectra. Analyses were performed for return periods of 1000 and 2475 years at two sites, Los Angeles and Oakland, and included an investigation of the influence of ground-motion directionality on bridge responses. Finally, the results obtained from elastic and inelastic analyses of single-degree-of-freedom systems, and NTHA were compared.

17. KEY WORDS Near-fault fault adjustment factors, ground motion directionality, probabilistic seismic hazard analysis, nonlinear time history analysis, inelastic response spectra	18. DISTRIBUTION STATEMENT No Restrictions	
19. SECURITY CLASSIFICATION *(of this report)* Unclassified	20. NUMBER OF PAGES 132	21. COST OF REPORT CHARGED

Reproduction of completed page authorized.

DISCLAIMER STATEMENT

Cal Poly

Caltech

SCEC
AN NSF+USGS CENTER

UC Irvine

UCLA

UC Santa Barbara

USC

New Near-Fault Adjustment Factors for Caltrans Seismic Design Criteria (SDC)

Silvia Mazzoni, Esra Zengin,
Mahdi Bahrampouri, Yousef Bozorgnia

Natural Hazards Risk and Resiliency Research Center (NHR3),
Department of Civil and Environmental Engineering
University of California, Los Angeles

A report on research supported by
State of California, Department of Transportation (Caltrans)

Report GIRS-2025-04

DOI: 10.34948/N3S88X

University of California, Los Angeles (headquarters)

Natural Hazards Risk & Resiliency Research Center

The B. John Garrick Institute for the Risk Sciences

New Near-Fault Adjustment Factors for Caltrans Seismic Design Criteria (SDC)

Silvia Mazzoni, Esra Zengin,
Mahdi Bahrampouri, Yousef Bozorgnia
Natural Hazards Risk and Resiliency Research Center (NHR3),
Civil and Environmental Engineering Department
University of California, Los Angeles

A report on research conducted with support from
State of California, Department of Transportation (Caltrans)

Report GIRS-2025-04
DOI: 10.34948/N3S88X

Natural Hazards Risk and Resiliency Research Center
B. John Garrick Institute for the Risk Sciences
University of California, Los Angeles (Headquarters)

December 2025

CONTENTS

1. NEW NEAR-FAULT ADJUSTMENT FACTORS FOR CALTRANS SEISMIC DESIGN CRITERIA (SDC) CONSIDERING ELASTIC AND INELASTIC RESPONSE SPECTRA 1

TABLES

FIGURES

ACKNOWLEDGMENTS

This study was supported by the California Department of Transportation (Caltrans) and coordinated by the Natural Hazards Risk and Resiliency Research Center (NHR3) headquartered at UCLA through the Pacific Earthquake Engineering Research Center (PEER). The support is gratefully acknowledged. The findings, conclusions, or recommendations in this publication are those of the authors and do not necessarily represent those of the sponsor, the B. John Garrick Risk Institute, the NHR3, or the Regents of the University of California.

The authors would like to thank Tom Shantz, Kyungtae Kim, and Sharon Yen of Caltrans, and Professor Saiid Saiidi (Chapter 2), for their helpful discussions and valuable insights related to this research.

ORGANIZATION OF THE REPORT

This report covers analyses of Caltrans' near-fault adjustment factors as recommended in the Caltrans Seismic Design Criteria. The report has two large chapters.

Chapter 1 builds on prior UCLA studies that performed probabilistic seismic hazard analyses (PSHA) at numerous California sites across a range of return periods and multiple site classes. Using that dataset, the chapter develops simplified, distance- and period-dependent models that quantify directivity amplification of elastic response spectra statewide. Because many bridges are expected to respond inelastically during major earthquakes, the models are further adapted to capture period elongation consistent with typical bridge ductility demands.

In Chapter 2, the impacts of the near-fault directivity factors proposed in Chapter 1 were evaluated on the seismic performance of two Caltrans ordinary long-span bridge configurations: a single-column bent and a two-column bent. Using nonlinear time history analysis (NTHA), three-dimensional bridge models were evaluated under 20 bidirectional near-fault ground motions, scaled to three different target spectra. Analyses were performed for return periods of 1000 and 2475 years at two sites, Los Angeles and Oakland, and included an investigation of the influence of ground-motion directionality on bridge responses. Finally, the results obtained from elastic and inelastic analyses of single-degree-of-freedom (SDOF) systems, and NTHA were compared.

1. NEW NEAR-FAULT ADJUSTMENT FACTORS FOR CALTRANS SEISMIC DESIGN CRITERIA (SDC) CONSIDERING ELASTIC AND INELASTIC RESPONSE SPECTRA

by Silvia Mazzoni, Mahdi Bahrampouri, and Yousef Bozorgnia

1.1. ABSTRACT

Structures located near active fault ruptures are exposed to amplified ground shaking caused by rupture directivity and pulse-like ground motion effects. Since 1992, Caltrans Seismic Design Criteria (SDC) have included Near-Fault Adjustment Factors (NFAFs) to address these effects, but only limited updates have been made over the past three decades. This study provides updated recommendations for NFAFs based on recent advances in seismic hazard modeling, ground motion databases, and structural response analysis. A comprehensive statewide probabilistic seismic hazard analysis (PSHA) incorporating directivity was conducted using UCERF-3 fault sources, NGA-West2 ground motion models, and three directivity models, applied to more than 19,000 sites across California. Simplified distance- and period-dependent models were developed from PSHA deaggregation results to characterize directivity amplification, with magnitude binning applied to improve accuracy for large events. Inelastic response effects were incorporated using new models based on inelastic response spectra and pulse-type motions from NGA-West2 data, accounting for period elongation and ductility levels consistent with bridge performance. The recommended updated adjustment factors extend application distances to 35 km, refine period thresholds for both elastic and inelastic response, and provide Caltrans with flexible implementation options: (1) simplified distance-based adjustments for standard design, (2) magnitude-dependent adjustments for critical structures, and (3) a site-specific interactive tool developed under the UCLA NHR3 program. These updates provide a more scientifically robust, practical, and implementable framework for future revisions of the Caltrans Seismic Design Criteria.

1.2. EXECUTIVE SUMMARY

Ground shaking near rupturing faults has been shown to be significantly more intense—and more damaging—than shaking observed at greater distances. Since 1992, Caltrans has accounted for near-fault effects by increasing the design response spectrum using period-dependent adjustment factors for sites within 15 km of an active fault. These provisions have seen only minor revisions over the past three decades.

Given recent developments in ground motion databases, seismic hazard modeling, and structural response analysis, this project re-evaluates the current Caltrans Near-Fault Design Criteria and provides updated recommendations. New insights were drawn from recent research projects on the statewide probabilistic seismic hazard analysis (PSHA) incorporating near-fault directivity effects, as well as recent research on inelastic structural response to near-fault ground motions. The goal of the current project was to develop an improved "near-fault adjustment factor" model that engineers can implement easily, while still maintaining scientific rigor.

The updated adjustment factors are based on two major steps: (i) updating the Caltrans near-fault adjustment factors based on linear elastic response spectra employing comprehensive data and models for directivity of ground motion, and (ii) modifying the adjustment factor developed in step (i) to incorporate the general behavior of inelastic structural response.

The technical implementation of these two steps is described below.

Task 1: Simplified Directivity Model Using the UCLA NHR3 Interactive 2023 Map

This study builds on the statewide directivity-inclusive PSHA developed by UCLA NHR3 (Al Atik et al., 2022, Al Atik et al., 2023, Mazzoni et al., 2023), which provided directivity-adjusted hazard data for over 19,000 sites across California. The statewide hazard calculations incorporated:

- UCERF-3 seismic source model.
- NGA-West2 ground motion models applied with and without directivity.
- Directivity modeled using three established models:
    - **CS13 (Chiou & Spudich 2013)**: physically-based rupture geometry model;
    - **BS13 (Bayless & Somerville 2013)**: simplified empirical model;
    - **BSS20 (Bayless et al. 2020)**: narrowband directivity model incorporating finite-fault simulations.
- Directivity model weights assigned as: CS13 (50%), BS13 (25%), and BSS20 (25%).

Hazard calculations were performed for multiple oscillator periods (0.5 s to 10 s), eight return periods, and full site condition coverage (Vs_{30} = 180 to 1100 m/s).

Directivity amplification factors were computed at each site as the ratio of PSA values with and without directivity effects. Selection filters excluded sites where subduction contributed more than 30% of the total hazard, as well as offshore sites. Deaggregation analysis was performed to extract both modal and mean magnitude-distance (M–R) pairs characterizing the controlling seismic hazard at each location.

Using the statewide NHR3 dataset, simplified functional models were then developed that relate directivity amplification to rupture distance and oscillator period. Magnitude binning (0.5-unit intervals from M6.0 to M8.5) was applied to develop magnitude-dependent models. The resulting functional form employs a plateau amplification within near-fault distances, transitioning logarithmically with distance — balancing physical realism and engineering practicality.

Task 2: Incorporation of Inelastic Response Effects

The second phase of the project addressed the influence of inelastic structural response on near-fault amplification, leveraging prior research (GIRS-2023-01; Bahrampouri et al., 2024) on inelastic ground motion models using NGA-West2 data. This work incorporated:

- Inelastic response spectra for ductility levels $\mu = 2, 4, 6$, and 8;
- Empirical period elongation models to capture nonlinear behavior under pulse-like motions;
- Pulse-period distributions calibrated with 137 pulse-like NGA-West2 recordings;
- Development of period- and ductility-dependent adjustment factors to translate elastic directivity amplification into corresponding inelastic amplification.

The inelastic analysis revealed that while nonlinearity reduces the narrowband amplification seen in elastic response, it shifts amplification effects toward shorter periods. Consequently, the lower-bound period threshold for inelastic directivity amplification was adjusted from 0.75 s to 0.5 s—aligning with the existing Caltrans SDC lower bound.

Summary of Proposed Models

Three directivity amplification models are recommended for Caltrans implementation, depending on project type and design stage:

1. **Updated Simplified Near-Fault Adjustment Factors:**
    - Period- and distance-dependent amplification, valid up to 3 s.
    - Magnitude-independent for ease of routine design application.
    - Distance threshold extended to 35 km.
    - Period threshold set to 0.75 s for elastic spectra and 0.5 s for inelastic spectra.
2. **Magnitude-Dependent Models:**
    - Magnitude binning included for improved precision in large-magnitude events.
    - Suitable for critical infrastructure, long-span bridges, or detailed design reviews.
3. **Site-Specific Directivity Tool (UCLA NHR3 Platform):**
    - Enables custom response spectra based on location, magnitude, distance, Vs_{30}, and fault geometry.
    - This method allows the user to specify the location of a bridge, the site class, and return period to obtain site-specific amplification values. This method should be used when bridge characteristics are outside of the allowable range of the simplified models, such as long-period bridges (T>3 seconds) very close to the San Andreas fault.
    - Publicly accessible: https://www.risksciences.ucla.edu/nhr3/california-directivity

Overall Contributions

This study integrates recent scientific advances across PSHA, directivity modeling, nonlinear response behavior, and period elongation to provide a modernized and scientifically robust update to Caltrans Near-Fault Adjustment Factors. The proposed models preserve practical simplicity for routine use, while offering expanded capability for complex or critical bridge designs.

1.3. INTRODUCTION

Recordings from past earthquakes have shown that ground shaking near a rupturing fault can be significantly more intense—and damaging—than shaking observed at greater distances. In response, Caltrans has, since 1992, increased the design response spectrum for sites located within 15 km of an active fault to account for the severity of near-fault ground motion. These enhancements, implemented using period-dependent adjustment factors, have undergone only minor revisions since their original adoption.

This project seeks to evaluate the current Caltrans Near-Fault Adjustment Factors and offers recommendations for improving the existing model based on the latest scientific understanding, including a statewide seismic hazard model that explicitly incorporates near-fault effects, as well as findings from a recent study examining the inelastic structural response to near-fault ground motions.

These Near-Fault Adjustment Factors are in part based on probabilistic seismic hazard spectra, which aggregate contributions from both near-fault and far-fault sources by incorporating their respective recurrence rates. As a result, the representation of directivity effects in probabilistic spectra is significantly more complex than in scenario-based spectra, where ground motions are associated with a single deterministic source. A simplified model of the directivity-based PSHA was developed. The resulting near-fault adjustment factors were subsequently modified to incorporate general characteristics of inelastic structural response.

The figures included in the body of this report were selected represent a particular case: a Return Period of 2475yr. This return period was selected as it typically considered the default case. The same calculations were carried out for other return periods and the figures will be presented in a digital appendix.

1.3.1. Task 1: Use of the UCLA NHR3 Interactive 2023 Directivity Hazard Map to Determine Directivity Effects

The objective of this task was to evaluate whether the directivity effects presented in the UCLA NHR3 interactive 2023-directivity hazard map could be adequately represented using a simplified parameterization based solely on distance from the fault. Instead of using a set of representative sites, a simplified directivity-amplification versus distance model was developed using the entire statewide dataset – binned by magnitude, return period, source type (excluded subduction), and oscillator period.

The results demonstrated how closely the simplified model aligns with the full directivity representation, highlighting both strengths and limitations of the reduced parameterization.

This work is documented in this report and includes:

- The statewide geographic distribution of directivity effects,
- The methodology used for simplification,
- The simplified model,
- Quantitative comparisons between the simplified and full directivity models.

This evaluation provides a foundation for assessing whether a simpler distance-based approach may be suitable for certain design applications, or where incorporating full directivity models may offer significant benefit.

1.3.2. Task 2: Consideration of Inelastic Response

The objective of this task was to develop near-fault adjustment factors applicable to analysis that explicitly account for the effects of inelastic structural response under pulse-type ground motions. This was accomplished using the findings from the UCLA NHR3 report *GIRS-2023-01*, sponsored by Caltrans, which quantifies the impact of inelastic behavior on effective period elongation in response to near-fault pulses.

Using the methodology and supporting data from the above study, inelastic adjustment factors were derived by evaluating the elongation of structural period due to nonlinear behavior. These adjustments were calculated across a representative range of pulse periods for two levels of ductility demand, allowing for coverage of typical structural response characteristics. A probabilistic model for pulse period was reviewed, and an appropriate model was selected to ensure realistic representation of near-fault motion variability.

This report documents:

- The development of the inelastic adjustment factors,
- A comparison between traditional elastic-based directivity effects and the refined inelastic response-based modifications,
- And the final recommended adjustment factors for use in modal analysis.

These results provide a significant advancement in incorporating inelastic behavior into seismic design near active faults, improving the reliability of structural performance predictions.

1.4. PAST PROJECTS

1.4.1. Statewide California PSHA-with-Directivity Study

As part of a comprehensive risk and resilience study of California's infrastructure system, a statewide seismic hazard analysis was conducted using probabilistic seismic hazard analysis (PSHA) methodology. This analysis reflects the latest advancements in seismic hazard science. Specifically, the most up-to-date ground motion models (GMMs) were employed to compute pseudo-spectral acceleration (PSA) intensity measures, both with and without incorporating near-fault directivity effects. The Uniform California Earthquake Rupture Forecast, Version 3 (UCERF-3), shown in **Figure 1-1**, was used as the seismic source model, as it represents the current best understanding of earthquake behavior in California. The analysis covered 19,316 sites across the state, based on a high-resolution grid with 0.05° × 0.05° spacing in both longitude and latitude.

At each site, PSHA was performed for a range of Vs_{30} values (VS30), from 180 m/s to 1100 m/s. Vs_{30} is the time-averaged shear-wave velocity in the upper 30 meters of soil. It is used in determining the site class of a site. The analyses included site-specific VS30 estimates derived from three-dimensional geophysical velocity models across California, as illustrated in **Figure 1-2**. Where available and deemed reliable, the analysis also incorporated site-specific basin depth parameters—Z1.0 and Z2.5. PSA values were computed for 23 periods, including PGA, PGV, and spectral periods ranging from 0.01 to 10 seconds, and across 8 return periods spanning from 50 to 10,000 years. Additionally, the study evaluated the effects of near-fault directivity by calculating directivity amplification factors—defined as the ratio of PSA values with directivity to those without. These results, along with deaggregation data at all sites, were used to assess and recommend improvements to the current directivity amplification methodology employed by Caltrans. The data products from the statewide study are shown in **Figure 1-3**.

Because of the significant computation effort involved in including directivity in PSHA, it was included only for the case Vs30=760m/s. However, the study demonstrated that the directivity-amplification factors computed for this Vs30 applied to all other site classes in regions where subduction sources did not control the hazard, as is the case for the regions considered in this study.

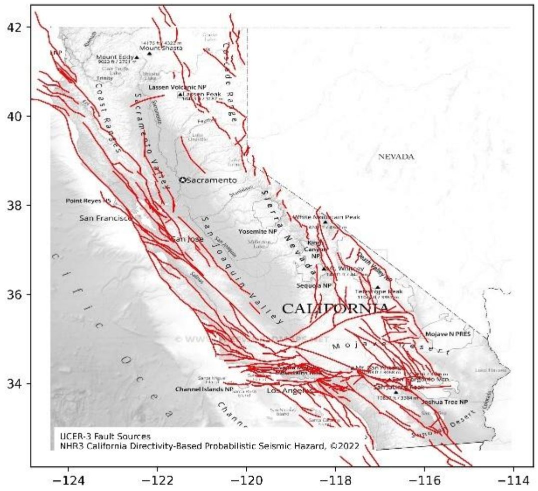

Figure 1-1 UCERF-3-Based Fault Sources

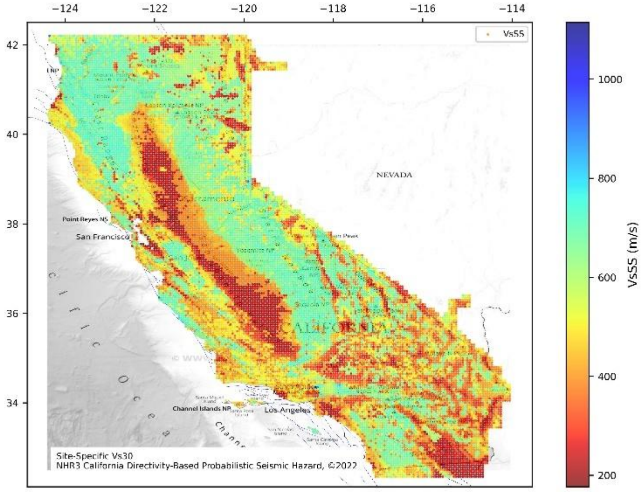

Figure 1-2 Estimated Site-Specific Vs30

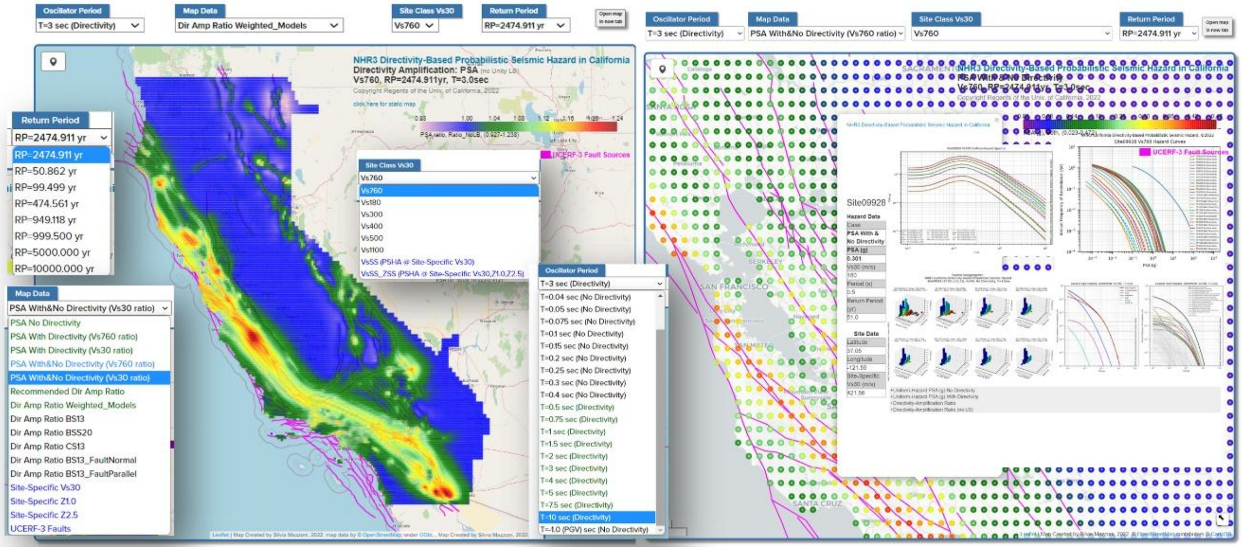

Figure 1-3 Data availability – metrics and geographic distribution of data.

1.4.1.1. Directivity Models used in PSHA Study

Three directivity models were incorporated into GMMs and carried out PSHA including the directivity effects. Three sets of directivity models were incorporated:

- **CS13 – Chiou and Spudich (2013):** This model is based on the Direct Point Parameter (DPP) and captures directivity effects using a physically grounded approach tied to fault geometry and rupture characteristics.
- **BS13 – Bayless and Somerville (2013):** An update to the earlier Somerville et al. (1997) model, BS13 offers a simplified formulation with a minimal set of predictive parameters, making it computationally efficient.
- **BSS20 – Bayless et al. (2020):** A further refinement of the BS13 model, BSS20 incorporates narrowband directivity characteristics and is designed to better handle

complex and multi-segment fault ruptures. While it maintains much of the computational simplicity of BS13, BSS20 integrates both empirical ground-motion data and finite-fault simulations in its development. *Note:* This update applies only to the average horizontal component of ground motion and does not include revised predictions for fault-normal and fault-parallel components.

It is important to note that directivity effects were not applied to gridded seismicity or to subduction sources included in the seismic source characterization model for Northern California.

1.4.1.2. Model Weighting in PSHA Hazard Calculations

Based on an evaluation presented in the full study report, the three models were assigned the following weights for use in probabilistic seismic hazard analysis (PSHA) to compute the Weighted-Model with-directivity PSA:

- **CS13**: 0.50
- **BS13**: 0.25
- **BSS20**: 0.25

These weights reflect the relative confidence and applicability of each model in capturing directivity effects from crustal fault sources.

1.4.2. Inelastic-Response Spectra Study

This study developed ground motion models (GMMs) specifically for inelastic response spectra, using data from the NGA-West2 ground motion database. While traditional GMMs focus on elastic response, this project addresses the gap in predicting how real structures, which behave inelastically during strong shaking, respond to earthquakes. Inelastic response spectra were calculated for a range of ductility factors (μ = 1.5, 2, 3,4, 5) -- representing increasing levels of nonlinearity in structures. The authors developed new predictive equations for median inelastic spectral response and standard deviation, accounting for variables like magnitude, distance, site effects (e.g., Vs30), fault mechanism, and spectral period. These models are an extension of elastic GMMs but customized for inelastic demands. In addition to traditional GMMs, this study proposed models for adjustment factors for elastic PSA to get inelastic response. The study also qualitatively studied the effect of directivity pulses on inelastic and elastic response spectra.

Figure 1-4 illustrates the average influence of inelastic behavior on ground motions identified as pulse-like. Here, Cy refers to the seismic coefficient in constant-ductility response spectra, which represents structural demand accounting for inelastic behavior. Panel (a) shows the ratio of observed to median predicted Cy values, and panel (b) presents the average difference between the total residuals of inelastic Cy and those of the elastic response (i.e., PSA). This figure qualitatively shows that increased structural ductility (inelasticity) reduces the peak directivity effects near the pulse period (T/Tp ≈ 1) while broadening the response enhancement to shorter periods (lower T/Tp values). At longer periods (higher T/Tp values), the effect of varying ductility diminishes as all response curves converge.

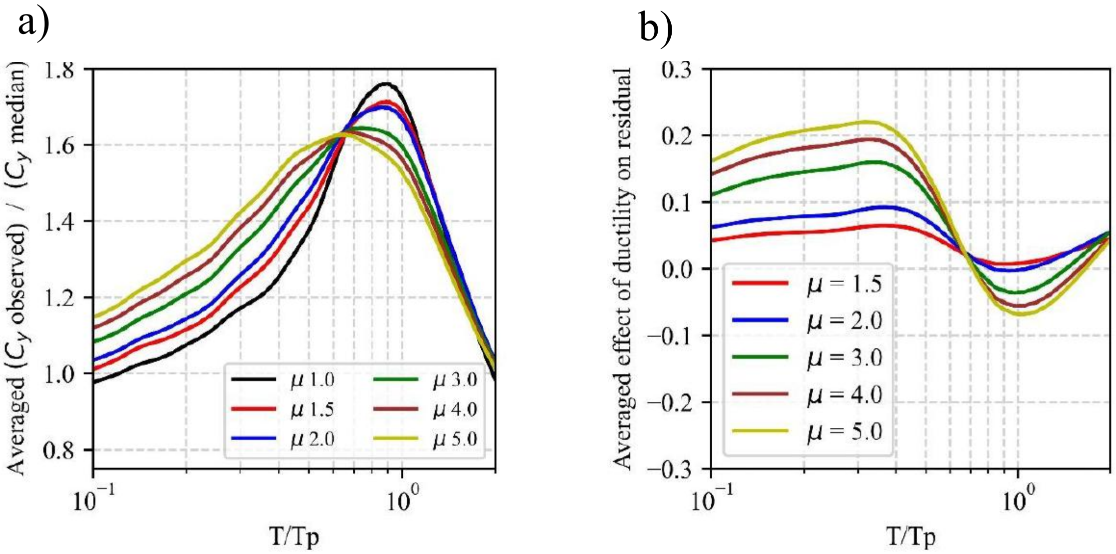

Figure 1-4 *Findings from Inelastic Response Spectra Study. Bilinear Takeda Hysteretic Model, Vs30=760 m/s, 5% damping.*

1.5. CALTRANS SEISMIC DESIGN CRITERIA

Appendix B of the Caltrans Seismic Design Criteria (2019) defines a Near-Fault Spectrum Adjustment Factor to account for elevated ground shaking at sites located near a rupturing fault, particularly at spectral periods longer than 0.5 seconds. As illustrated in **Figure 1-5**, this adjustment factor is applied to sites within 15 km of a fault rupture and gradually tapers to zero at a distance of 25 km. Similarly, the factor is applied to spectral periods starting at 0.5 seconds, tapering to a full amplification for period of 1.0 second and above. Factors for a range of distance and periods are shown in **Table 1.1**.

For application to probabilistic response spectra, the guidelines specify that the "probabilistic distance" should be determined as the smaller of the following:

- The **mean distance**, and
- The **mode distance** corresponding to the distance–magnitude pair contributing the most to the hazard.

However, this distance must **not be less than** the shortest distance from the site to the rupture plane of the nearest fault listed in the Caltrans Fault Database.

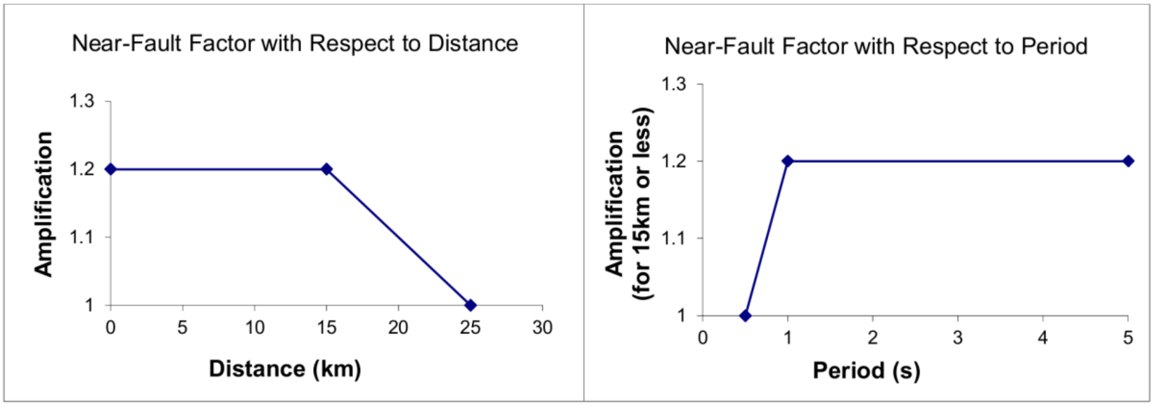

Figure 1-5 *SDC 2.0 -Figure B.1 Near-Fault adjustment factor as a function of distance and spectral period.*

Based on the figure above, the Caltrans Directivity Model is governed by three key parameters:

- **Threshold Distance** – the distance beyond which directivity amplification is considered negligible.
- **Minimum Elastic Period** – the spectral period at which directivity effects begin to influence ground motion.
- **Maximum Amplification Factor** – the peak amplification applied in near-fault zones, specifically for sites located within the threshold distance and at periods exceeding the minimum elastic period.

The primary objective of this study is to evaluate the current values assigned to these parameters and provide recommendations for adjustments. These recommendations are based on analyses of both **elastic** and **inelastic** response spectra to ensure the model more accurately reflects observed ground motion behavior in near-fault regions.

***Table 1.1** Caltrans Spectrum Adjustment Factors (SDC 2.0)*

Amp Factor		**Distance (km)**												
		0.1	1	2.5	5	7.5	10	12.5	15	20	25	30	35	40
Period (sec)	0.01	1	1	1	1	1	1	1	1	1	1	1	1	1
	0.1	1	1	1	1	1	1	1	1	1	1	1	1	1
	0.2	1	1	1	1	1	1	1	1	1	1	1	1	1
	0.3	1	1	1	1	1	1	1	1	1	1	1	1	1
	0.4	1	1	1	1	1	1	1	1	1	1	1	1	1
	0.5	1	1	1	1	1	1	1	1	1	1	1	1	1
	0.75	1.1	1.1	1.1	1.1	1.1	1.1	1.1	1.1	1.05	1	1	1	1
	1	1.2	1.2	1.2	1.2	1.2	1.2	1.2	1.2	1.1	1	1	1	1
	1.25	1.2	1.2	1.2	1.2	1.2	1.2	1.2	1.2	1.1	1	1	1	1
	1.5	1.2	1.2	1.2	1.2	1.2	1.2	1.2	1.2	1.1	1	1	1	1
	1.75	1.2	1.2	1.2	1.2	1.2	1.2	1.2	1.2	1.1	1	1	1	1
	2	1.2	1.2	1.2	1.2	1.2	1.2	1.2	1.2	1.1	1	1	1	1
	2.5	1.2	1.2	1.2	1.2	1.2	1.2	1.2	1.2	1.1	1	1	1	1
	3	1.2	1.2	1.2	1.2	1.2	1.2	1.2	1.2	1.1	1	1	1	1
	5	1.2	1.2	1.2	1.2	1.2	1.2	1.2	1.2	1.1	1	1	1	1

1.5.1. Caltrans Bridge Locations

The Caltrans researchers supporting the project provided us with an unofficial list of Caltrans Bridges and their location coordinates. This is not intended to be an accurate or extensive list, it was provided to us to compare the geographic distribution of the PSHA metrics with the geographic distribution of Caltrans Bridges. These data, along with the UCERF-3 fault sources, are shown in **Figure 1-6**.

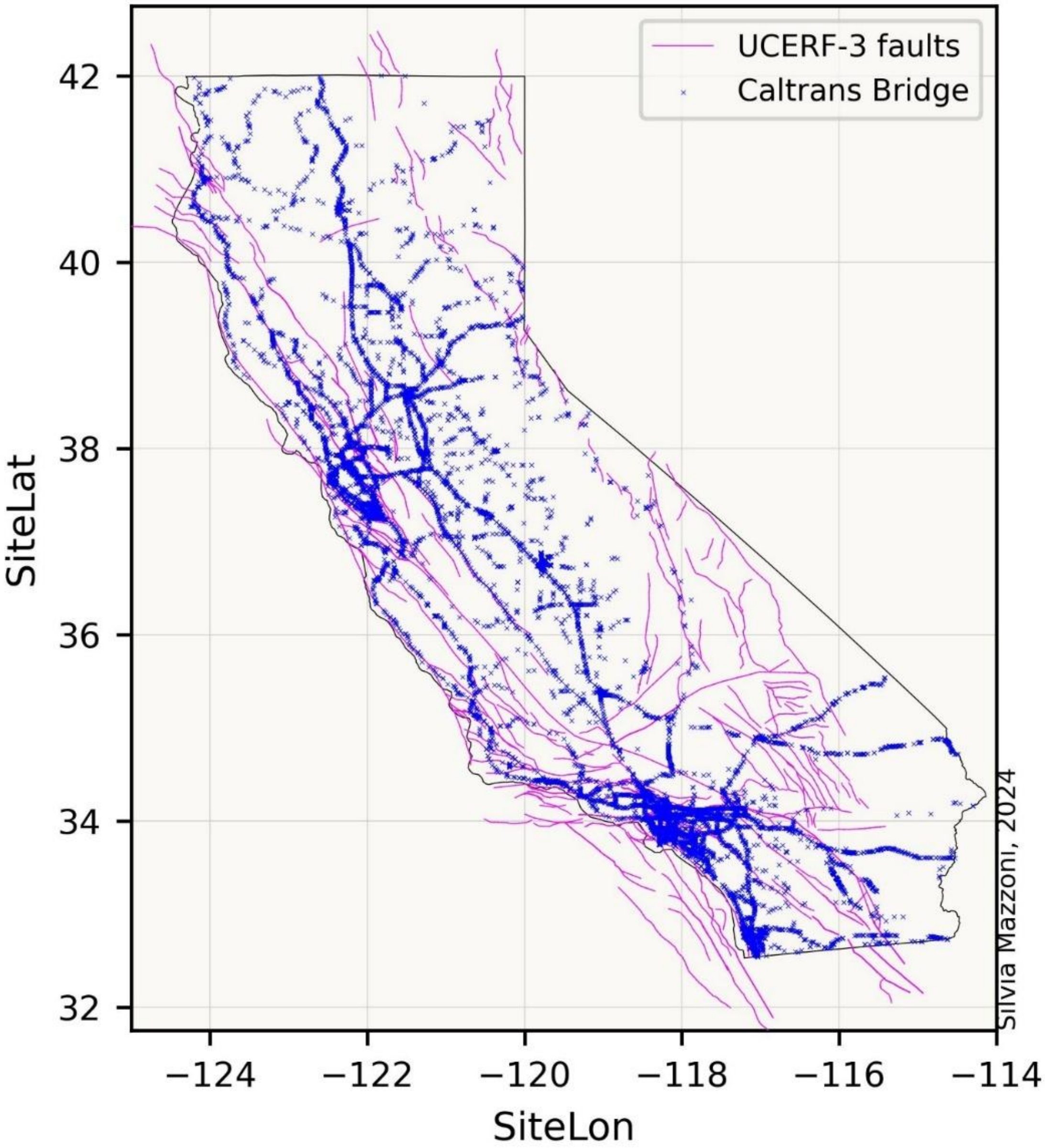

Figure 1-6 *Geographic Distribution of Caltrans Bridge and UCERF-3 Fault Sources*

1.6. CALIFORNIA STATEWIDE DIRECTIVITY PSHA DATA

The geographic distribution of PSA values for an oscillator period of T = 3.0 seconds, Vs30 = 760 m/s, and a return period of 2,475 years, both with and without directivity effects, using a consistent color scale is shown in Figure 1-7. Fault sources from the UCERF-3 model are overlaid for reference. Comparable maps have been generated for all other combinations of period, site condition, and return period considered in the study.

These data were used to compute the directivity amplification ratio (i.e., PSA-with-directivity / PSA-no-directivity) for the weighted directivity model, as shown in **Figure 1-8**. The figure illustrates the complex spatial patterns of both the underlying fault network and the resulting amplification effects due to directivity, emphasizing the significance of capturing these effects in regional seismic hazard assessments. As shown in **Figure 1-9**, the directivity amplification ratio is also period-dependent – generally, directivity amplification increases with period. These figures show the geographic distribution of this ratio for all the directivity periods, one graph per period, in the range of 0.5 to 10 seconds. **Figure 1-10** shows the same data, with the addition of the location of the Caltrans Bridges.

It is worth noting that the directivity amplification factor falls below 1.0 in areas away from fault sources. This effect is due to some of the directivity models as well as rounding errors. Even though we recommend setting a lower bound of 1.0 to the directivity amplification, this lower bound was not applied to the dataset used in this study.

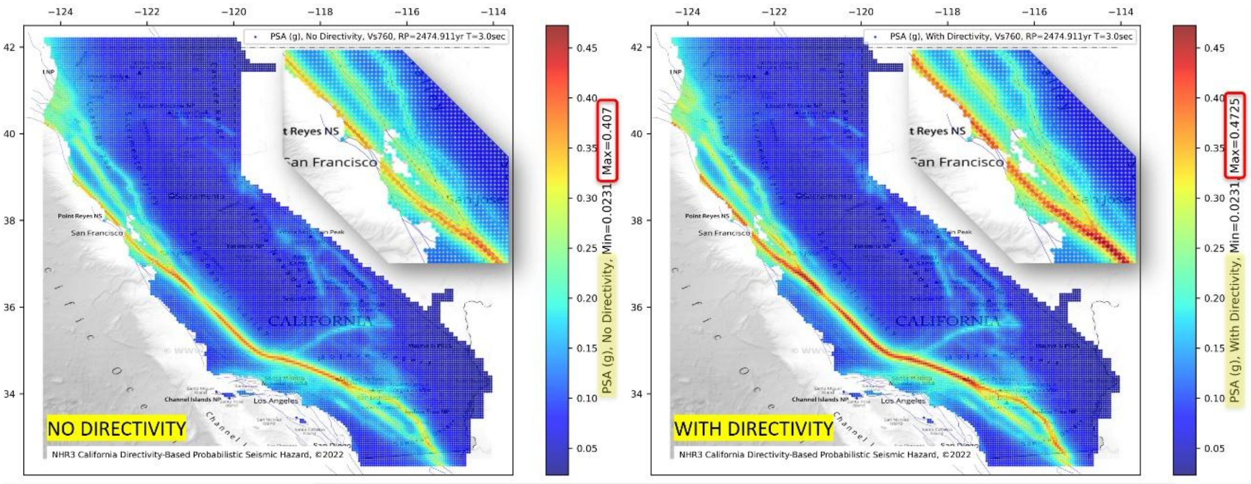

Figure 1-7 *Mapped PSA with and Without Directivity Amplification. T=3.0sec, Vs30=760m/s, Return Period=2475yr*

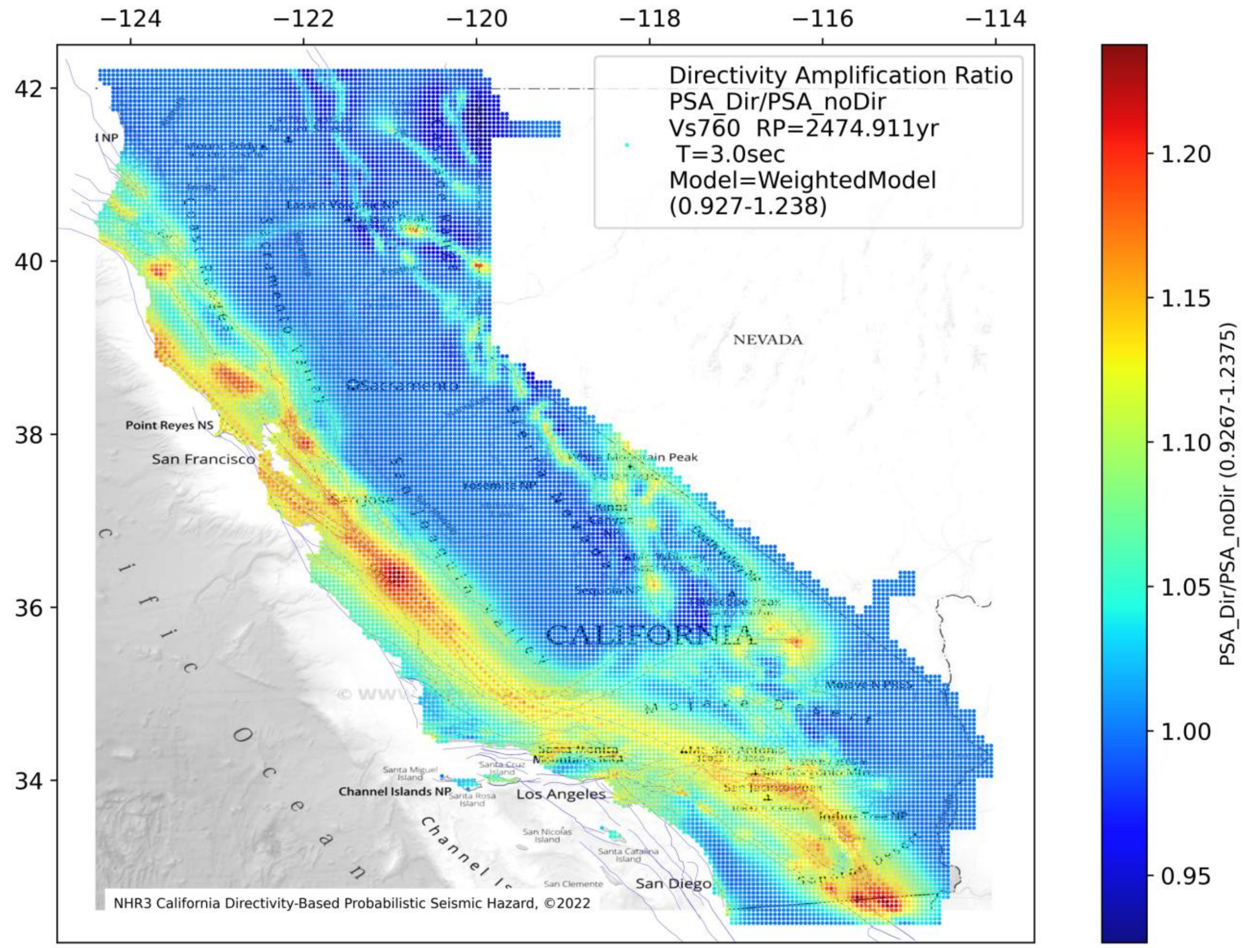

Figure 1-8 *Geographic Distribution of Weighted-Model Directivity Amplification Factor (Vs30=760m/s, RP=2475yr, T=3.0s)*

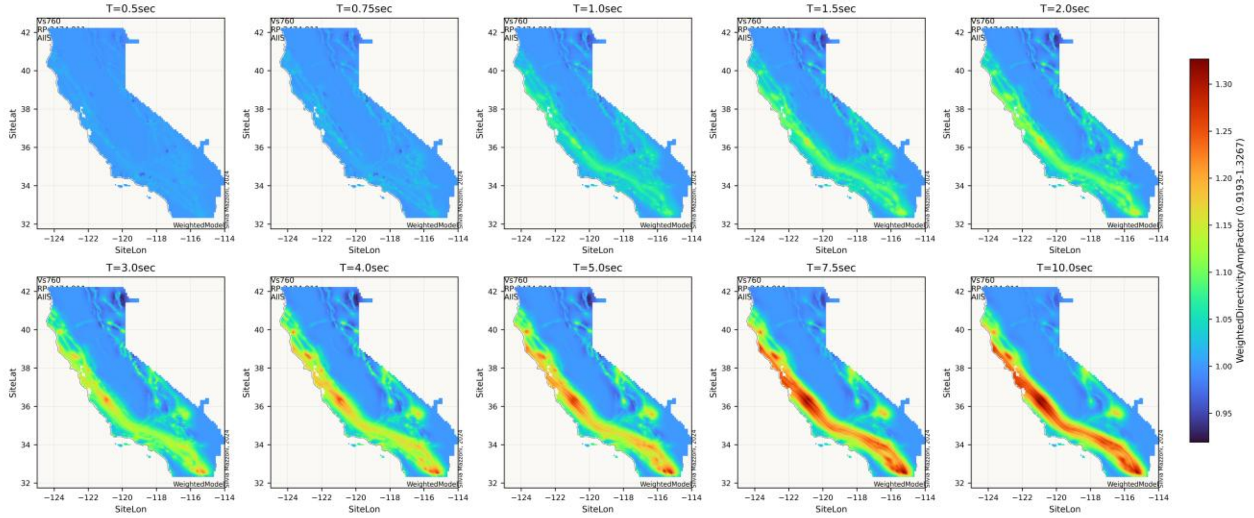

Figure 1-9 *Geographic distribution of Weighted-Model Directivity Amplification Factor (Vs30=760m/s, RP=2475yr) – for Directivity Periods 0.5s-10s*

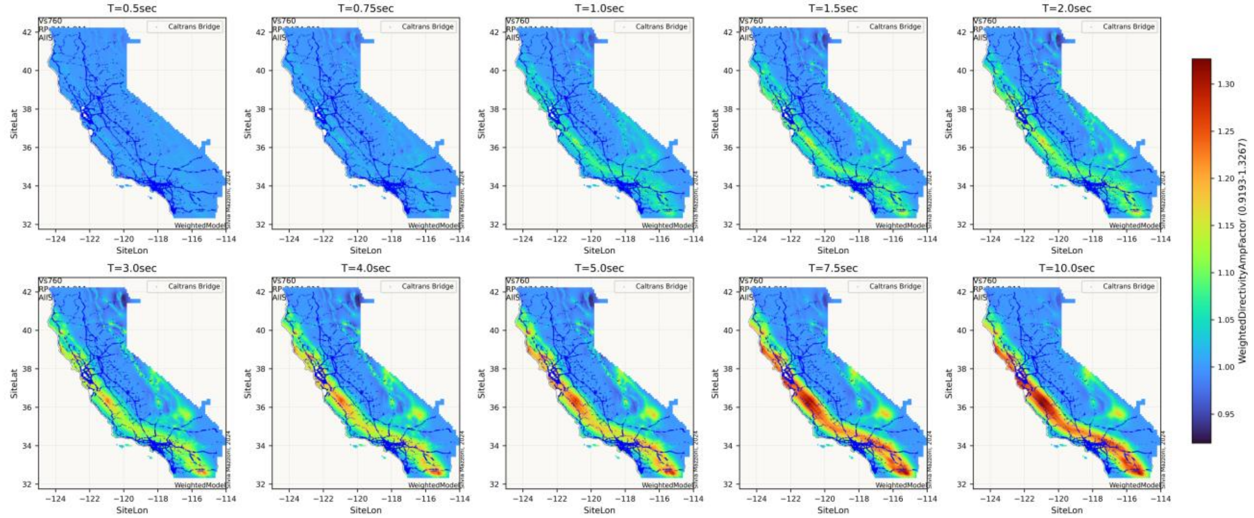

Figure 1-10 *Caltrans-Bridge Locations + Geographic Distribution of Weighted-Model Directivity Amplification Factor (Vs30=760m/s, RP=2475yr) – for Directivity Periods 0.5s-10s*

1.6.1. Directivity-Model Comparison

Directivity-Amplification factors were computed for the Weighted Model as well as the three individual directivity models. **Figure 1-11** shows the mapped values for the case of Vs30=760m/s, Return-Period=2475yr, and T=3.0sec. To enable a visual comparison, all 4 maps use the same color scale. The range of values for each case is shown in each legend.

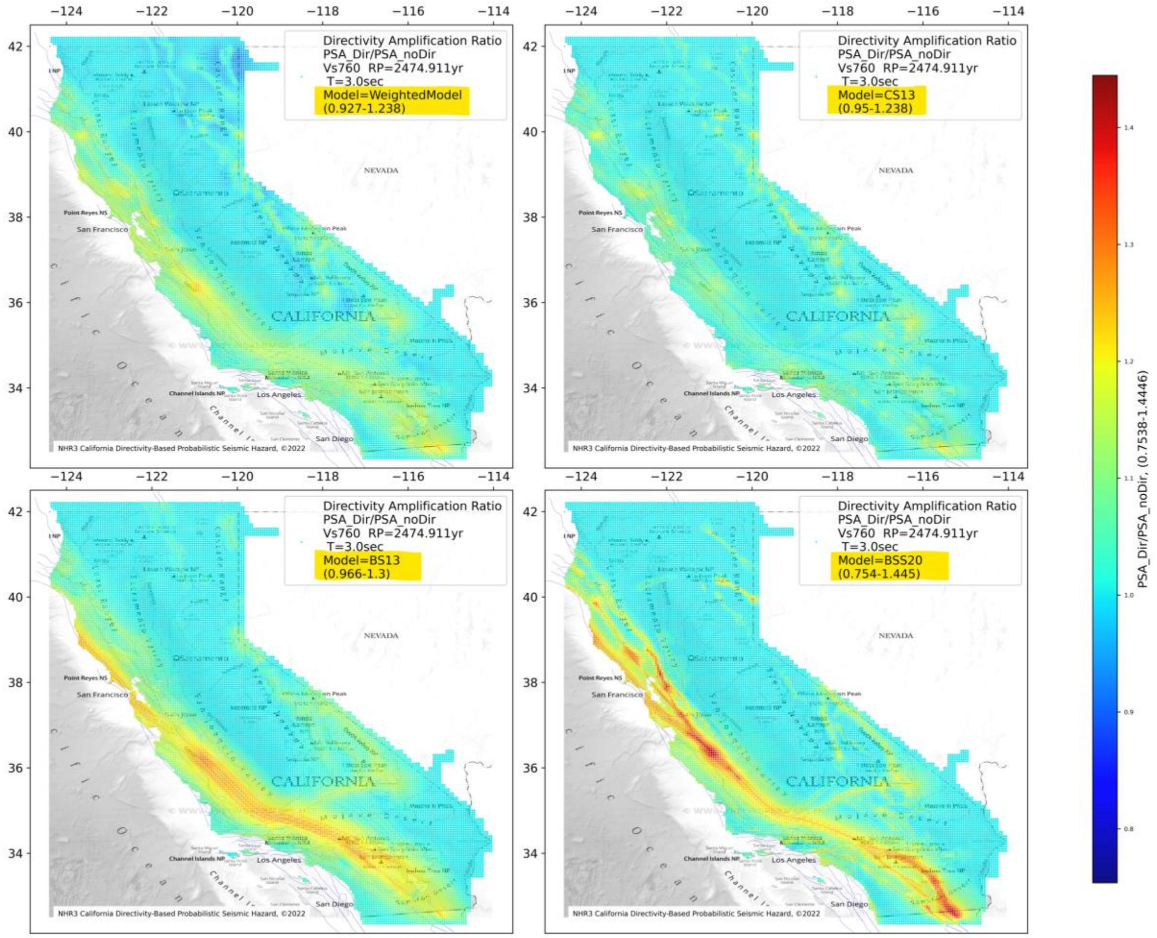

Figure 1-11 Geographic Distribution of Directivity Amplification Factor – Comparison of all Directivity Models. (Vs30=760m/s, Return Period=2475yr, T=3.0s)

1.6.2. Data Selection & Bins

The first step in selecting and binning the data involved removing sites not on land and limiting the cases to oscillator periods at and above 0.5 seconds, as directivity effects were only considered for this period range.

1.6.2.1. Selection by Source-Type Contribution

The next step involved excluding sites where subduction events contributed to more than 30% of the total hazard. These sites were excluded because directivity models were applied only to crustal-fault events and including them would introduce a bias into the directivity-amplification factor by reducing its effect.

Figure 1-12 and **Figure 1-13** show the Source-Type hazard curves for a site that was included in the dataset and one that was excluded, respectively, for Vs30=760 m/s, Return Period=2475yr and oscillator period=3.0s. The site in **Figure 1-12** was selected as an example because it lies very close to the San Andreas Fault, hence this fault controls the hazard at all return period. The site in **Figure 1-13**, on the other hand, was chosen as an example because it shows that the relative contribution of the different types of events is return-period dependent (Annual frequency of exceedance). These data were processed for all sites and transformed into maps and are shown in the next set of figures.

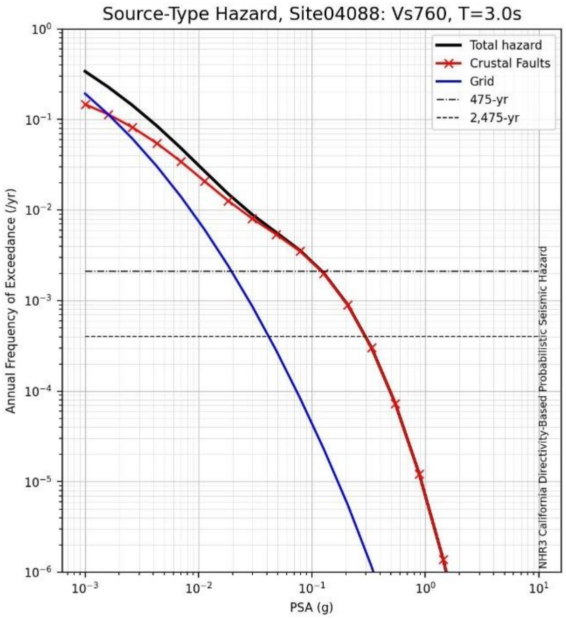

Figure 1-12 *Source-Type Hazard Curve, Vs30=760m/s, T=3.0 sec (Site 04088, near Los Angeles)*

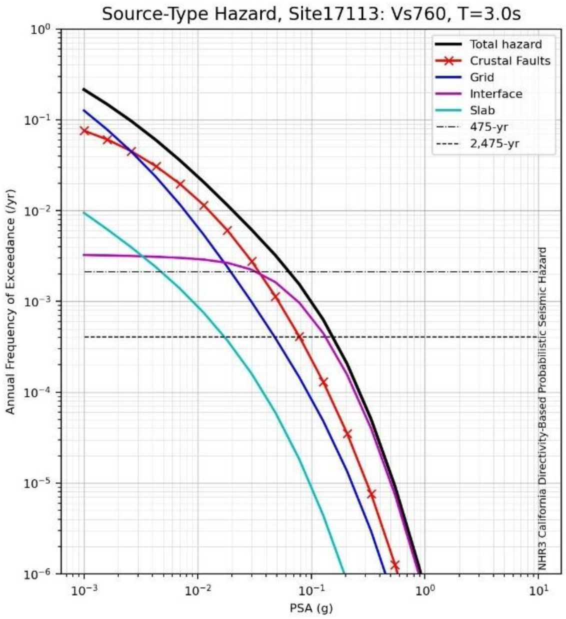

Figure 1-13 *Source-Type Hazard Curve, Vs30=760m/s, T=3.0 sec (Site 17113, North-West California)*

Figure 1-14 maps the source type that has the largest contribution to the hazard. These plots show the period dependence of the contributions provide an overall understanding of the regions being considered in this dataset.

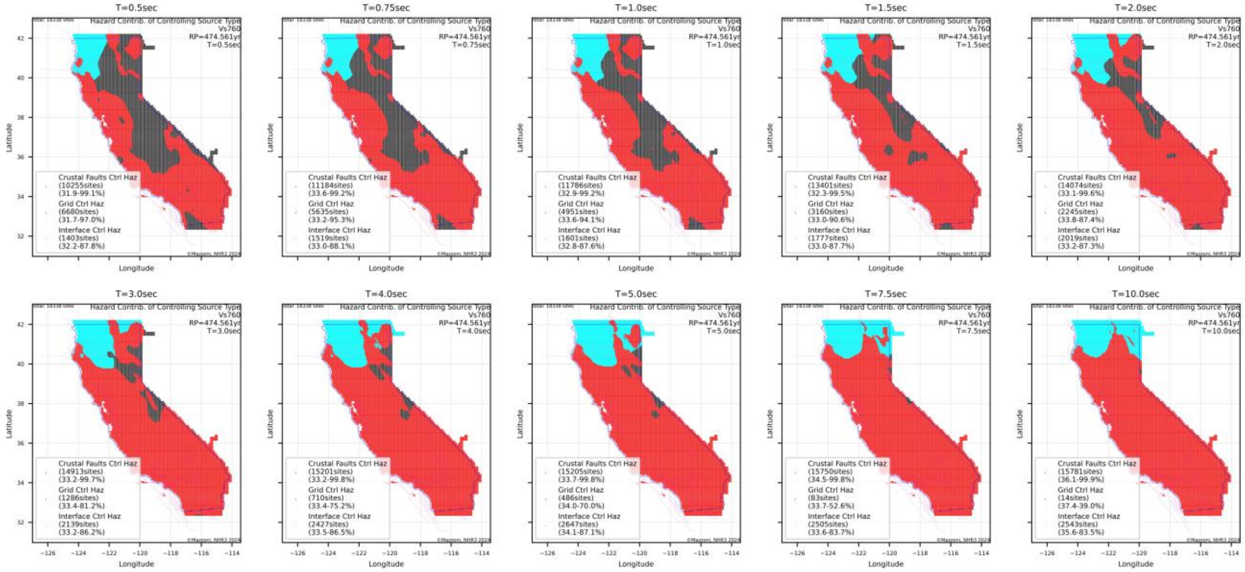

__Figure 1-14__ Hazard-Controlling Events (Vs30=760m/s RP=2475yr)

Figure 1-15 maps the percent contribution of subduction events – the combination of slab and interface events -- to the total hazard at each site. The sites where this value exceeded 30% were excluded from the dataset used in this study. These sites are located in the North-West corner of the state and the size of the area is period dependent, increasing with period.

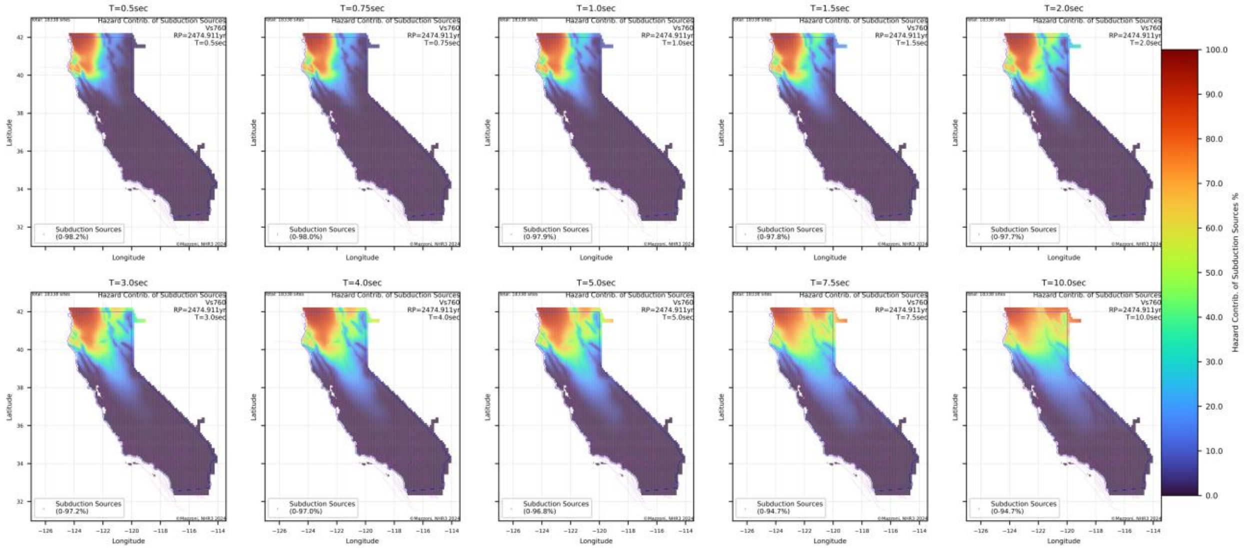

Figure 1-15 Percent Contribution to Hazard -- Subduction Events (Interface + Slab) (Vs30=760m/s RP=2475yr)

Figure 1-16 maps the contribution to the hazard of gridded events, to which no directivity was applied since they are area and not fault sources. These sites have the most significant contribution to the hazard in moderate periods and in areas away from the San Andreas Fault Zone. We did not exclude these sites because they lie close enough to fault sources that could have a higher contribution to hazard when directivity is considered.

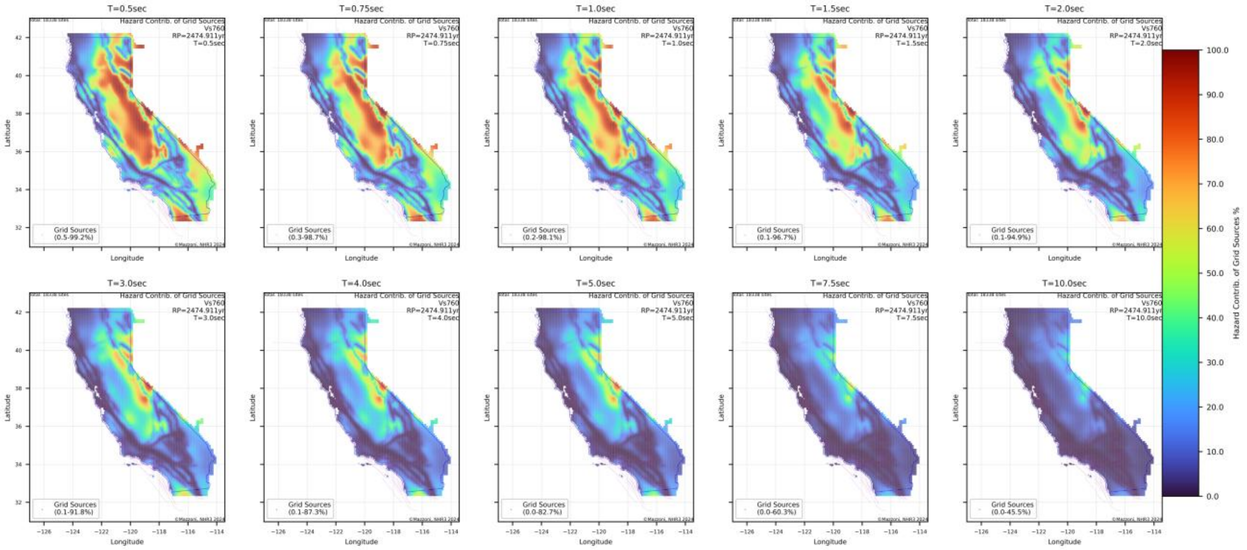

Figure 1-16 *Percent Contribution to Hazard -- Grid Events (Vs30=760m/s RP=2475yr)*

Figure 1-17 maps the contribution of crustal-fault events to the total hazard at each site. These are the only event type to which directivity-amplification factors were applied. In the moderate-period range crustal events have the largest contribution to the hazards in regions very close to faults, as expected. In the longer-period range the contribution increases in areas in Southern California farther from faults.

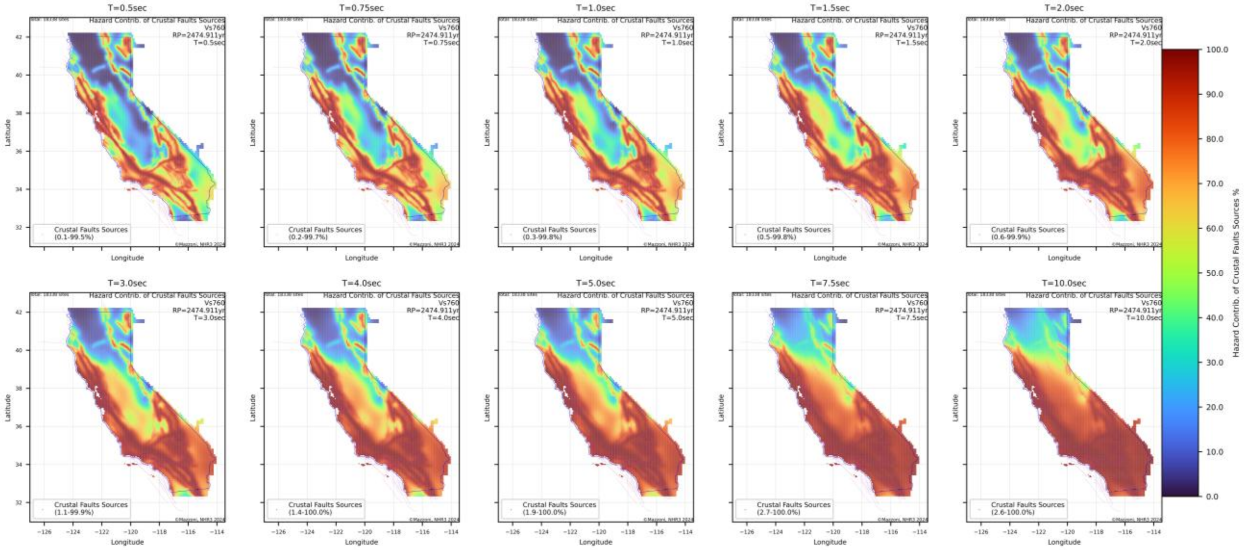

Figure 1-17 *Percent Contribution to Hazard – Crustal-Fault Events (Vs30=760m/s RP=2475yr)*

Figure 1-18 maps the directivity factors for the sites in the dataset – after we removed the sites where subduction events contributed to more than 30% of the total hazard. This figure corresponds to Vs30 = 760 m/s and a return period of 2,475 years. Each subplot represents a different oscillator period in the range of 0.5 to 10 seconds. **Figure 1-19** overlays the location of existing Caltrans bridges on the Directivity-Amplification Factor for the sites in the dataset.

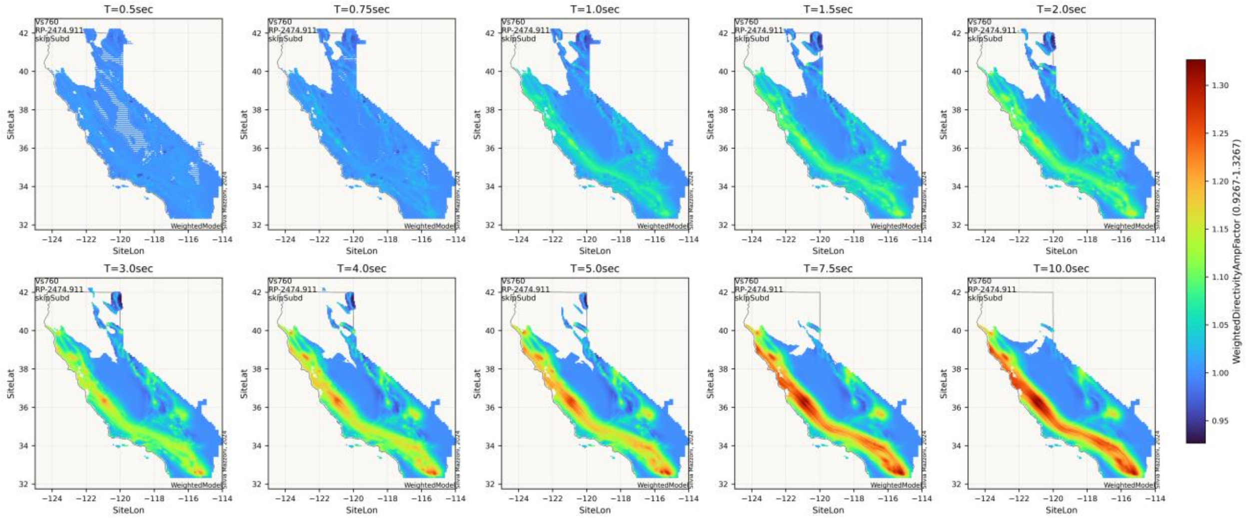

***Figure 1-18** Directivity-Amplification Factor For Sites in Dataset (Vs30=760m/s, Return Period=2475yr)*

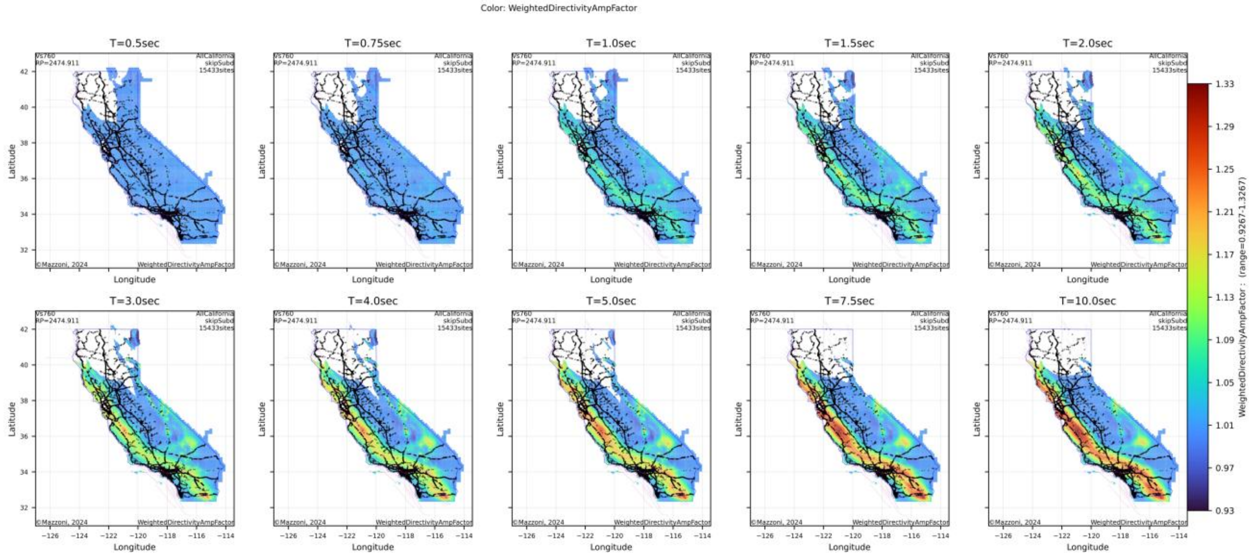

***Figure 1-19** Overlay of Existing-Caltrans-Bridge Locations and Directivity-Amplification Factor For Sites in Dataset (Vs30=760m/s, Return Period=2475yr)*

1.6.2.2. Bin by Deaggregation

The binned deaggregation data for the no-directivity case for each site was used in this study. It is important to emphasize that we need to use this deaggregation data, not the deaggregation from the directivity case, because it is what is available to a design engineer. An example of these data is shown in **Figure 1-20** for the case of Vs30=760m/s, oscillator period = 3.0 sec and one plot per return period.

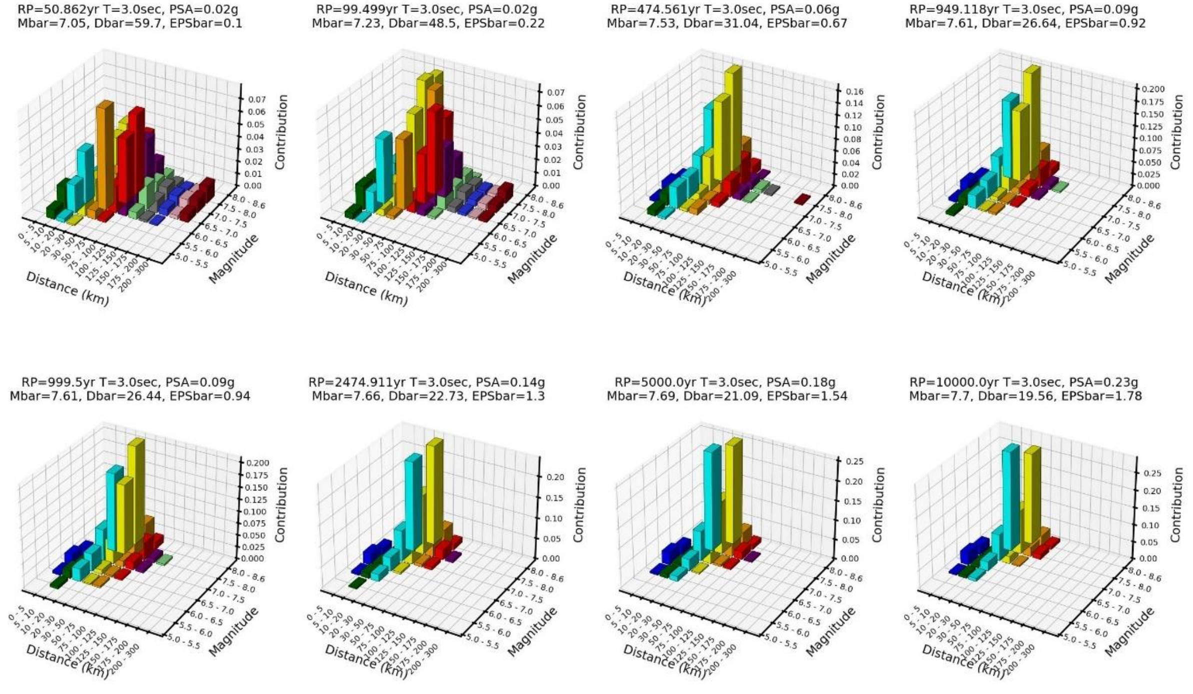
RP=50.862yr T=3.0sec, PSA=0.02g
Mbar=7.05, Dbar=59.7, EPSbar=0.1

RP=99.499yr T=3.0sec, PSA=0.02g
Mbar=7.23, Dbar=48.5, EPSbar=0.22

RP=474.561yr T=3.0sec, PSA=0.06g
Mbar=7.53, Dbar=31.04, EPSbar=0.67

RP=949.118yr T=3.0sec, PSA=0.09g
Mbar=7.61, Dbar=26.64, EPSbar=0.92

RP=999.5yr T=3.0sec, PSA=0.09g
Mbar=7.61, Dbar=26.44, EPSbar=0.94

RP=2474.911yr T=3.0sec, PSA=0.14g
Mbar=7.66, Dbar=22.73, EPSbar=1.3

RP=5000.0yr T=3.0sec, PSA=0.18g
Mbar=7.69, Dbar=21.09, EPSbar=1.54

RP=10000.0yr T=3.0sec, PSA=0.23g
Mbar=7.7, Dbar=19.56, EPSbar=1.78

Figure 1-20 *Binned Deaggregation Data. Vs30=760 m/s, T=3.0sec, Site01536 (Southern California)*

For each combination of Vs30, return period, and oscillator period, the following parameters were extracted:

- **Modal Magnitude and Distance** – Corresponding to the magnitude-distance bin that contributes the most to the hazard. While sensitive to bin size, these values represent a physically-meaningful scenario. As is shown in the plots of **Figure 1-20**, the distance bins had varying distance intervals -- 5, 10, 20, and 25km -- and the magnitude bins had magnitude intervals of 0.5 Magnitude units. The center values of each bin were used.
- **Mean Magnitude and Distance** – Computed as weighted averages based on each case's contribution to the hazard. Although convenient, these values do not represent a specific earthquake scenario. However they are easy to obtain because they are output by the hazard program itself as Mbar and Dbar.
- **Directivity Amplification Factor** – Defined as the ratio of PSA with directivity to PSA without directivity. The analysis used the weighted-average value across the three directivity models, though individual model results were also recorded.

The data were then binned by both modal and mean magnitude, allowing for a more structured assessment of directivity effects.

1.6.3. Deaggregation Bins

1.6.3.1. Mode

The modal magnitude and distance—defined as the center values of the magnitude-distance (M-R) bin contributing the most to the seismic hazard—were used in this study. The geographic distributions of these modal values are presented in **Figure 1-21** and **Figure 1-22**, corresponding to a Vs_{30} of 760 m/s and a return period of 2,475 years. The geographic distribution of the contribution of the Mode to the total hazard is shown in **Figure 1-23**. **Figure 1-24** and **Figure 1-25** overlay the Caltrans-Bridge locations with these Modal values.

These figures provide valuable insight into the spatial variability of the controlling earthquake scenarios and serve as a practical tool for estimating representative magnitude and distance values. Notably, the results illustrate a strong dependence of modal values on spectral period, highlighting the importance of period-specific analyses in seismic hazard assessment, especially when directivity is considered.

These maps can directly inform site-specific design decisions and provide a rational basis for selecting input parameters in ground motion modeling and scenario-based structural analyses.

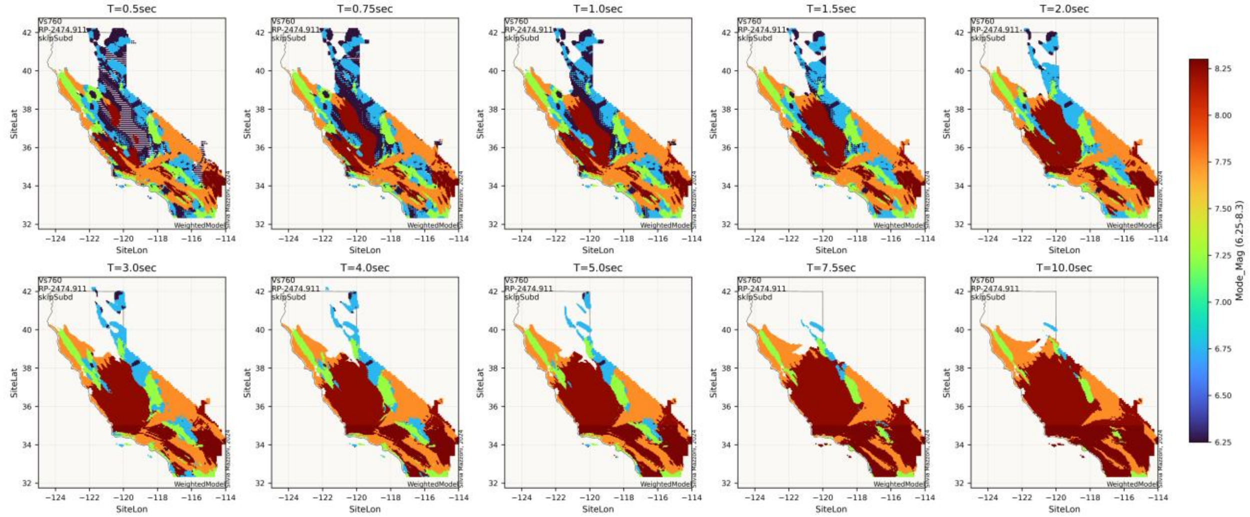

Figure 1-21 *Geographic Distribution of Modal Magnitude (Vs30=760m/s, RP=2475yr)*

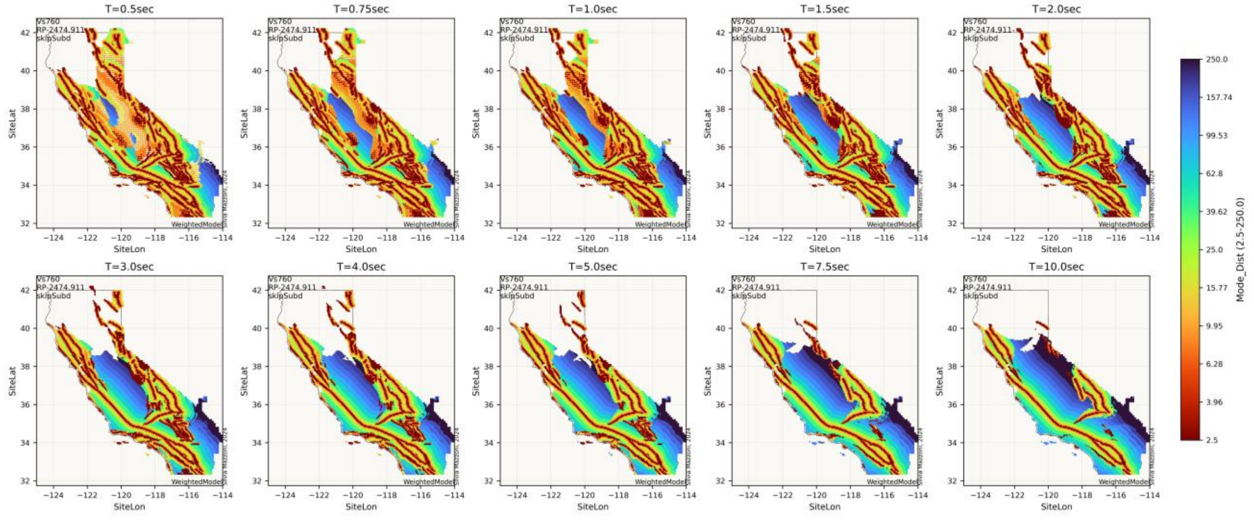

Figure 1-22 *Geographic Distribution of Modal Distance (km) (Vs30=760m/s, RP=2475yr)*

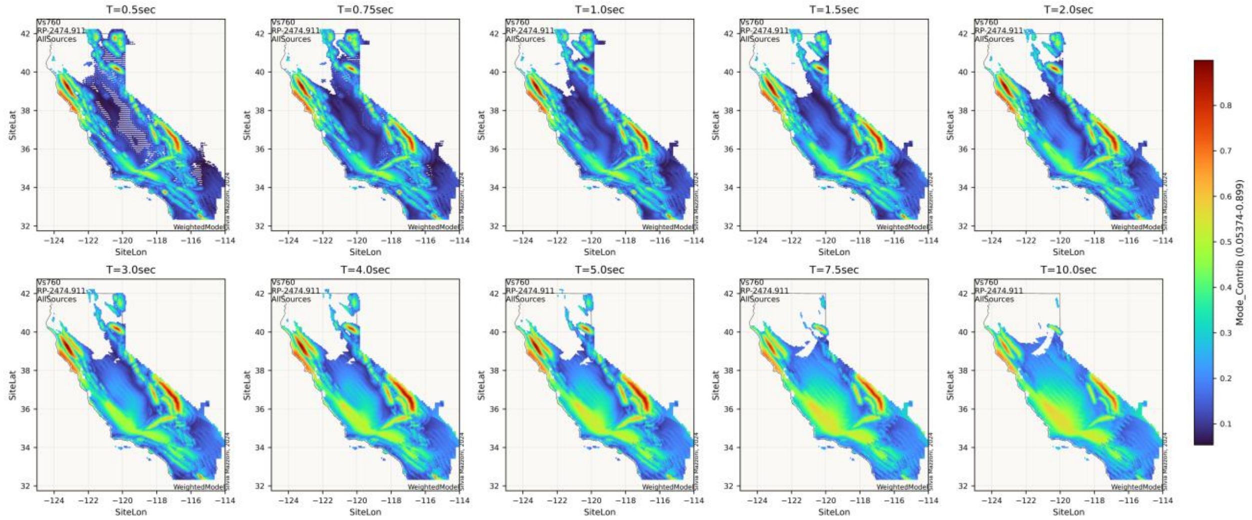

Figure 1-23 *Geographic Distribution of the Contribution of the Mode to the Total Hazard (Vs30=760m/s, RP=2475yr)*

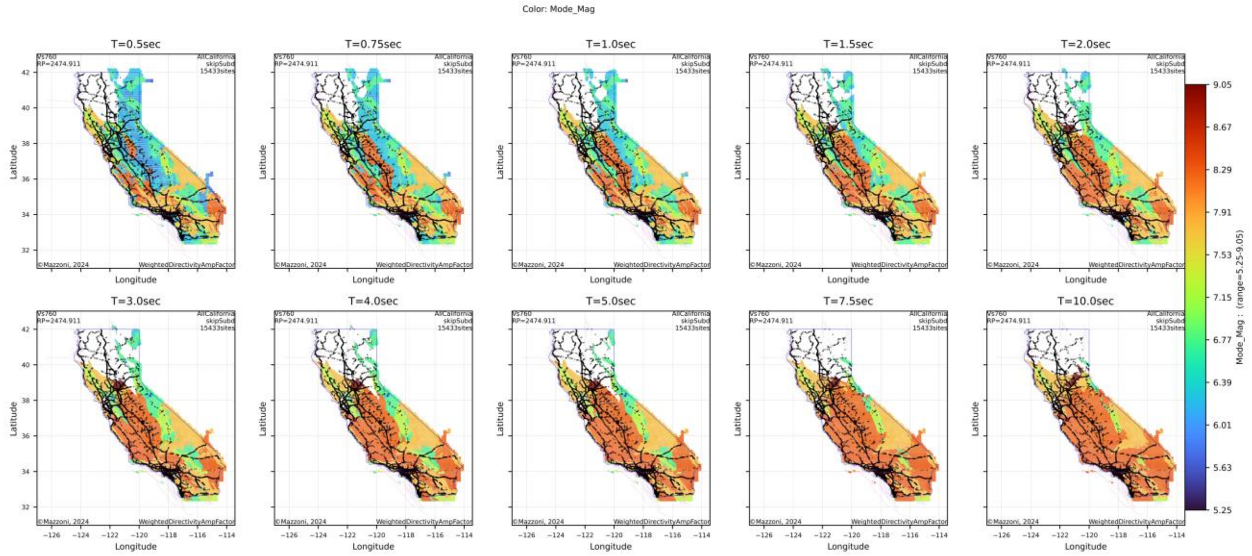

Figure 1-24 *Overlay of Existing-Caltrans-Bridge Locations and Geographic Distribution of Modal Magnitude (Vs30=760m/s, RP=2475yr)*

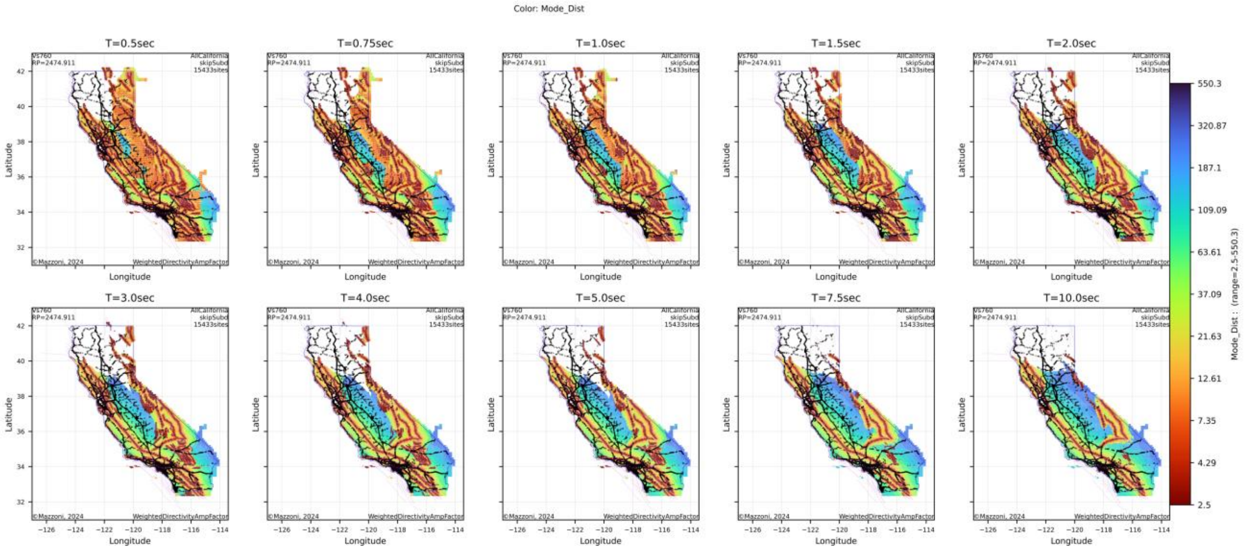

Figure 1-25 *Overlay of Existing-Caltrans-Bridge Locations and Geographic Distribution of Modal Distance (Vs30=760m/s, RP=2475yr)*

1.6.3.2. Mean

The mean magnitude, distance, and epsilon — generated by the hazard program — were computed and reported here, but were not used in this study. The geographic distributions of these values are presented in **Figure 1-26**, **Figure 1-27**, and **Figure 1-28**, respectively. These data correspond to a Vs_{30} of 760 m/s and a return period of 2,475 years. **Figure 1-29** and **Figure 1-30** overlay the Caltrans-Bridge locations with mean magnitude and distance values, respectively.

The data shown in these figures are similar to those for the modal values, however, because they are mean values that consider the entire hazard, they do not have the same extreme values as the mode. A detailed comparison of these two sets of data, which is beyond the scope of this study, can lead to valuable insight into hazard in California.

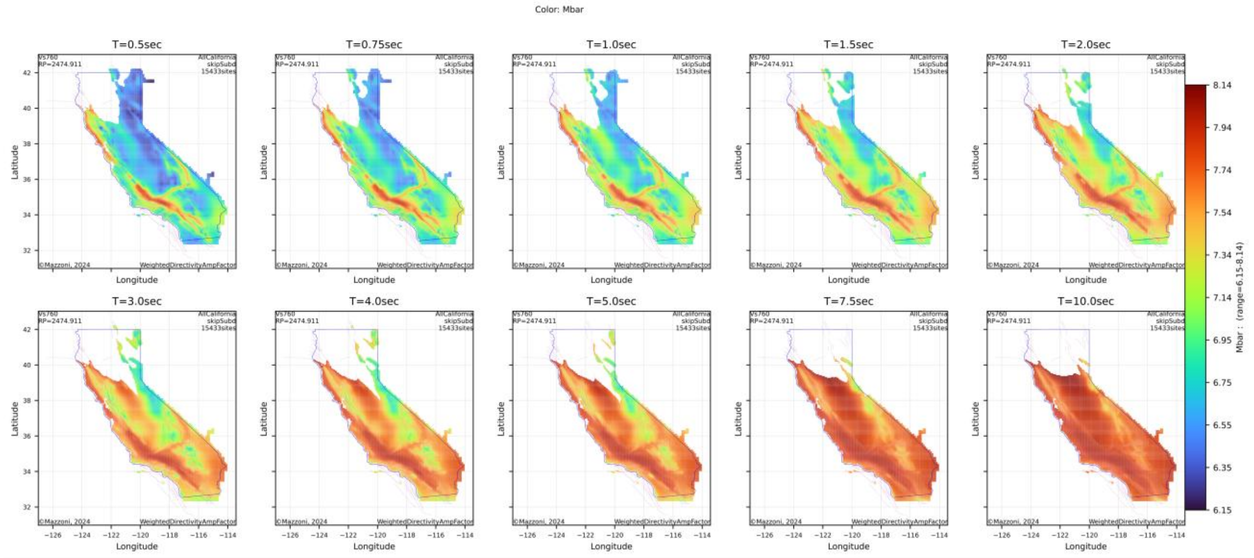

Figure 1-26 Geographic Distribution of Mean Magnitude (Mbar) (Vs30=760m/s, RP=2475yr)

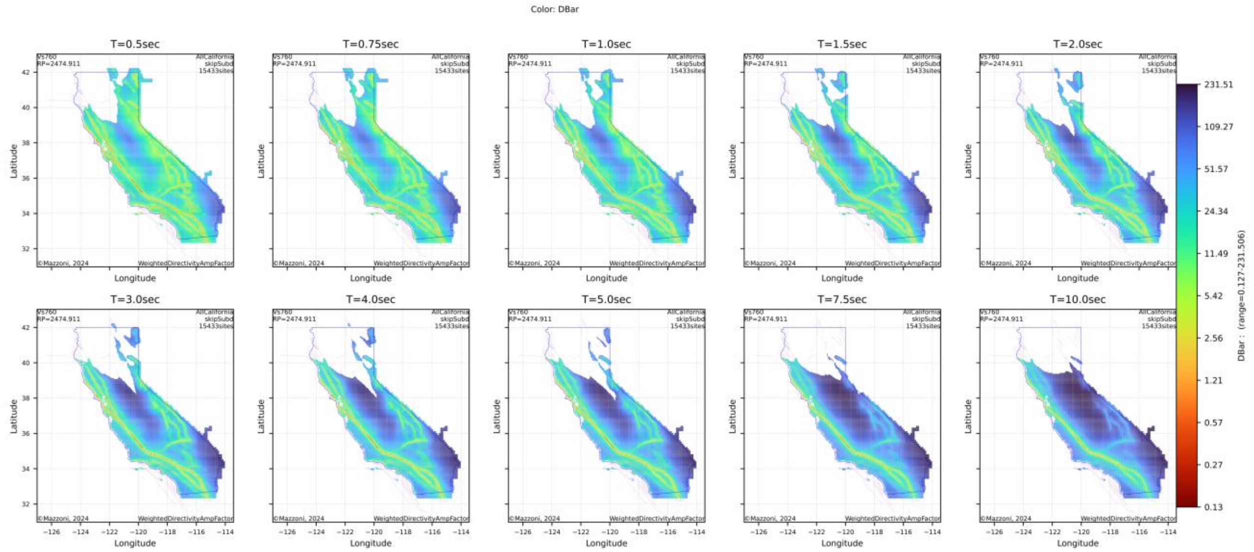

***Figure 1-27** Geographic Distribution of Mean Distance (Dbar) (km) (Vs30=760m/s, RP=2475yr)*

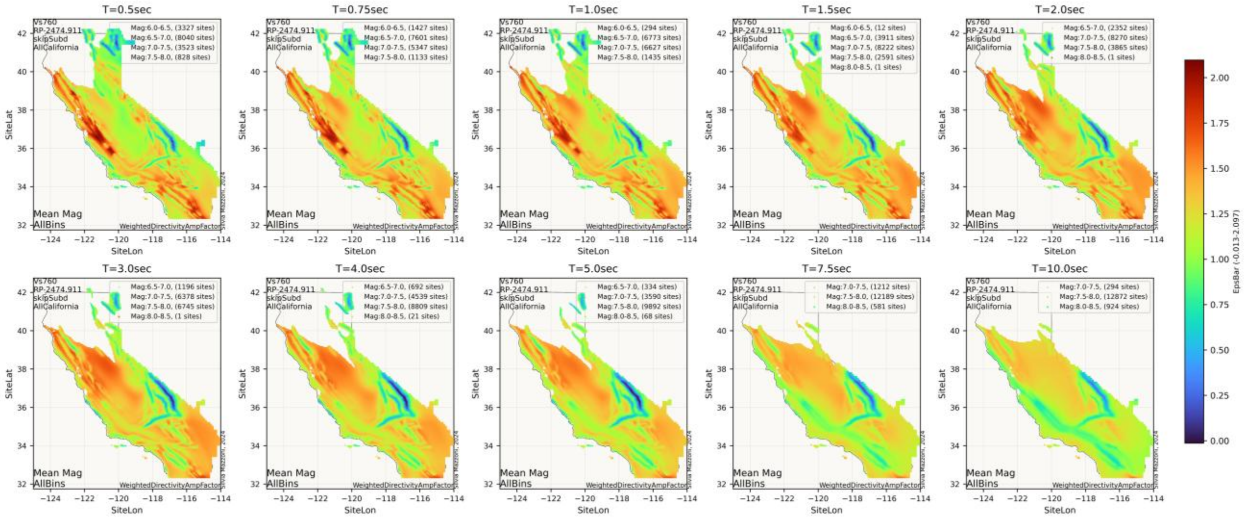

Figure 1-28 *Geographic Distribution of Mean Epsilon (Epsbar) (Vs30=760m/s, RP=2475yr)*

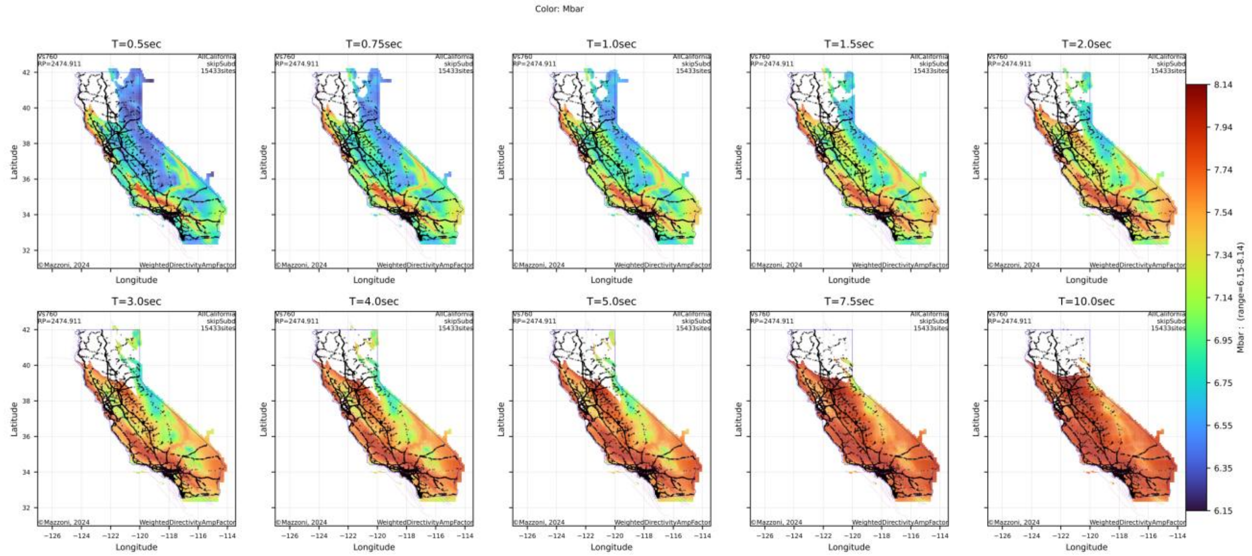

Figure 1-29 *Overlay of Existing-Caltrans-Bridge Locations and Geographic Distribution of Mean Magnitude (Mbar) (Vs30=760m/s, RP=2475yr)*

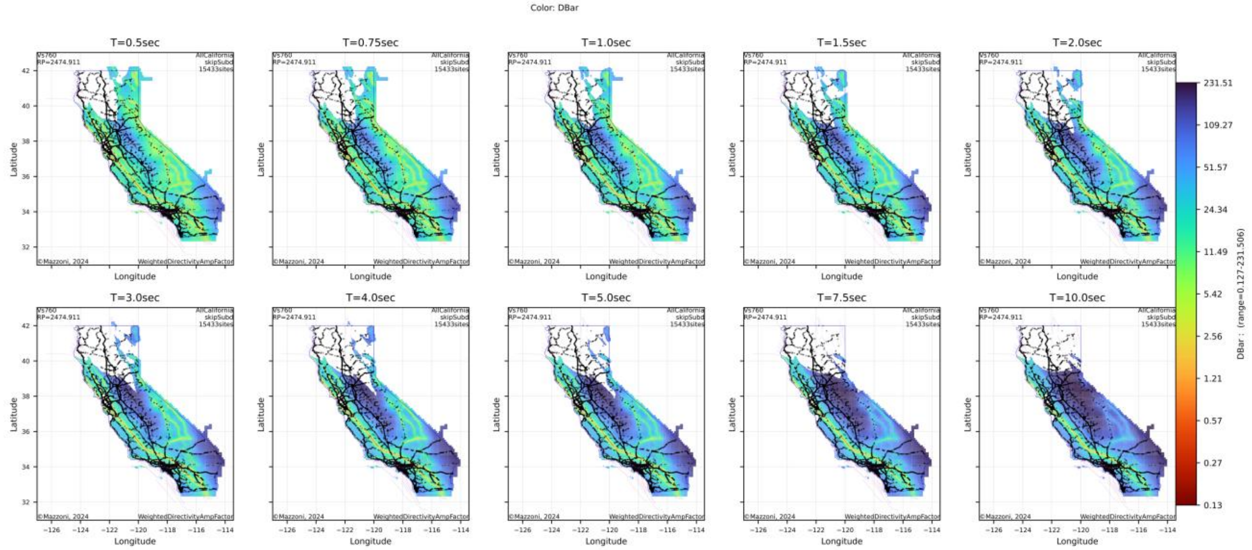

Figure 1-30 *Overlay of Existing-Caltrans-Bridge Locations and Geographic Distribution of Mean Distance (Dbar) (km) (Vs30=760m/s, RP=2475yr)*

1.6.3.3. Magnitude Bins

The datasets were grouped into Magnitude Bins, from Magnitude 6 to 8, in half-magnitude units. The data are shown in **Figure 1-31** and **Figure 1-32** for the modal and mean magnitudes, respectively, for the case of Vs30=760 m/s, return period=2475yr.

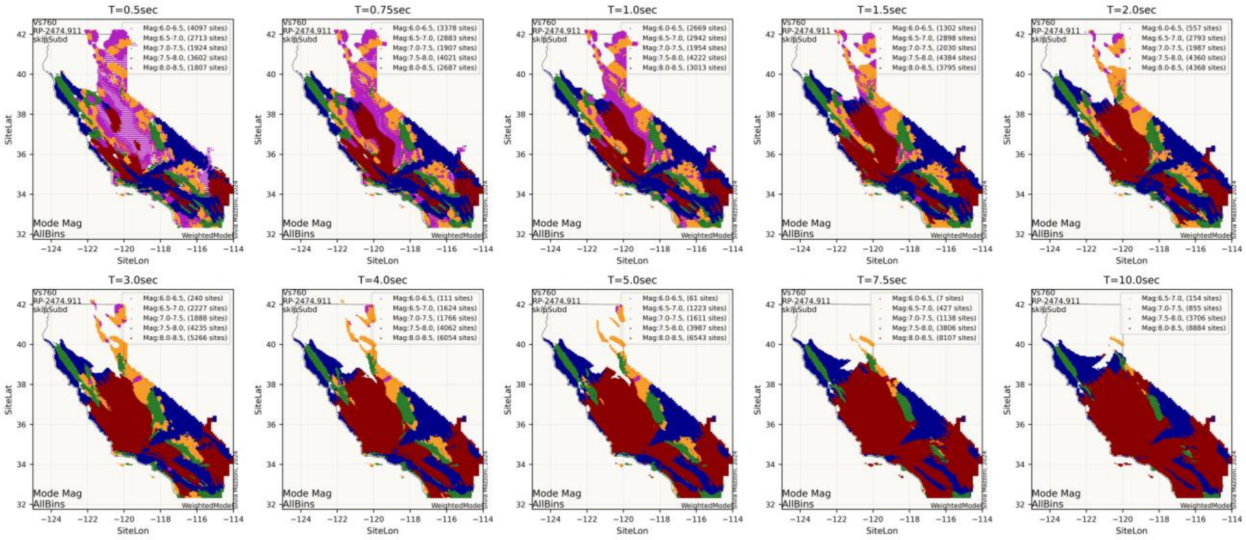

Figure 1-31 Geographic Distribution of Modal-Magnitude Bins (Vs30=760m/s, RP=2475yr)

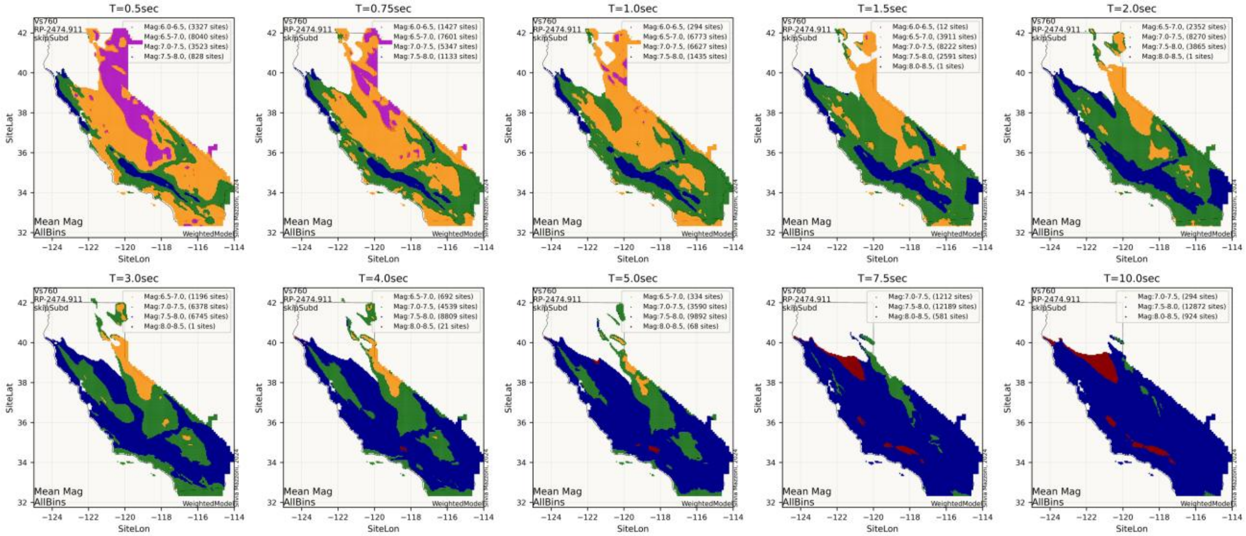

Figure 1-32 Geographic Distribution of Mean-Magnitude Bins (Vs30=760m/s, RP=2475yr)

1.7. PROCEDURE TO UPDATE CALTRANS NEAR-FAULT ADJUSTMENT FACTORS

The following steps were taken to evaluate and refine the current Caltrans Directivity Amplification Factors:

1. Extraction of Dominant Seismic Parameters: For all 19,000+ analysis sites, the magnitude (M) and rupture distance (Rrup) were extracted from the deaggregation results – for both mean and mode.
2. Analysis of Amplification Across Magnitude Bins: The directivity amplification factor was evaluated as a function of Rrup, categorized into magnitude bins:
    - M < 4.5
    - 4.5 ≤ M ≤ 6.5
    - M > 6.5

      This analysis was performed across different return periods and oscillator periods to observe trends and dependencies.
3. Assessment of Rupture Distance Threshold: The effectiveness of the current 15 km threshold for Rrup (used to trigger directivity amplification) was examined to determine if it remains appropriate or requires adjustment.
4. Sensitivity Analysis: The sensitivity of directivity amplification was evaluated with respect to:
    - The directivity model used
    - Return period
    - Oscillator period
    - Rupture distance (Rrup)
5. Evaluation of Inelastic Response Effects: Building on the findings from Bahrampouri et al. (2023), the influence of inelastic response on the effective oscillator period was examined.
    - For each (M, Rrup) bin and a range of pulse periods (Tp), the minimum elastic period where directivity effects remain significant was estimated.
    - These findings were used to assess whether the current 0.5 to 1.0 second period range defined in the Caltrans criteria should be revised.

1.8. DIRECTIVITY-AMPLIFICATION THRESHOLD DISTANCE

The first step in developing a directivity amplification model was the determination of the threshold distance. In this study, this threshold distance was defined as the shortest distance where the directivity amplification factor exceeded 1.05. This value was set with a 5% margin account for rounding errors in computing the directivity amplification factor, which was calculated as the ratio of the PSA with and without directivity considerations.

1.8.1. Computation of the Directivity-Amplification Threshold Distance

A mean and a standard deviation were computed for each dataset for this threshold distance. Even though these data were not explicitly used to develop the recommended Near-Fault Adjustment Factors, these data would help us evaluate our model to ensure that we considered this threshold distance in developing our model. These data is best visualized by plotting the Distance metric (Modal or Mean) on the vertical axis and the directivity amplification on the horizontal axis. **Figure 1-33** through **Figure 1-37** plot these data for all bins in one figure, and the individual Modal-Magnitude bins, one per figure. **Figure 1-38** through **Figure 1-42** plot the same data for the Mean-Magnitude bins.

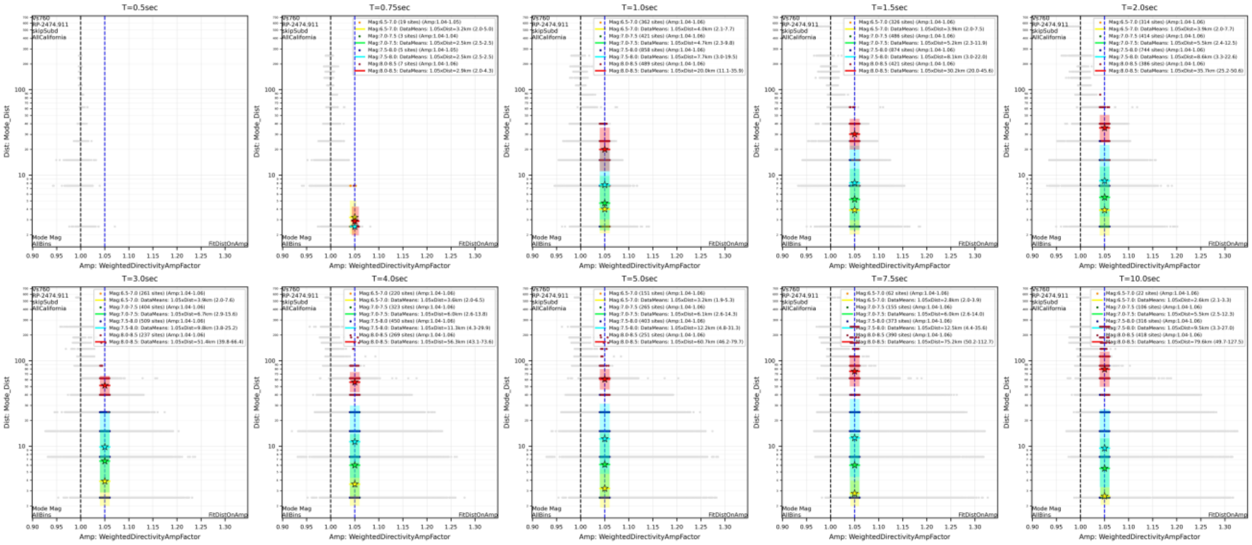

Figure 1-33 *Modal Distance vs Directivity Amplification Factor + Threshold Distance, All Modal-Magnitude Bins.*

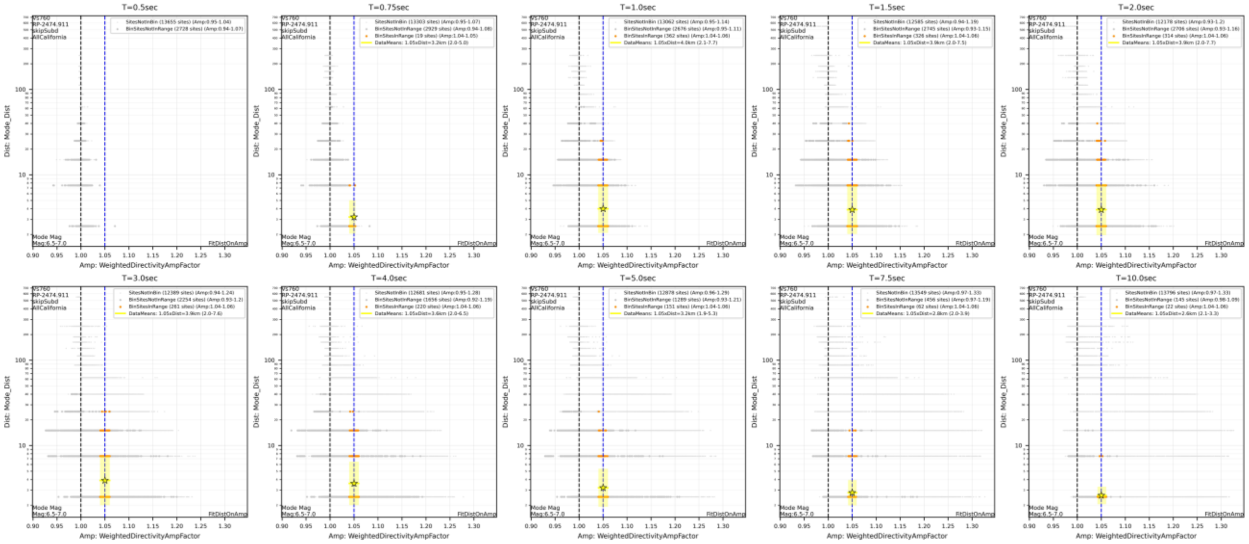

Figure 1-34 *Modal Distance vs Directivity Amplification Factor + Threshold Distance, Modal-Magnitude Bin: 6.5-7.0*

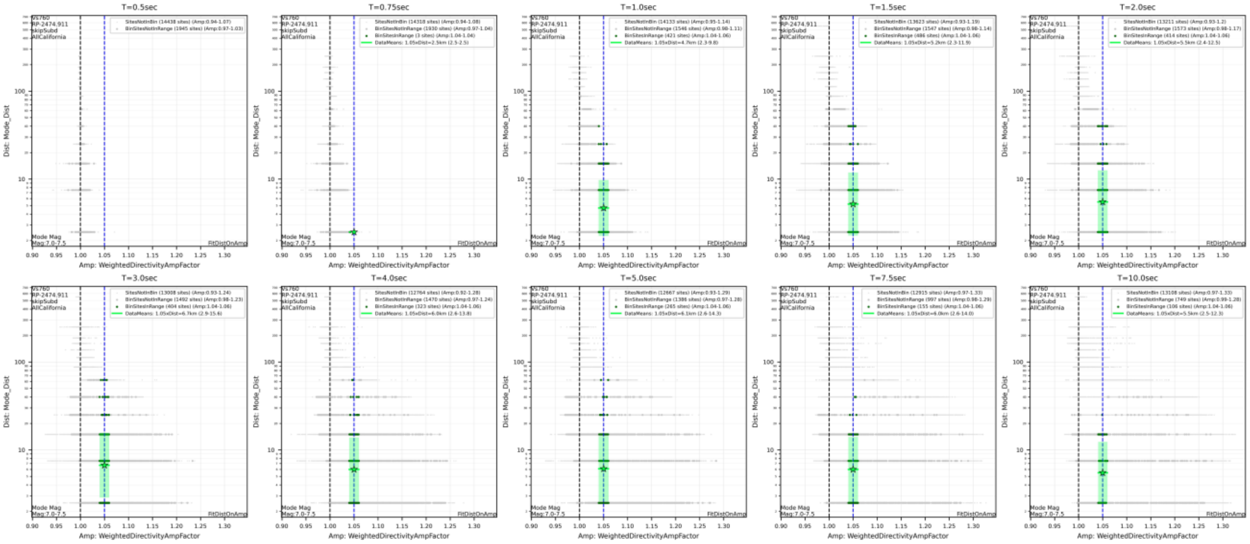

Figure 1-35 *Modal Distance vs Directivity Amplification Factor + Threshold Distance, Modal-Magnitude Bin: 7.0-7.5*

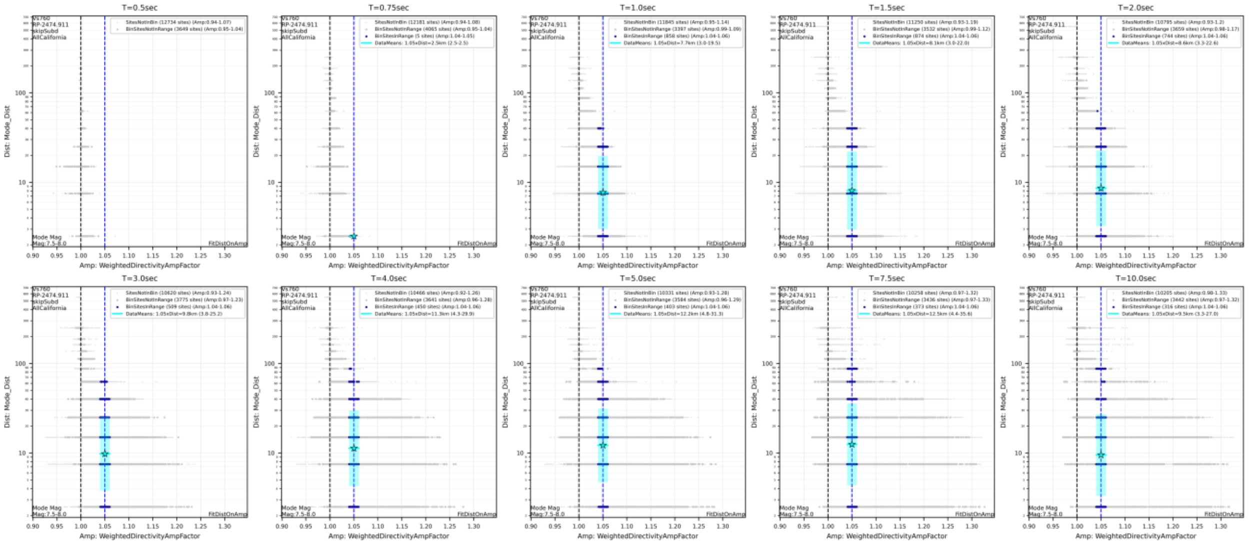

__Figure 1-36__ Modal Distance vs Directivity Amplification Factor + Threshold Distance, Modal-Magnitude Bin: 7.5-8.0

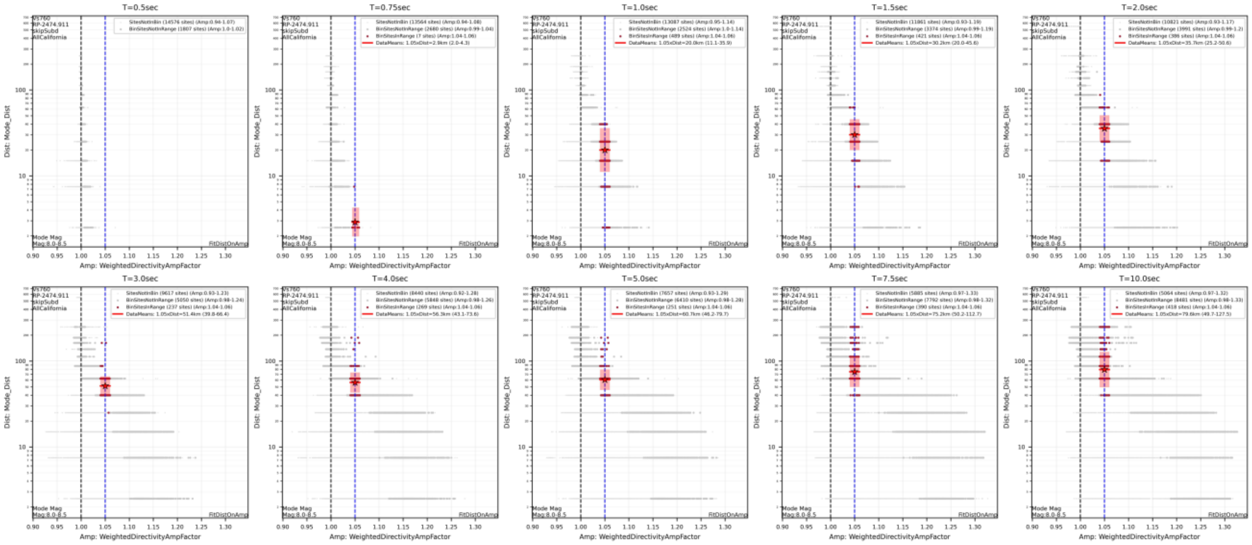

__Figure 1-37__ Modal Distance vs Directivity Amplification Factor + Threshold Distance, Modal-Magnitude Bin: 8.0-8.5

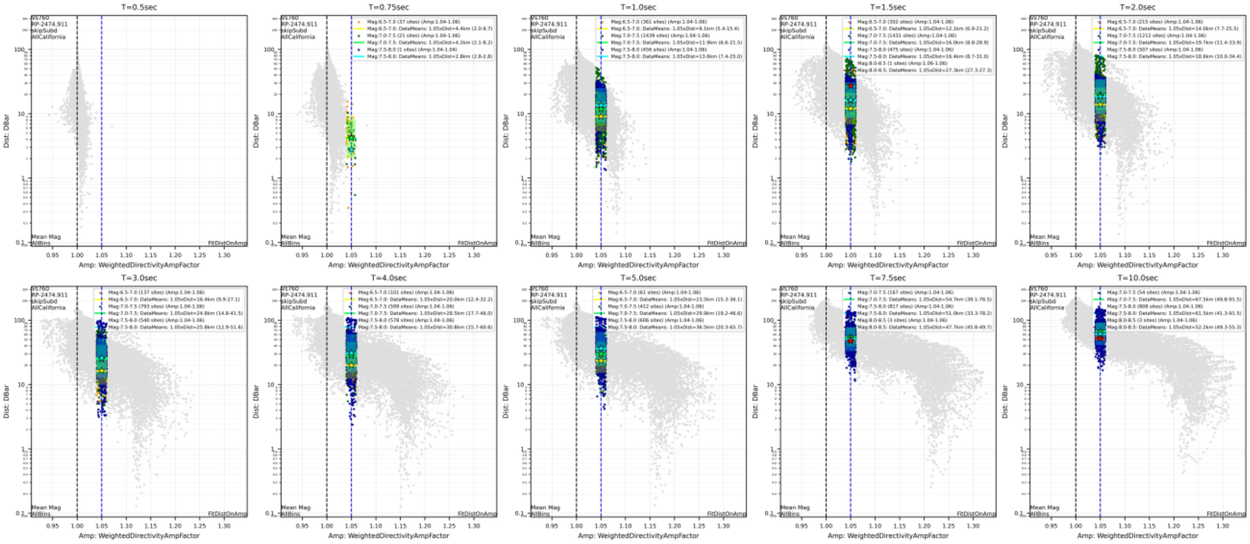

__Figure 1-38__ Mean Distance vs Directivity Amplification Factor + Threshold Distance, Mean-Magnitude Bin: All

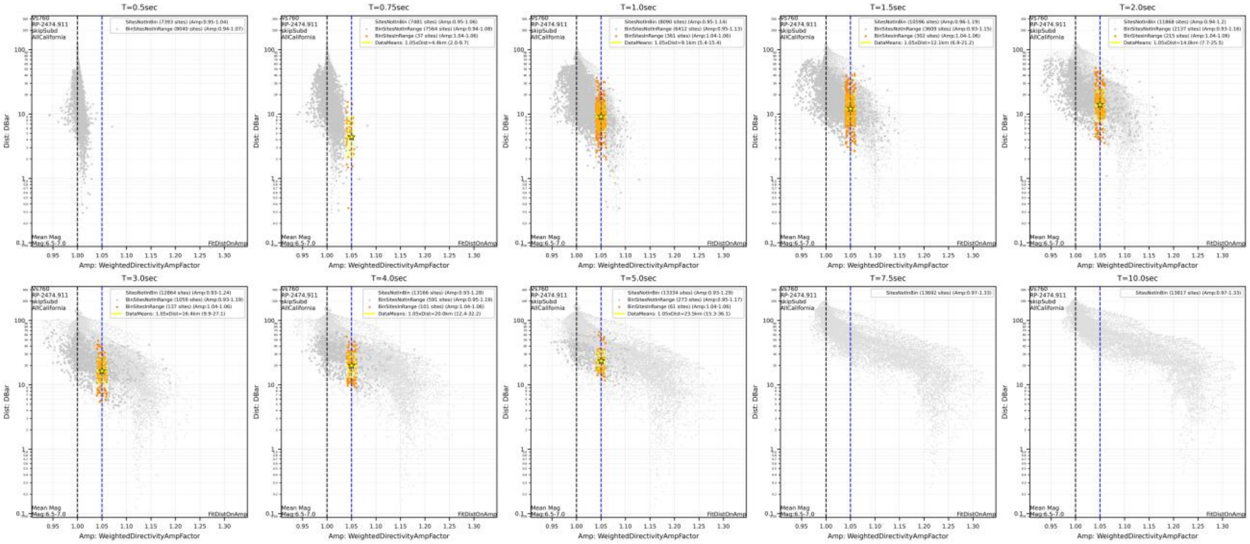

__Figure 1-39__ Mean Distance vs Directivity Amplification Factor + Threshold Distance, Mean-Magnitude Bin: 6.5-7.0

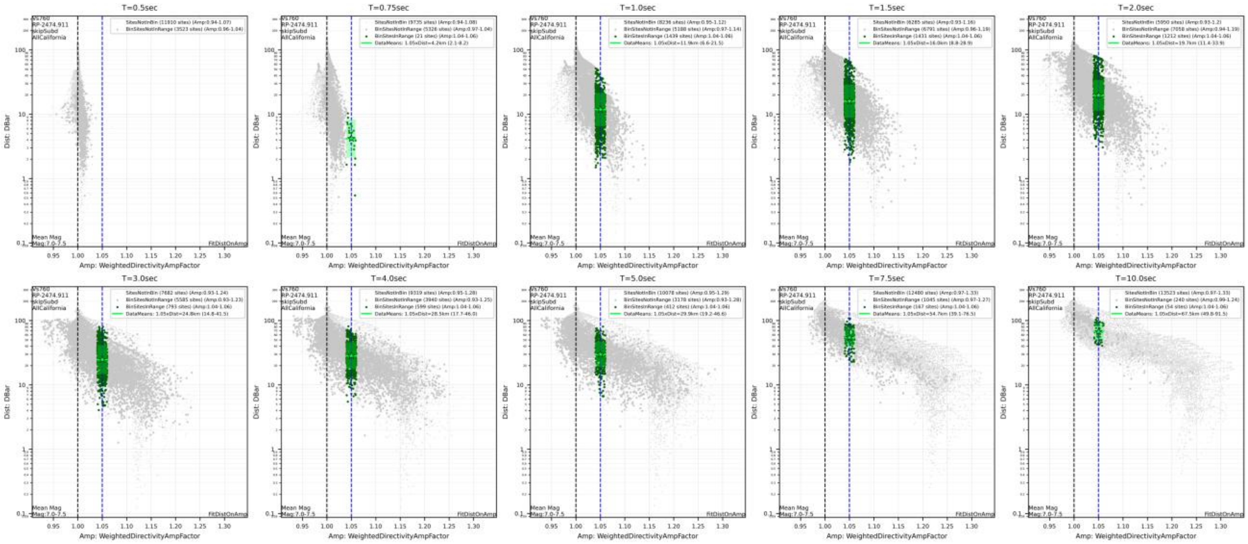

Figure 1-40 *Mean Distance vs Directivity Amplification Factor + Threshold Distance, Mean-Magnitude Bin: 7.0-7.5*

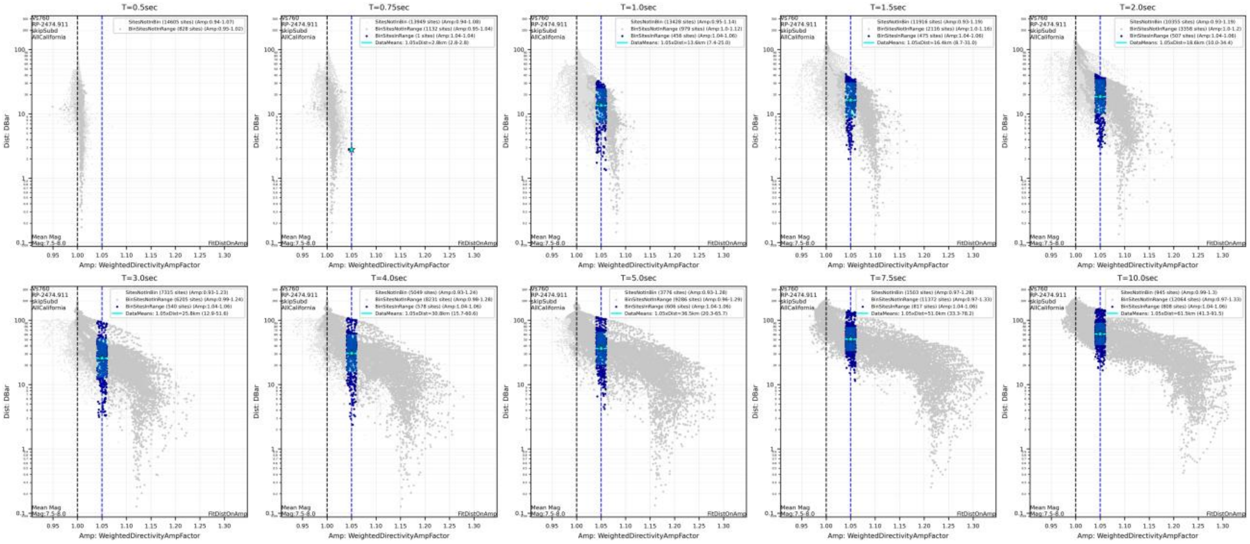

Figure 1-41 *Mean Distance vs Directivity Amplification Factor + Threshold Distance, Mean-Magnitude Bin: 7.5-8.0*

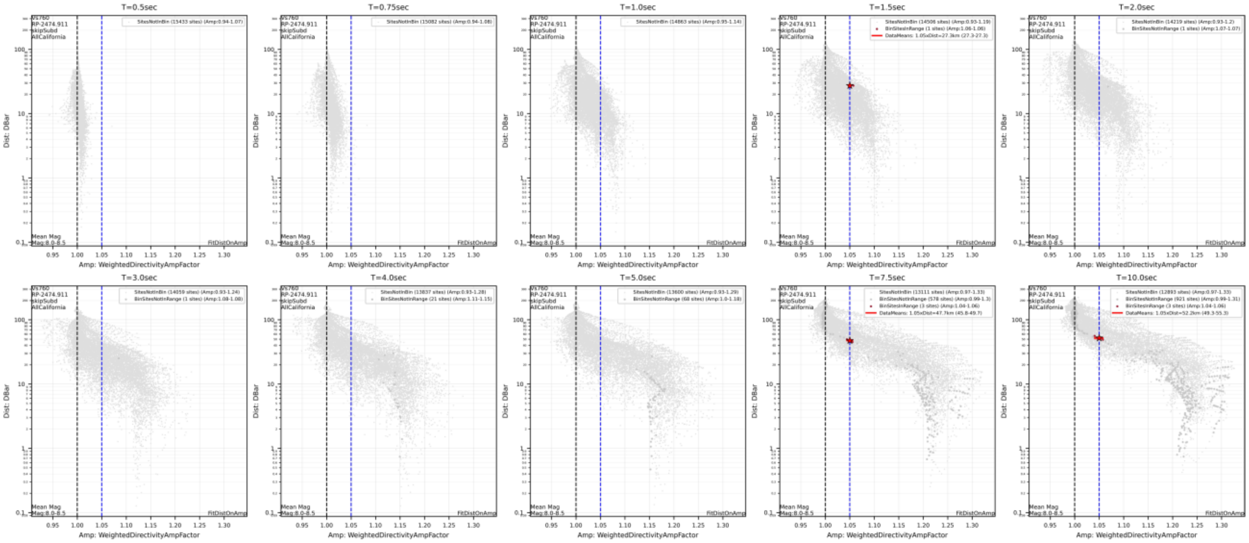

__Figure 1-42__ Mean Distance vs Directivity Amplification Factor + Threshold Distance, Mean-Magnitude Bin: 8.0-8.5

1.8.2. Directivity Threshold Distance vs Period

Figure 1-43 and **Figure 1-44** plot the threshold distance vs period mean and 16-84%ile in separate plots for each magnitude bin, for modal and mean magnitude, respectively. The magnitude bins are collapsed into a single plot in **Figure 1-45** and **Figure 1-46**, for modal and mean magnitude, respectively. Please note that the range of the vertical axes are the same within each figure, but have different ranges for modal and mean magnitude. A comparison of the latter 2 figures demonstrates the difference between the modal distance (corresponding to the magnitude and distance of the largest contributor to hazard), and mean distance (averaged over all scenarios considered in the PSHA).

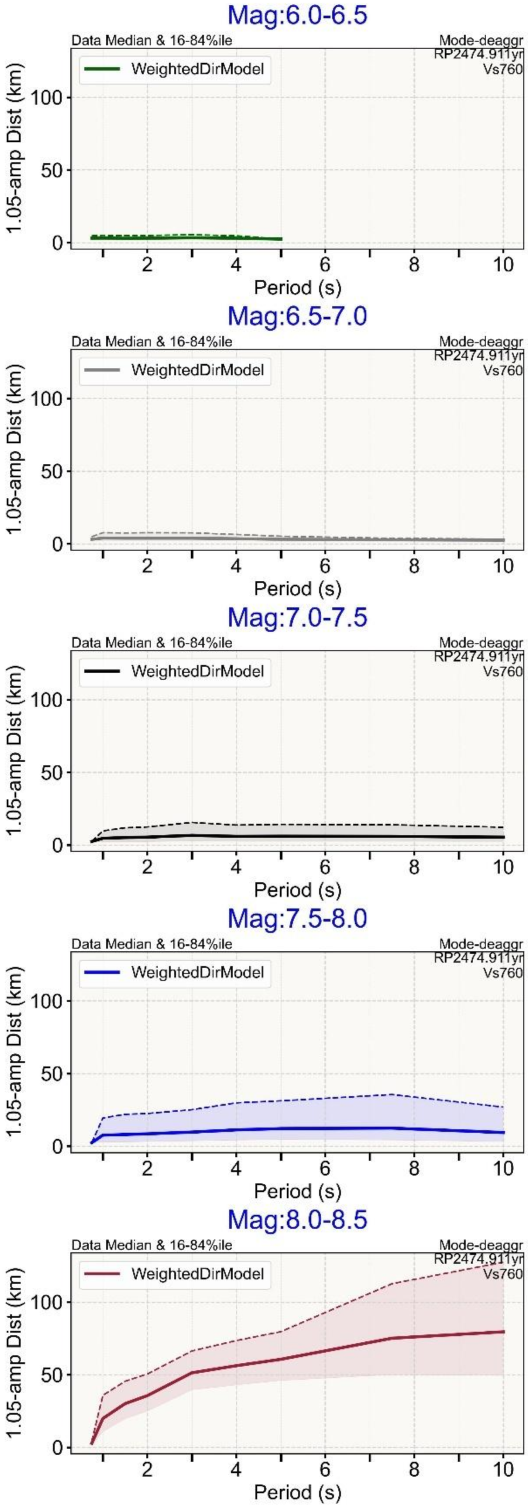

Figure 1-43 *Threshold Distance (1.05-amplification) -- Median +/- sigma. Separate* ***Modal****-Magnitude Bins*

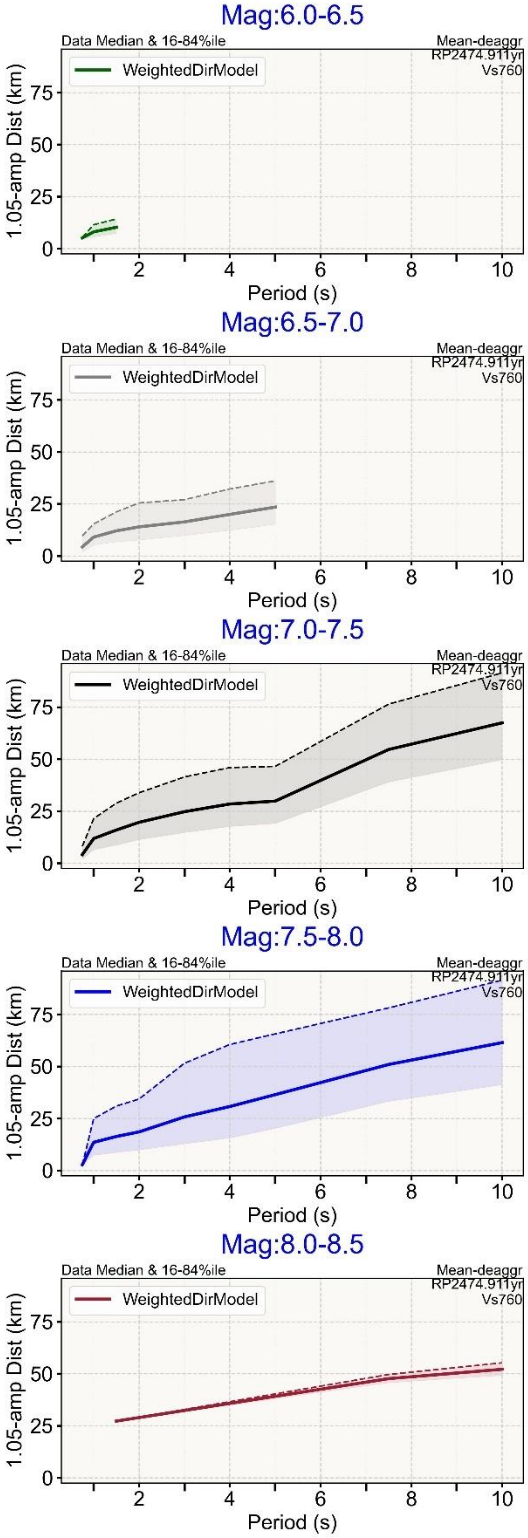

Figure 1-44 *Threshold Distance (1.05-amplification) -- Median +/- sigma. Separate **Mean**-Magnitude Bins*

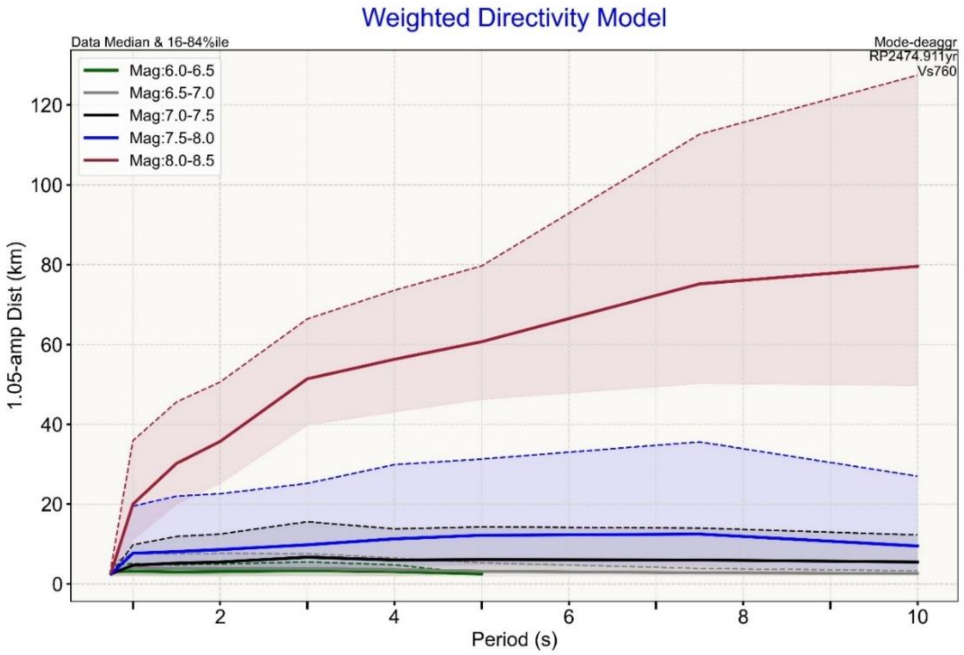

Figure 1-45 *Threshold Distance (1.05-amplification) -- Median +/- sigma. Combined* ***Modal****-Magnitude Bins*

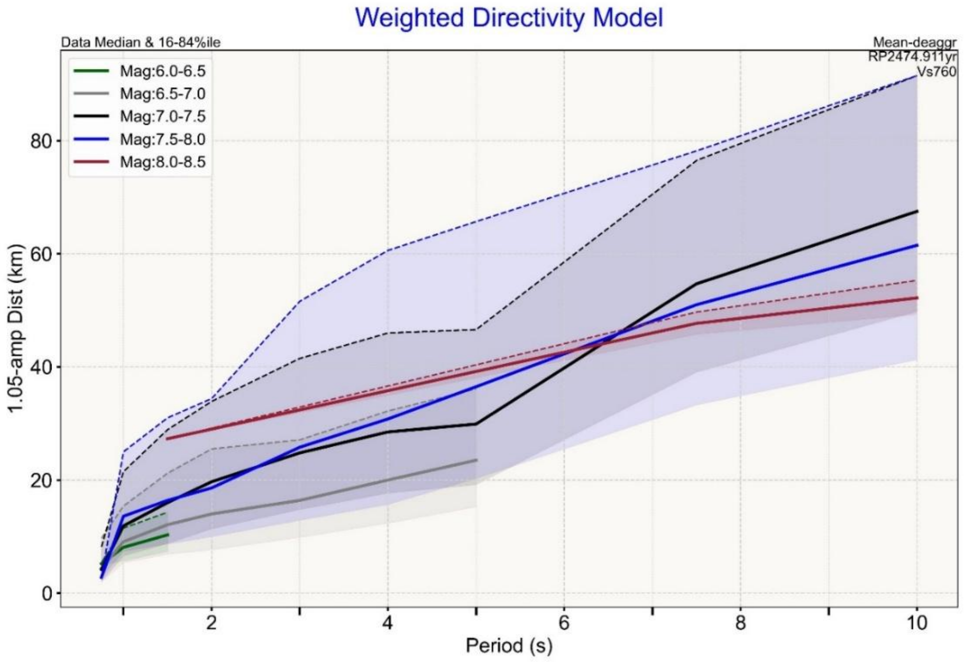

Figure 1-46 *Threshold Distance(1.05-amplification) -- Median +/- sigma. Combined* ***Mean****-Magnitude Bins*

1.9. DIRECTIVITY AMPLIFICATION FACTOR VS DISTANCE

1.9.1. Mode

The Directivity Amplification Factor (Weighted Model) is plotted vs Distance for each oscillator period and different magnitude bins using the Modal magnitude and distance is shown **Figure 1-47** through **Figure 1-52**. The first figure in the set shows the entire dataset: Modal Magnitude 6.5 and above. The subsequent figures show the individual magnitude bins. Please note that while the vertical axis has the same range for all period plots in each figure, it differs between each figure. This set of figures show that amplification is both distance and period dependent, as well as magnitude dependent. As noted earlier, the mean distance from deaggregation is not a realistic measure, so it will not be shown in this report. The figures correspond to a Vs30=760m/s and a return period of 2475 year. These values were selected as they are considered reference values.

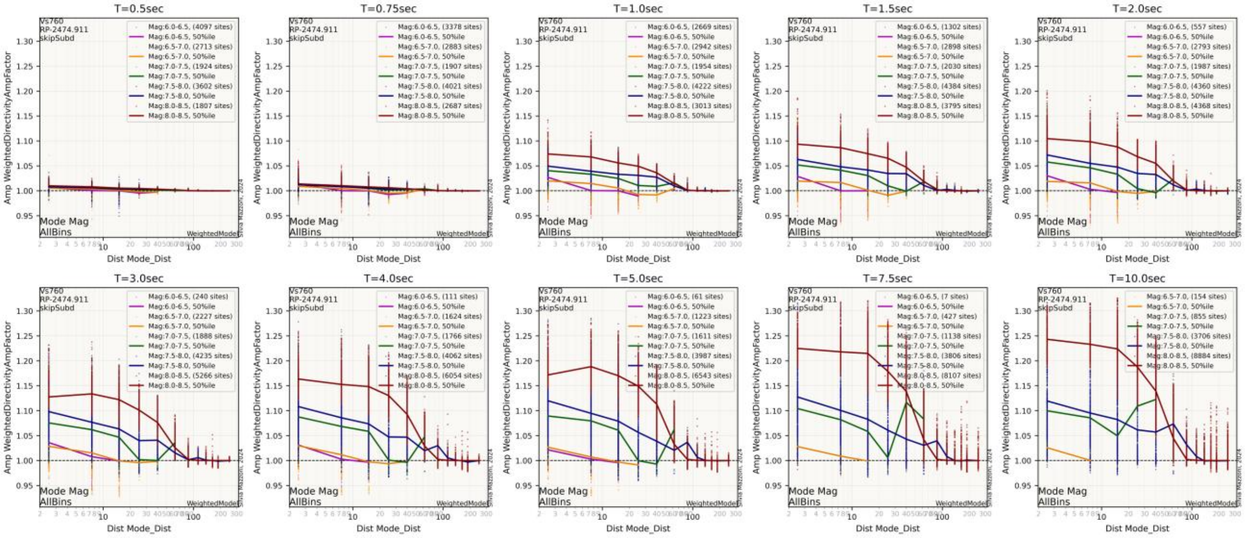

Figure 1-47 *Directivity Amplification Factor vs Modal Distance. Full dataset Modal Magnitude>= 6.0*

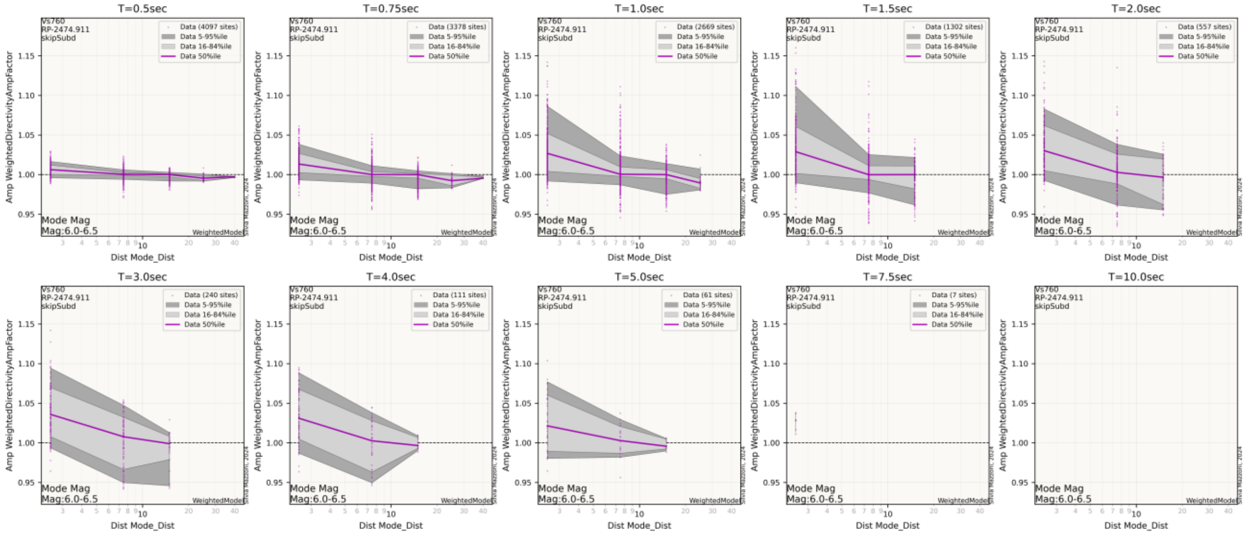

Figure 1-48 Directivity Amplification Factor vs Modal Distance. Modal-Magnitude Bin: 6.0-6.5

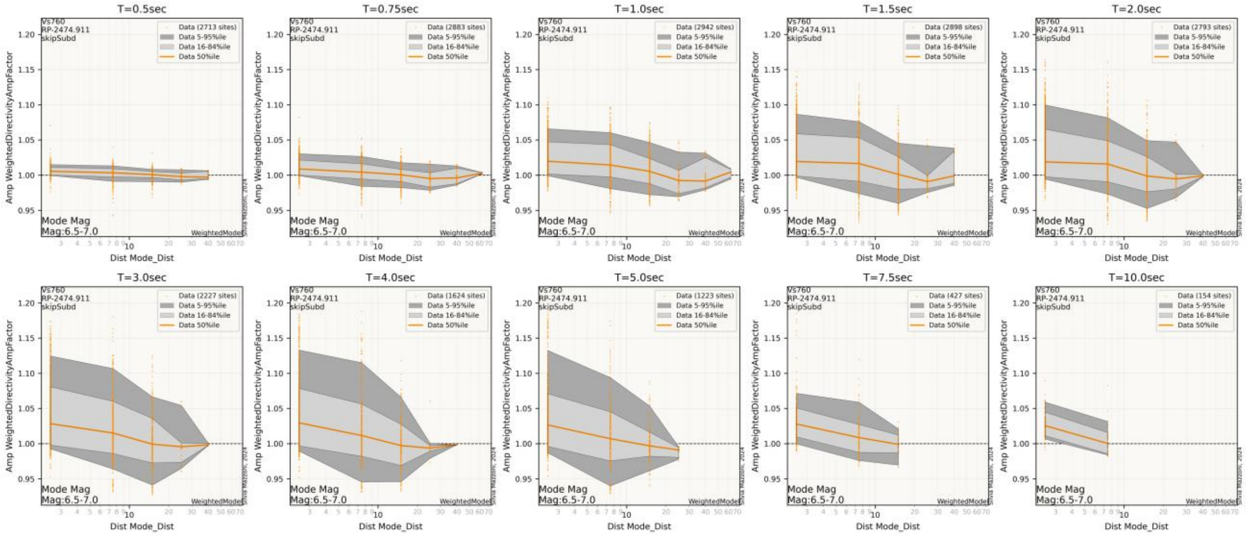

Figure 1-49 Directivity Amplification Factor vs Modal Distance. Modal-Magnitude Bin: 6.5-7.0

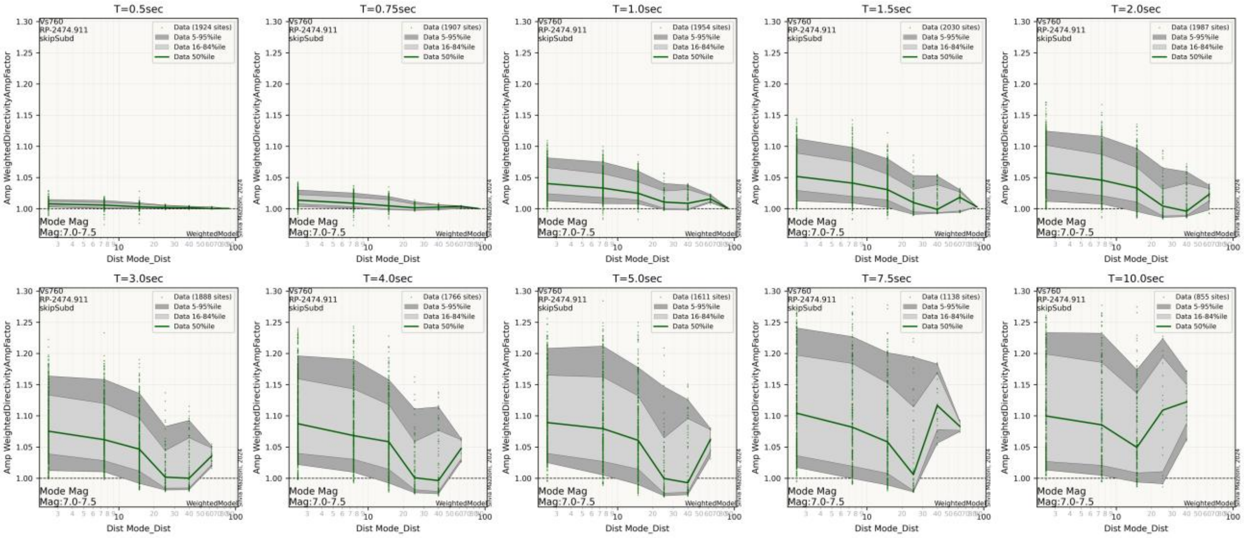

Figure 1-50 *Directivity Amplification Factor vs Modal Distance. Modal-Magnitude Bin: 7.0-7.5*

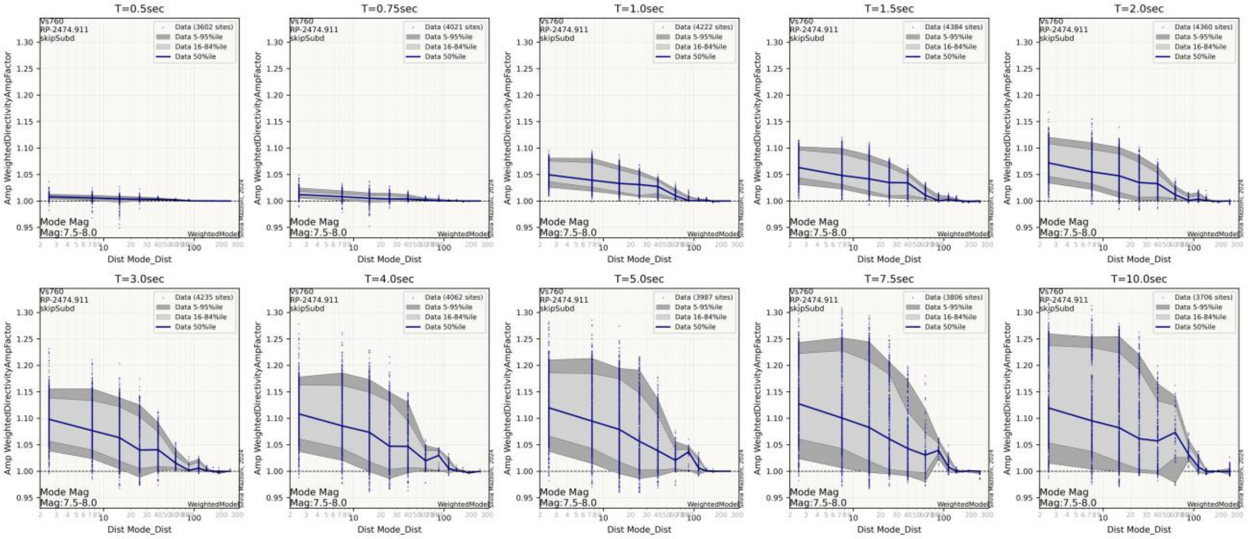

Figure 1-51 *Directivity Amplification Factor vs Modal Distance. Modal-Magnitude Bin: 7.5-8.0*

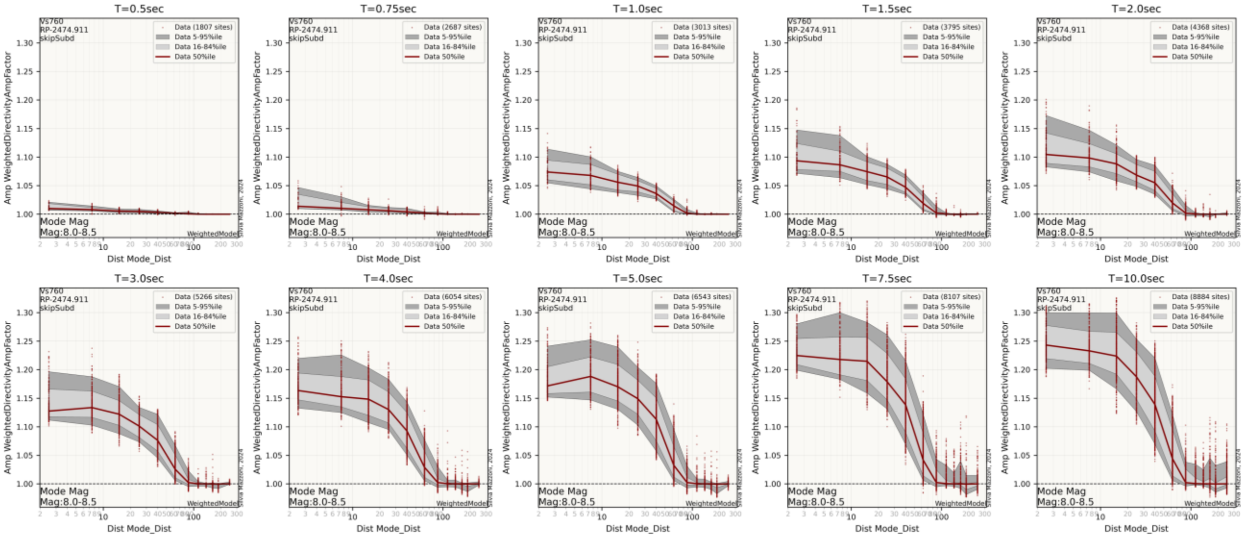

Figure 1-52 *Directivity Amplification Factor vs Distance. Modal Modal-Magnitude Bin: 8.0-8.5*

1.9.2. Mean

The Directivity Amplification Factor is plotted as a function of distance for the Mean-Deaggregation data in **Figure 1-53** through **Figure 1-58**. Both mean magnitude (Mbar) and mean distance (Dbar) values are unique to each site, resulting in a different data distribution than the modal-deaggregation data.

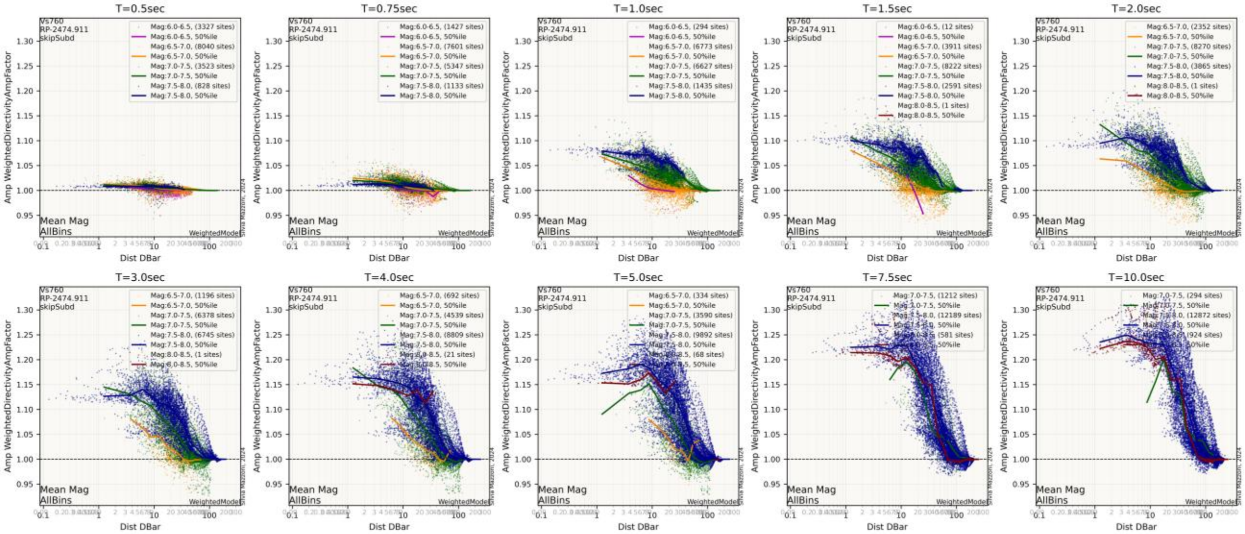

__Figure 1-53__ Directivity Amplification Factor vs Mean Distance. Full dataset Mean Magnitude>= 6.5

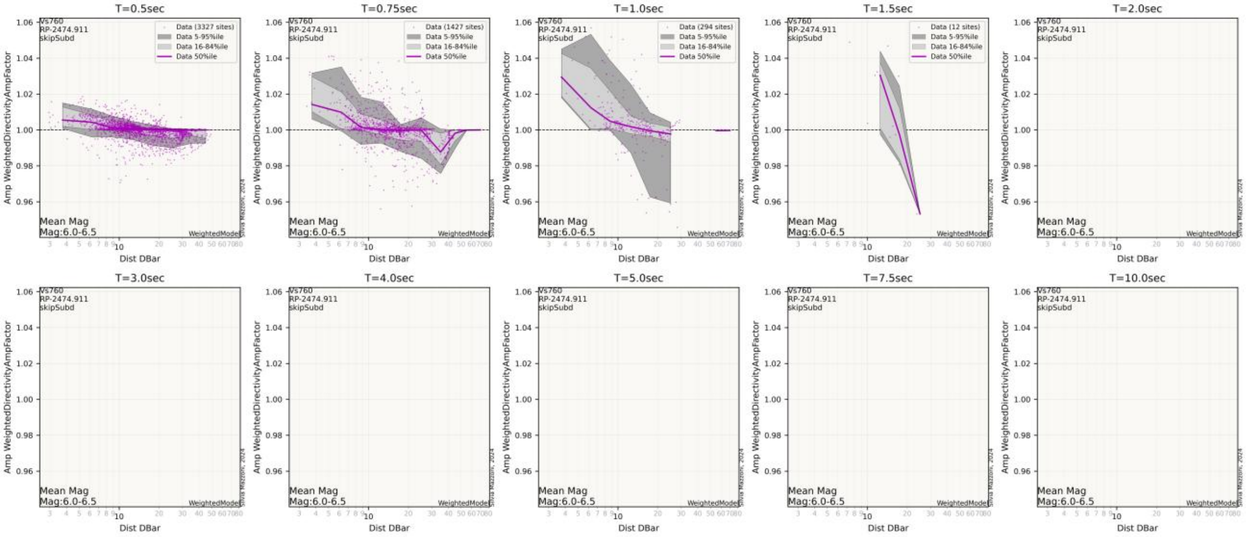

__Figure 1-54__ Directivity Amplification Factor vs Mean Distance. Mean-Magnitude Bin: 6.0-6.5

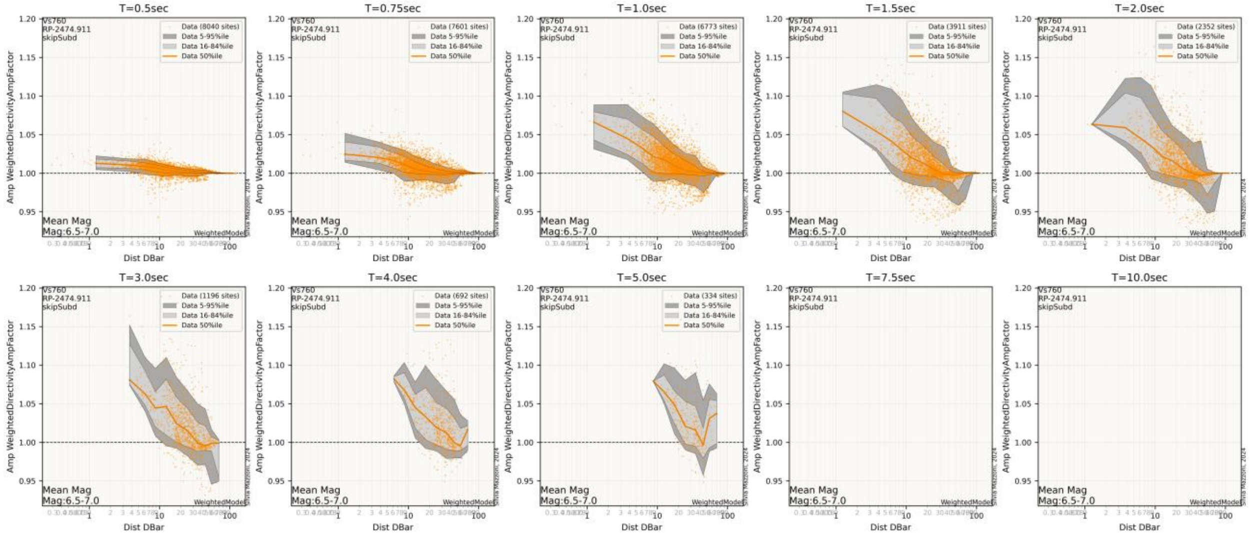

Figure 1-55 Directivity Amplification Factor vs Mean Distance. Mean-Magnitude Bin: 6.5-7.0

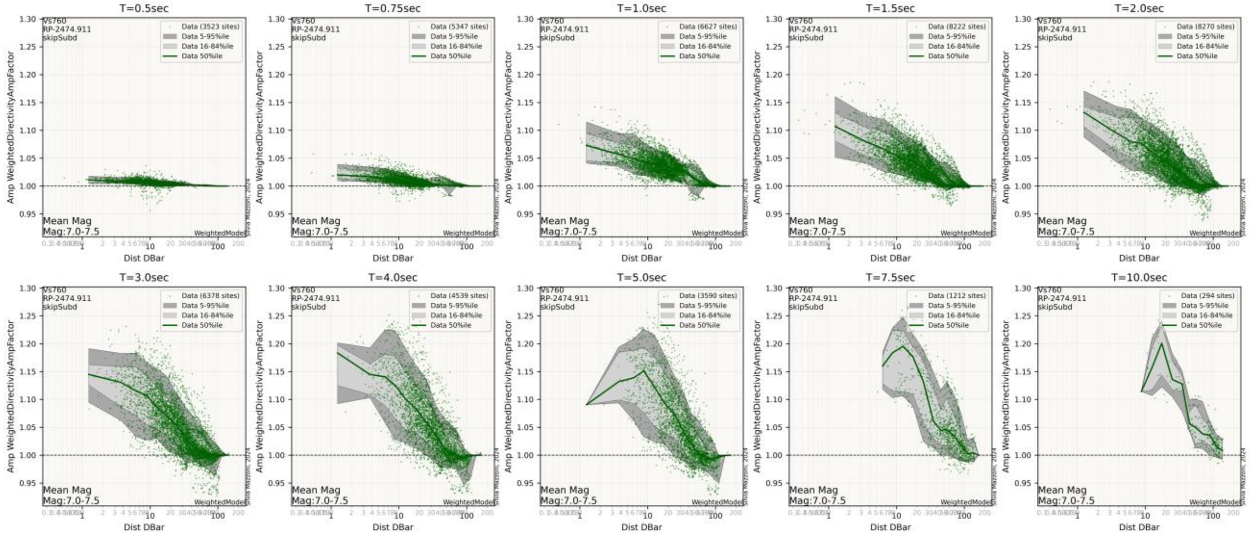

Figure 1-56 Directivity Amplification Factor vs Mean Distance. Mean-Magnitude Bin: 7.0-7.5

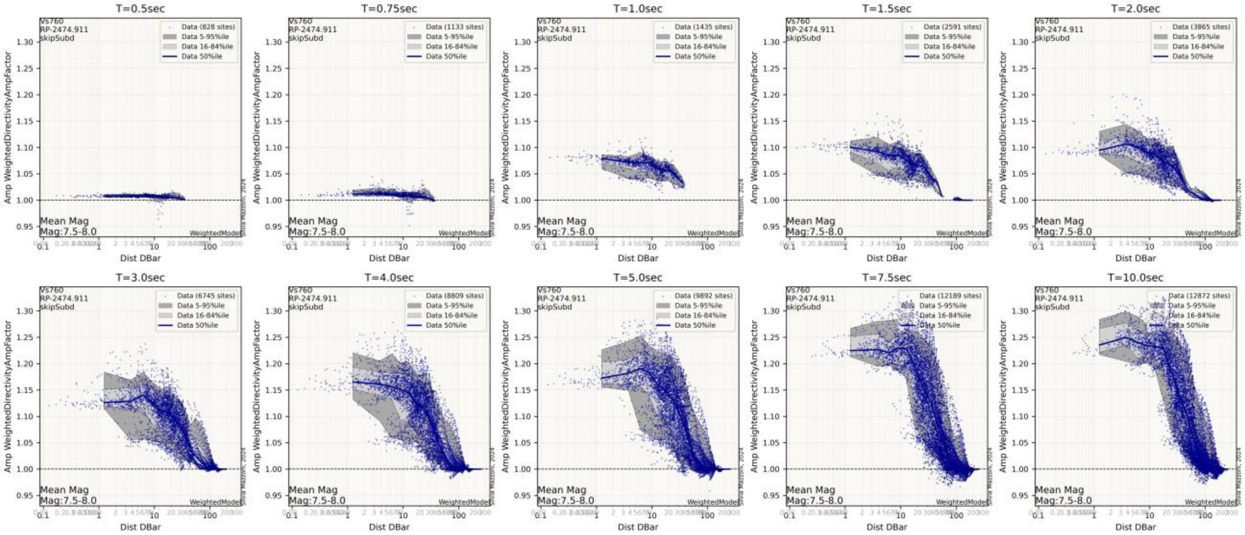

Figure 1-57 *Directivity Amplification Factor vs Mean Distance. Mean-Magnitude Bin: 7.5-8.0*

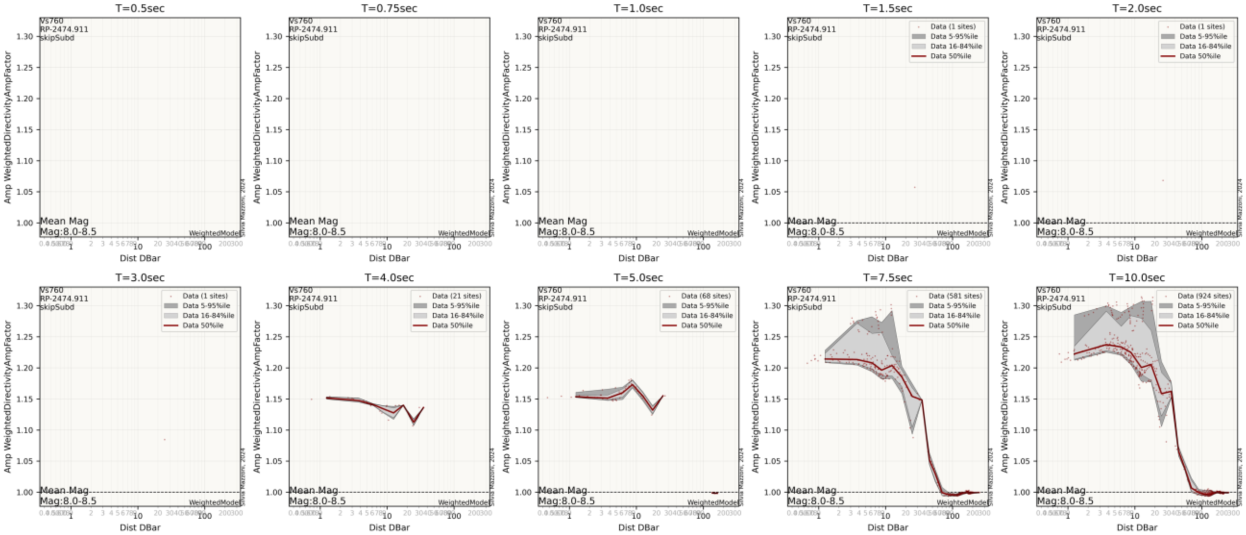

Figure 1-58 *Directivity Amplification Factor vs Mean Distance. Mean-Magnitude Bin: 8.0-8.5*

1.10. MODEL FOR DIRECTIVITY-AMPLIFICATION VS DISTANCE BINNED BY PERIOD AND MAGNITUDE

The data presented in the previous section were used to develop a model for the Directivity Amplification Factor (DAF) as a function of distance, grouped by magnitude and oscillator period bins. The model was based on the modal magnitude and distance obtained from hazard deaggregation, enabling estimation of both the mean and standard deviation of the amplification factor for each bin.

Given the observed behavior of amplification with distance—characterized by elevated amplification at short distances and diminishing effects at greater distances—we selected a hinged-type functional form. This formulation features a constant amplification plateau near the fault and a gradual transition (linear function of the log of the distance) to zero amplification at larger distances. A regression analysis was performed to determine the optimal parameters of the function by minimizing the mean squared error relative to the binned mean values.

1.10.1. Mode

Figure 1-59 presents all binned DAF vs Modal Distance models for the Modal Magnitude bins plotted on a consistent scale for direct comparison. Each curve is shown alongside the corresponding study data and the existing Caltrans SDC directivity amplification factor, which does not vary with magnitude. The figure also identifies the distance at which each model intersects a DAF of 1.05 (indicating a 5% amplification). This threshold is used to define the distance beyond which directivity effects are considered quantifiable, as amplification levels below this point may fall within numerical uncertainty or rounding error.

Figure 1-60 through Figure 1-64 present the directivity amplification models for individual magnitude bins. These figures demonstrate that the simplified models effectively capture both the mean and standard deviation of the amplification across all modal magnitude and oscillator period bins, showing strong agreement with the binned data.

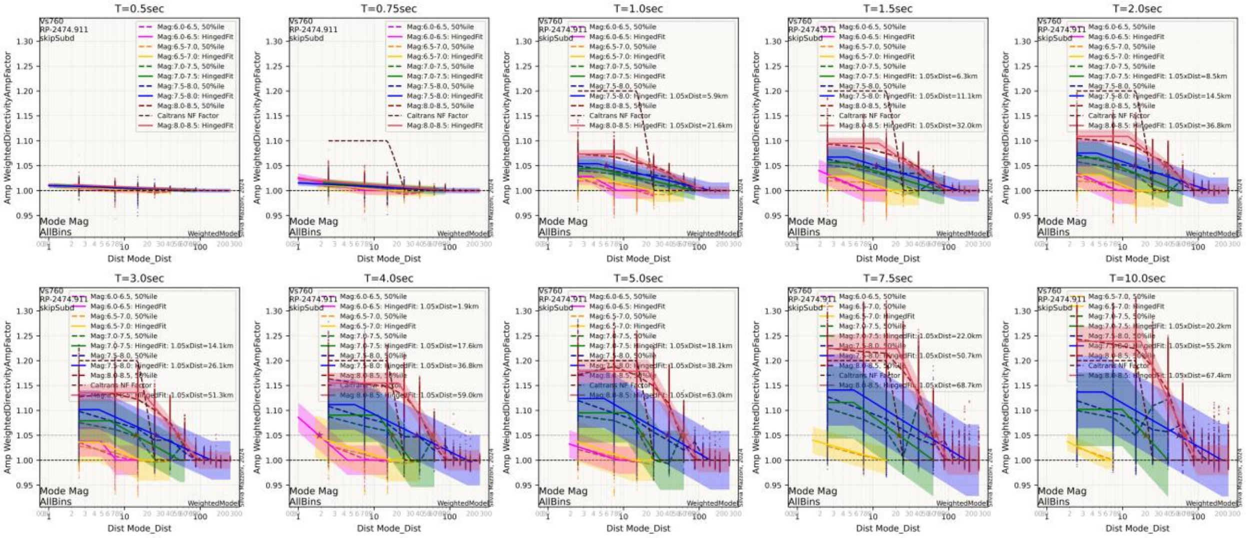

Figure 1-59 *Directivity Amplification vs Modal Distance Models -- all Modal-Magnitude Bins*

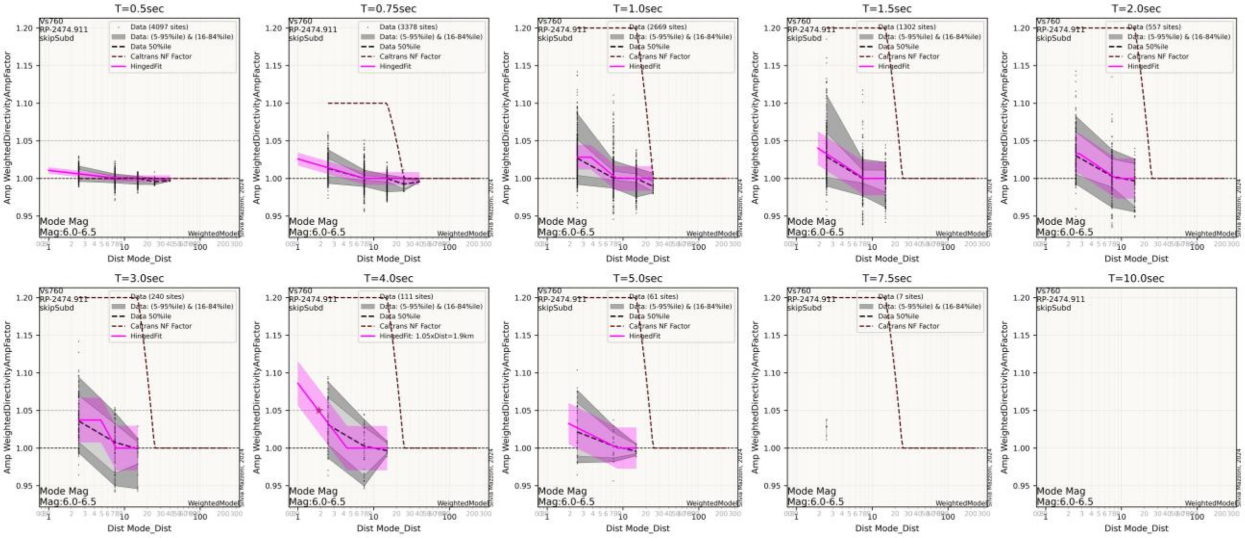

Figure 1-60 *Directivity-Amplification vs Modal Distance Models -- Modal-Magnitude Bin: 6.0-6.5*

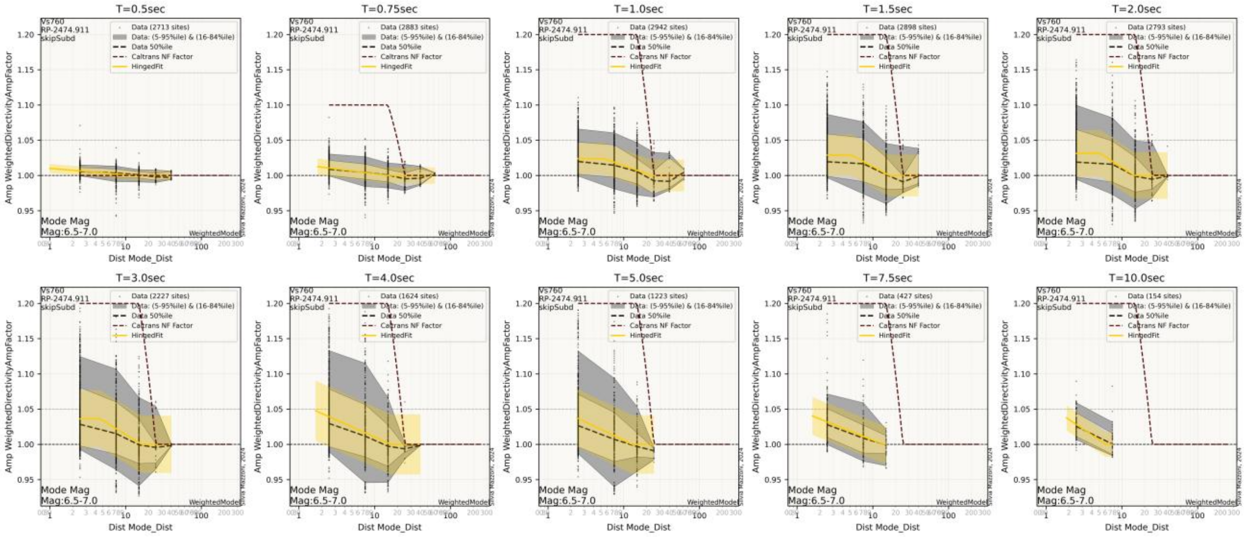

__Figure 1-61__ Directivity-Amplification vs Modal Distance Models -- Modal-Magnitude Bin: 6.5-7.0

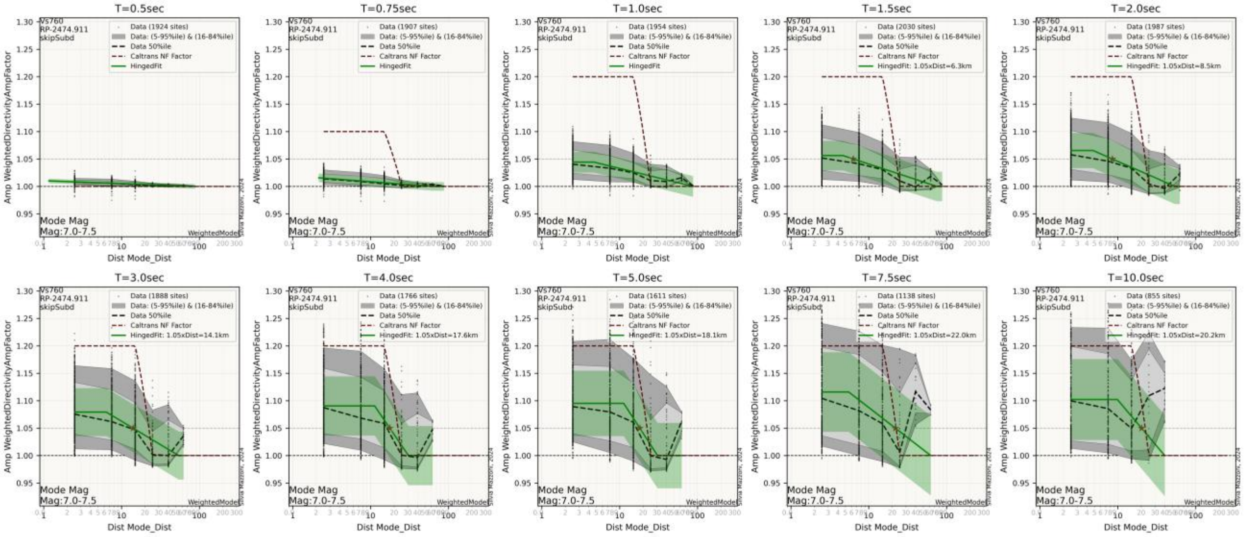

__Figure 1-62__ Directivity-Amplification vs Modal Distance Models -- Modal-Magnitude Bin: 7.0-7.5

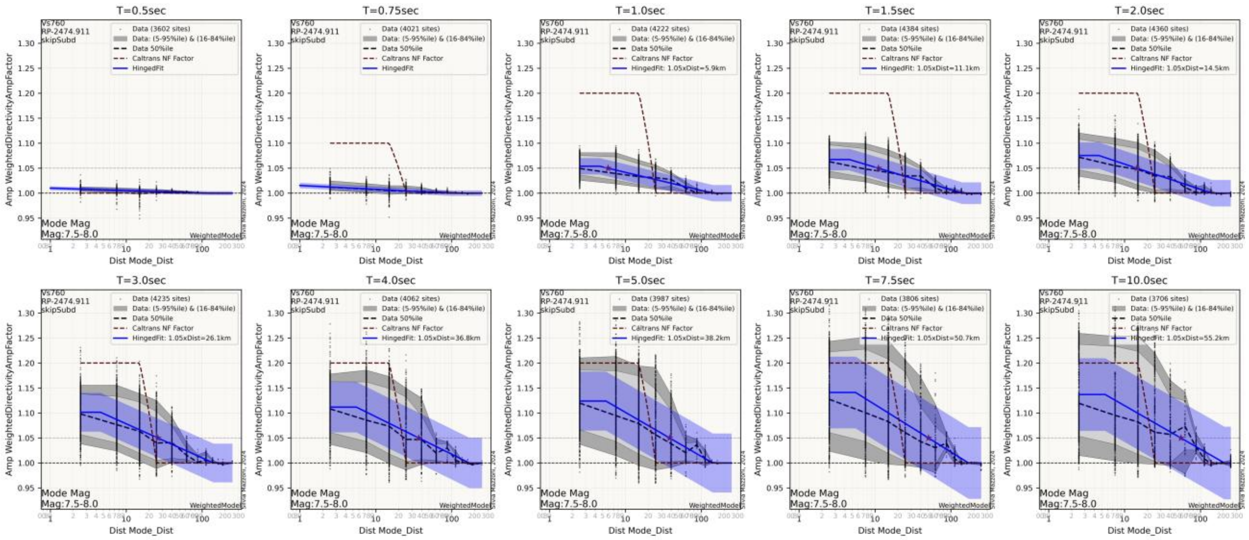

Figure 1-63 *Directivity-Amplification vs Modal Distance Models -- Modal-Magnitude Bin: 7.5-8.0*

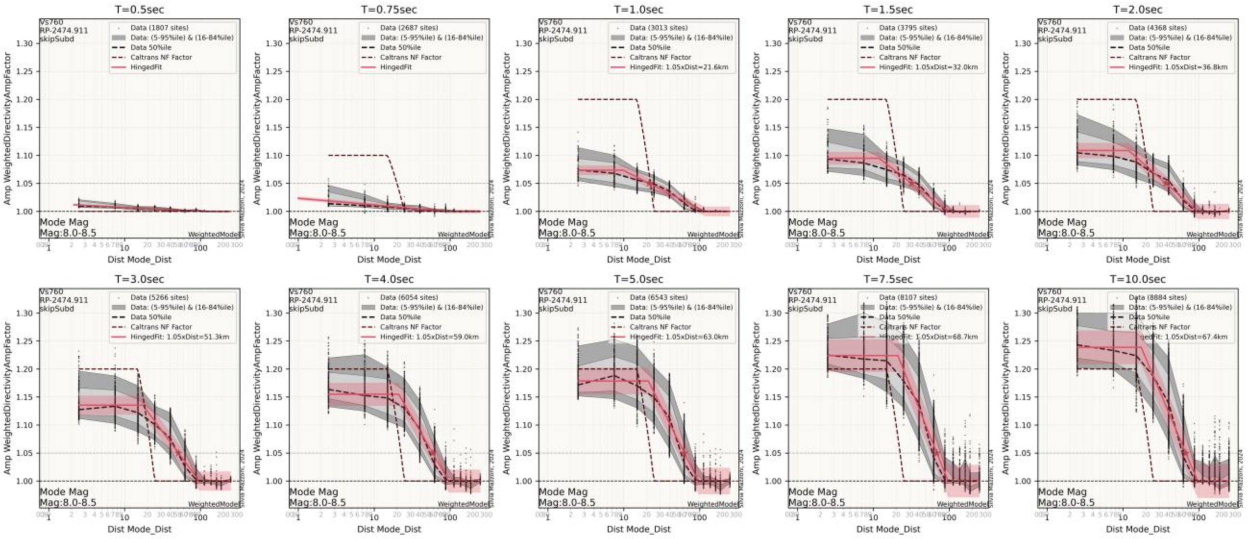

Figure 1-64 *Directivity-Amplification vs Modal Distance Models -- Modal-Magnitude Bin: 8.0-8.5*

1.10.2. Mean

The models for the directivity-amplification factor as a function of Mean Distance (Dbar) for all Mean-Magnitude (Mbar) bins are compared to the data in **Figure 1-65**. **Figure 1-66** through **Figure 1-70** compare the models to the data for the individual bins.

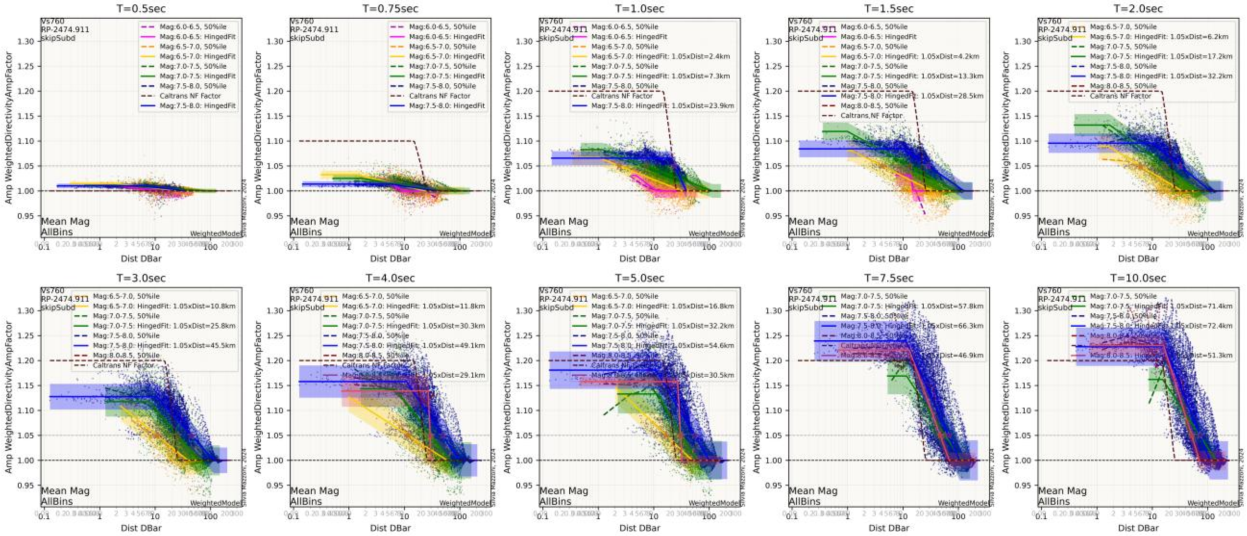

Figure 1-65 Directivity-Amplification vs Mean Distance Models -- All Mean-Magnitude Bins Mbar>6.5

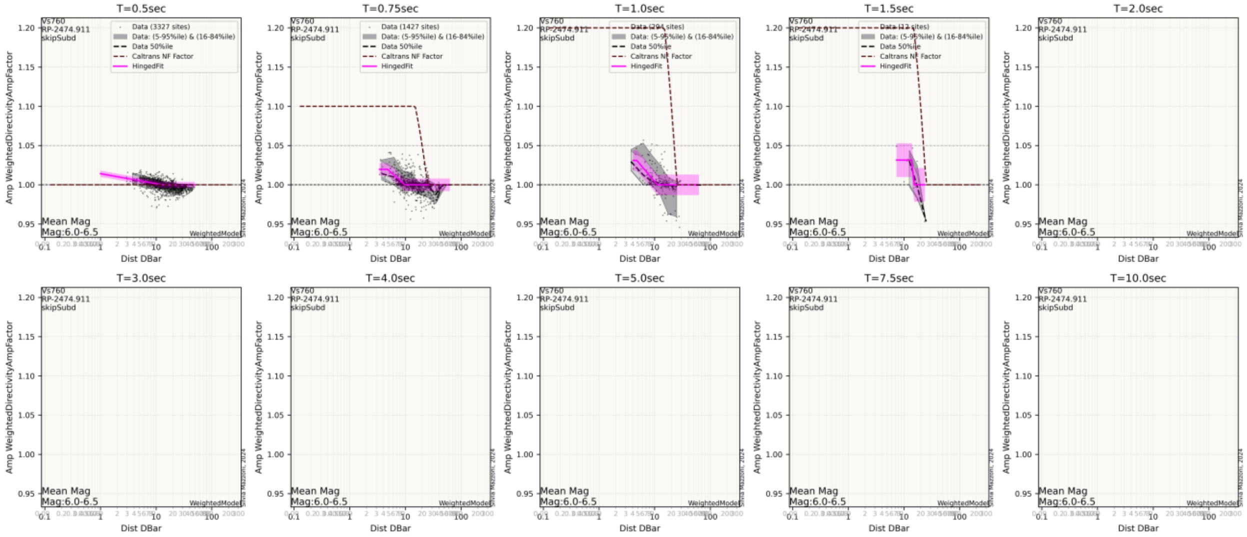

Figure 1-66 Directivity-Amplification vs Mean Distance Models -- Mean-Magnitude Bin: 6.0-6.5

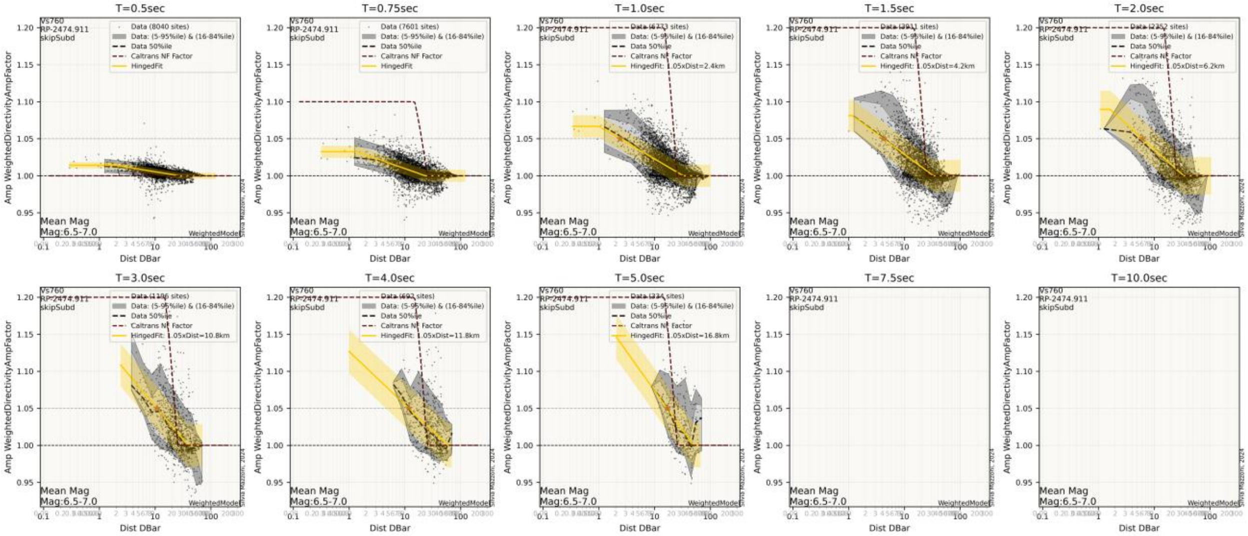

__Figure 1-67__ Directivity-Amplification vs Mean Distance Models -- Mean-Magnitude Bin: 6.5-7.0

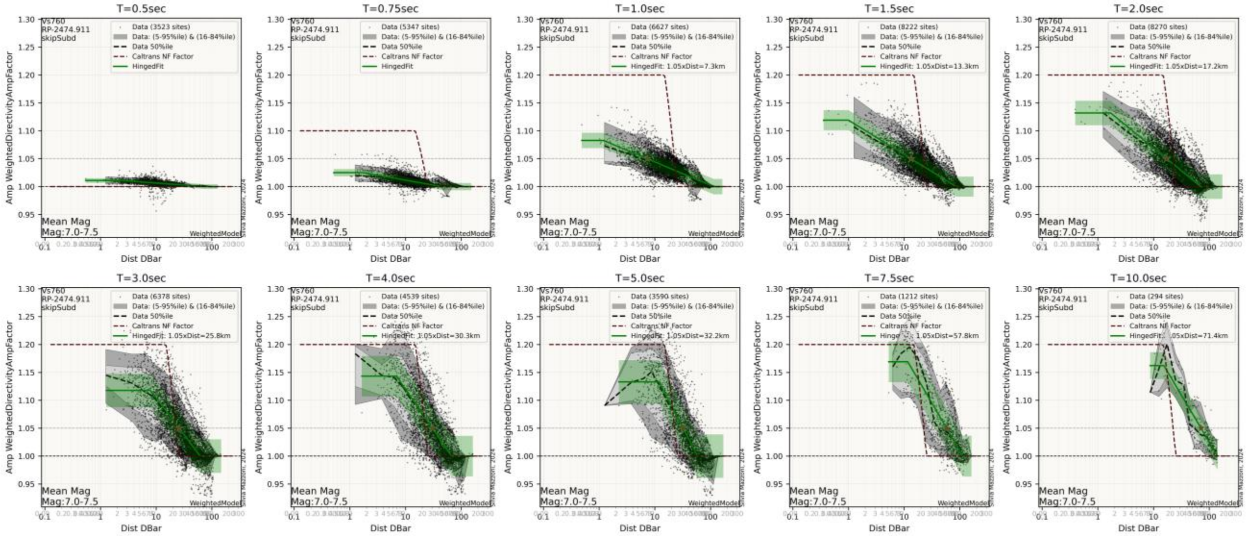

__Figure 1-68__ Directivity-Amplification vs Mean Distance Models -- Mean-Magnitude Bin: 7.0-7.5

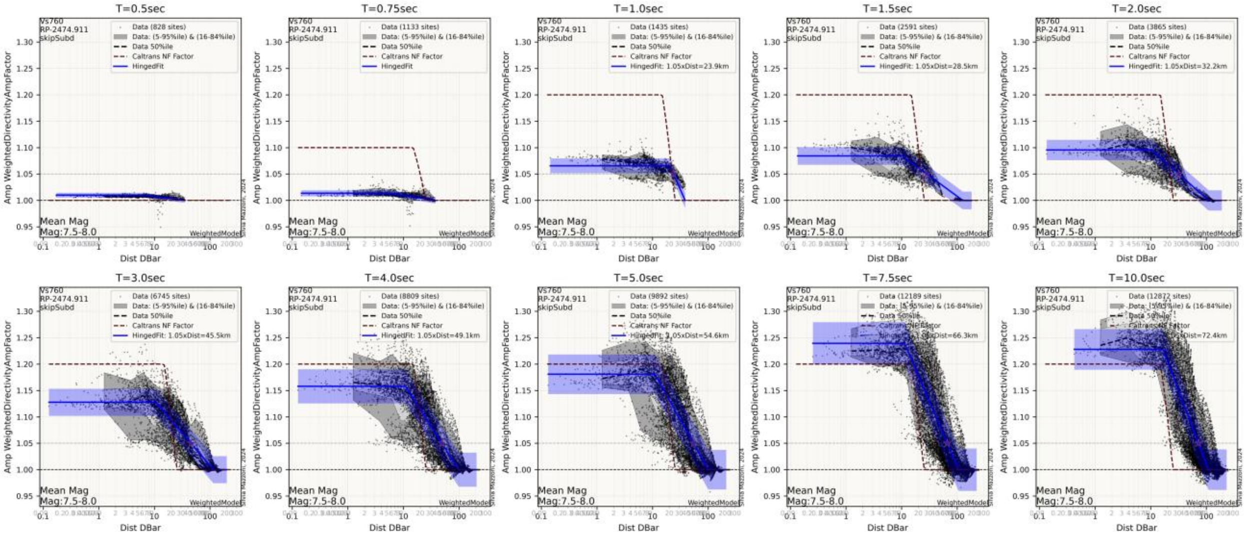

Figure 1-69 *Directivity-Amplification vs Mean Distance Models -- Mean-Magnitude Bin: 7.5-8.0*

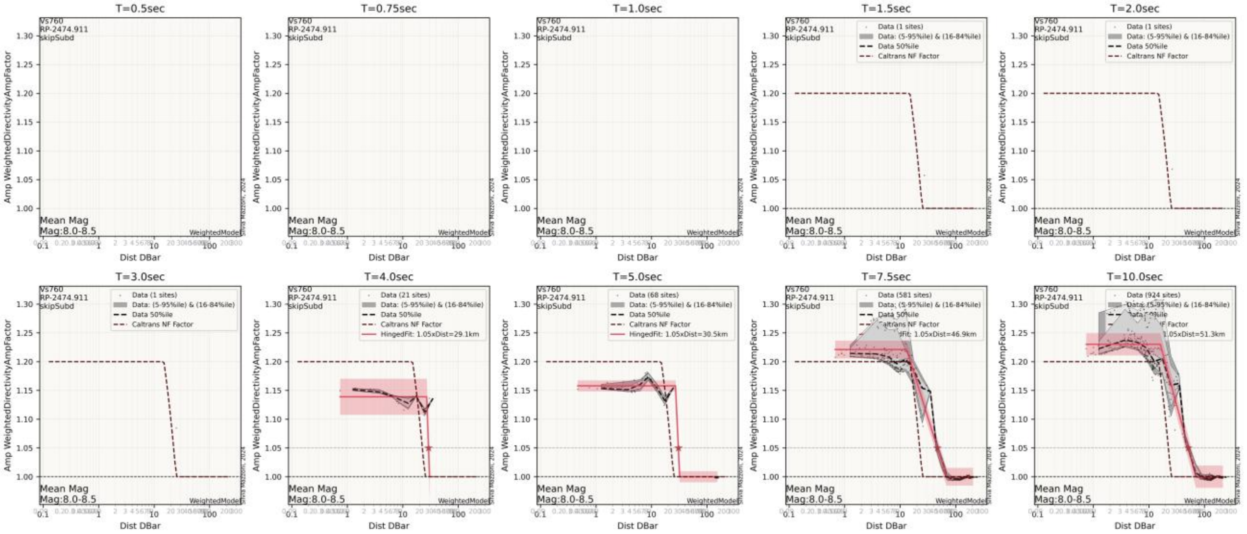

Figure 1-70 *Directivity-Amplification vs Mean Distance Models -- Mean-Magnitude Bin: 8.0-8.5*

1.11. DIRECTIVITY AMPLIFICATION VS PERIOD

The maximum directivity amplification factors from the distance-based models were extracted and plotted as functions of period. Both the estimated median values as well as the estimated median plus/minus one and two standard deviations (16th–84th, and 2nd-98th percentile ranges) for Vs30 = 760 m/s and a return period of 2475 years are shown in **Figure 1-71** and **Figure 1-72** for Modal and Mean deaggregation data bins, respectively. The data for the model median and one-standard deviation estimates from each of these figures was combined into a single plot for all magnitude beans, as shown in **Figure 1-73** and **Figure 1-74** for Modal and Mean deaggregation data bins, respectively. Please note that the range of the vertical axes are different for Modal and Mean deaggregation bins. It is worth noting that the data for Modal Magnitudes show a more-predictable pattern of behavior.

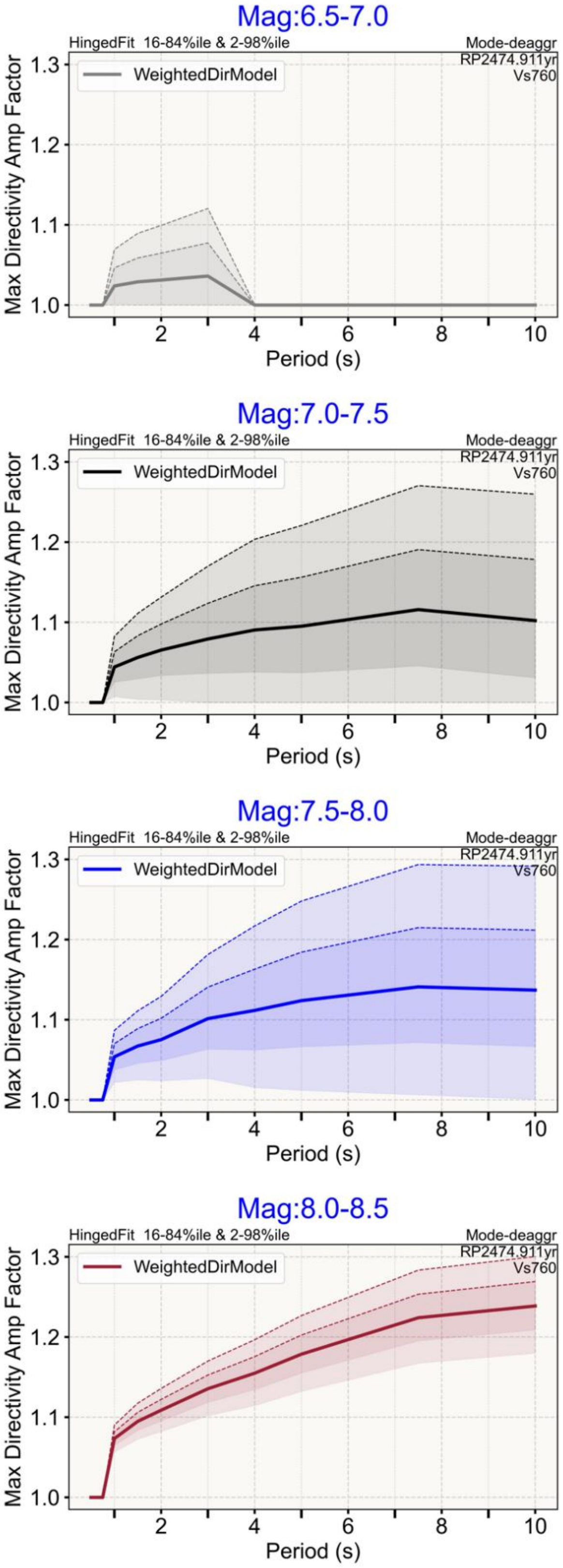

Figure 1-71 *Model Maximum Amplification Factor vs Period for each* ***Modal****-Magnitude bin.*

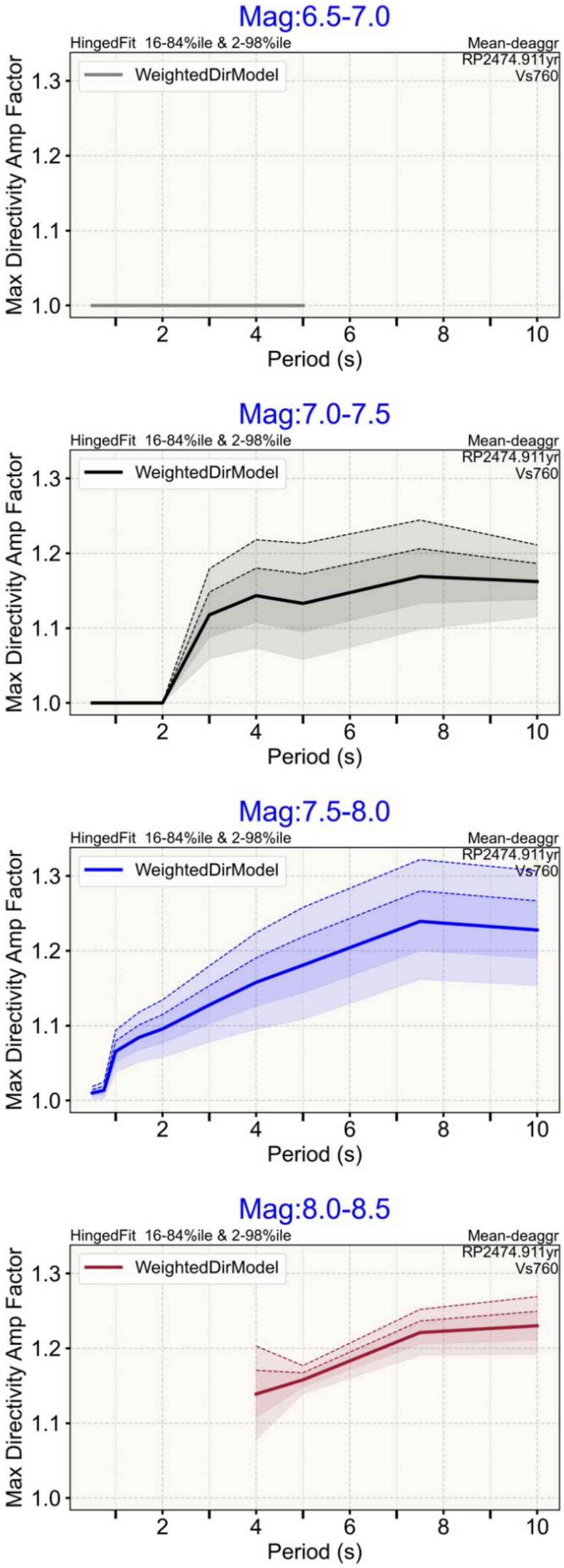

Figure 1-72 *Model Maximum Amplification Factor vs Period for each* ***Mean****-Magnitude bin.*

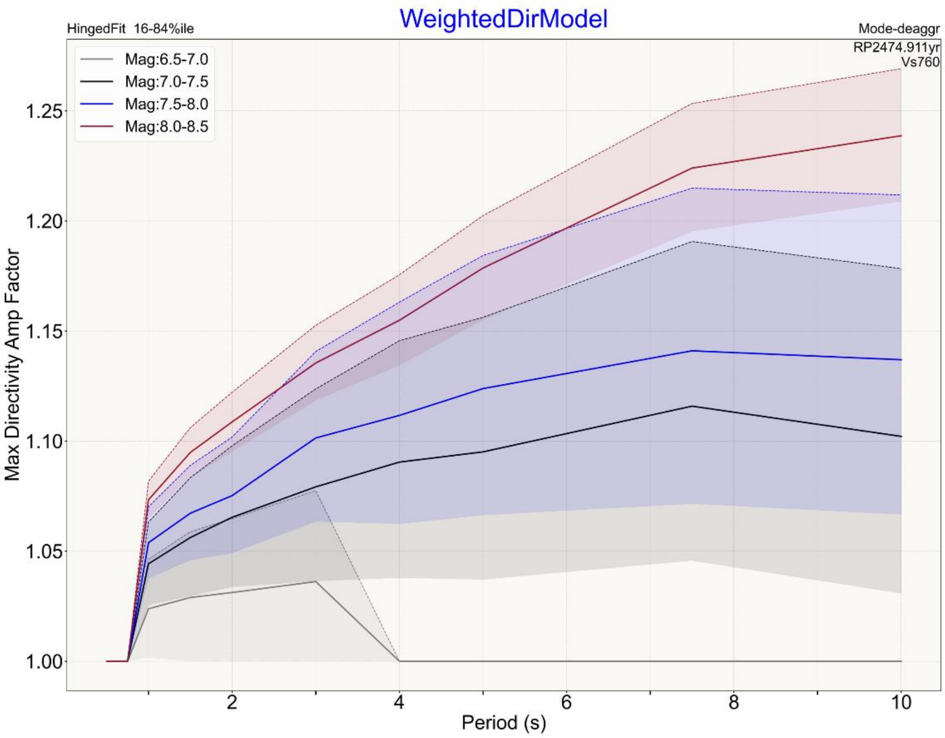

Figure 1-73 *Model Maximum Amplification Factor vs Period for all* ***Modal****-Magnitude bins -- Median +/- one standard deviation.*

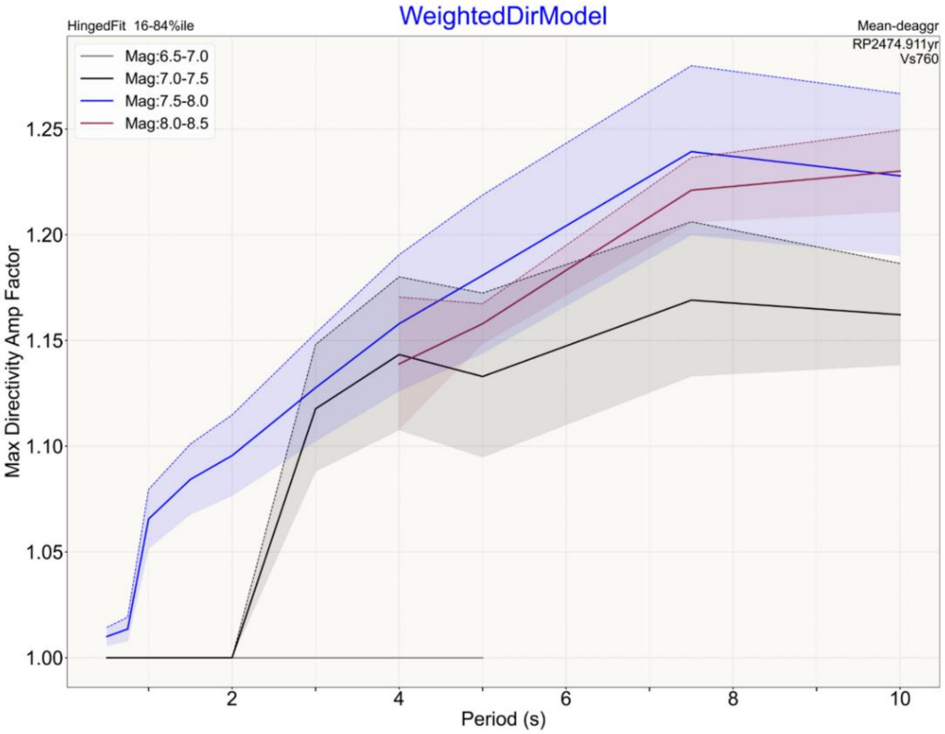

Figure 1-74 *Model Maximum Amplification Factor vs Period for all* ***Mean****-Magnitude bins -- Median +/- one standard deviation.*

1.12. DIRECTIVITY THRESHOLD DISTANCE: AMPLIFICATION-DISTANCE MODEL VS DATA

The Directivity-Amplification Threshold Distance has been defined as the shortest distance where the directivity amplification factor exceeded 1.05 earlier in this chapter, which we obtained from the data (Data Median, 16-84%ile, & 5-95%). We can now compare these data with the value predicted by the directivity-amplification vs distance model -- estimated as the distance at which the median prediction of amplitude intercepts and amplification of 1.05 (Amp-Dist Model Intercept). These data are shown in **Figure 1-75** and **Figure 1-76** for Modal and Mean Deaggregation magnitude bins, respectively. These data were used in evaluating whether the amplitude-distance model yielded unreasonable results. Both deaggregation types do not raise any red flags.

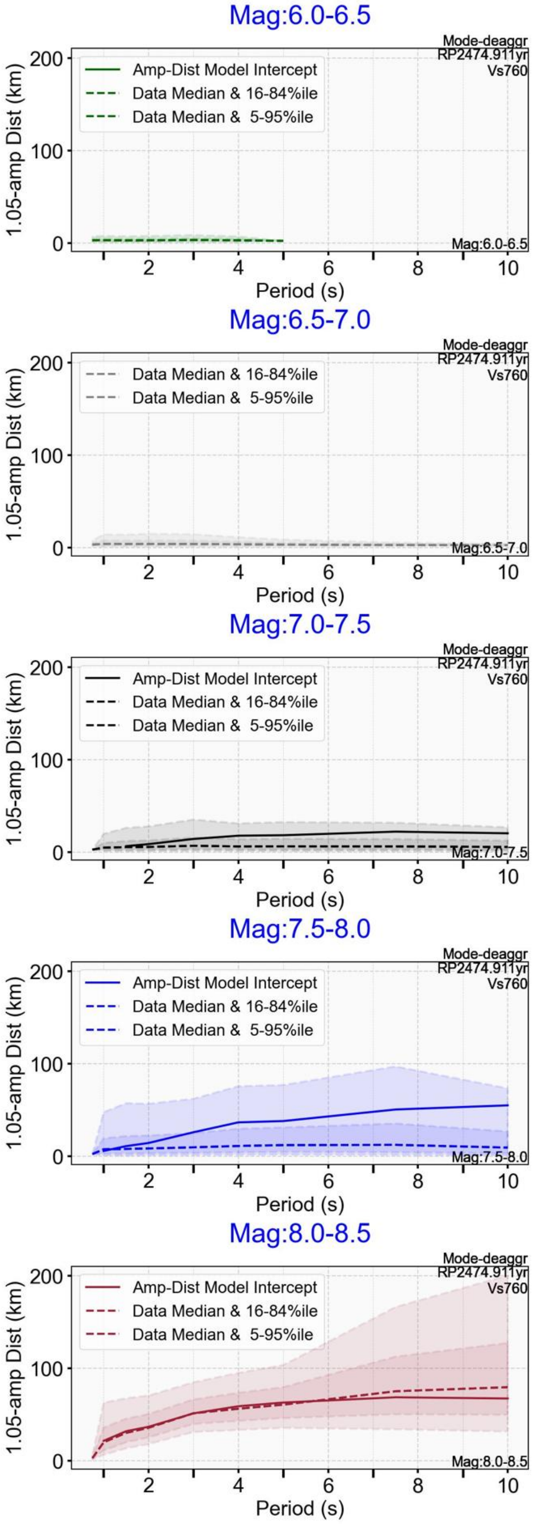

Figure 1-75 *Comparison of Threshold Distances (@1.05-amplification) Directivity Amplification-Distance Model Intercept (solid line) and Data-Interpolation Threshold Distance (Data Median, 16-84%, and 9-95% range) –* ***Modal****-Deaggregation Magnitude Bins*

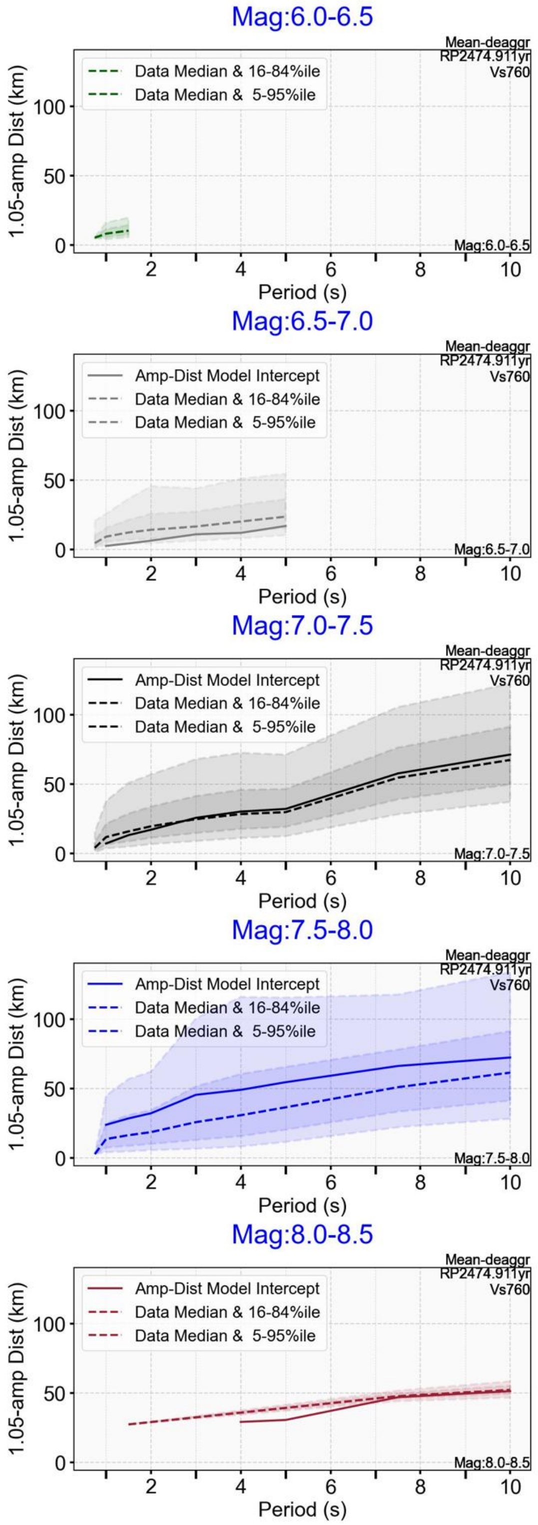

Figure 1-76 *Comparison of Threshold Distances (@1.05-amplification) Directivity Amplification-Distance Model Intercept (solid line) and Data-Interpolation Threshold Distance (Data Median, 16-84%, and 9-95% range) –* ***Mean****-Deaggregation Magnitude Bins*

1.13. SIMPLIFIED MODEL FOR DIRECTIVITY-AMPLIFICATION VS DISTANCE – BASED ON ELASTIC RESPONSE SPECTRA

The Directivity Amplification models developed in the previous section provide a practical simplification of more detailed site-specific models. However, for implementation within the Caltrans Seismic Design Criteria (SDC), an additional simplification is required: the removal of magnitude dependence. To ensure the model remains conservative and suitable for design applications, the resulting simplified model must envelop both the empirical data and the magnitude-dependent models previously developed. **Figure 1-77** shows the simplified model as a modification to the current Caltrans Directivity Amplification Factors – for period less than or equal to 3.0 seconds. Panels a. and b. display the model directivity-amplification factor vs distance and period, respectively. Panels c. and d. display the ratio of this amplification factor divided by the Caltrans SDC 2.0 amplification factor, vs distance and period, respectively. The values for a range of distances and oscillator periods are shown in **Table 1.2**. The change from the current SDC value is shown as the ratio of recommended to Caltrans in **Table 1.3**.

The recommendation extend the distance from 25 to 35km and shift the minimum period from 0.5 to 0.75 seconds as well as the maximum-amplification period from 1.0 to 2.0 seconds. It is important to note that this simplified model is recommended only for oscillator periods of 3 seconds or less. Additional consideration and studies need to be performed to extend the period range. However, the 3-second limit was considered acceptable for bridge-design applications where this simplified method would be used. Magnitude dependent, or site-specific studies should be used for longer-period structures.

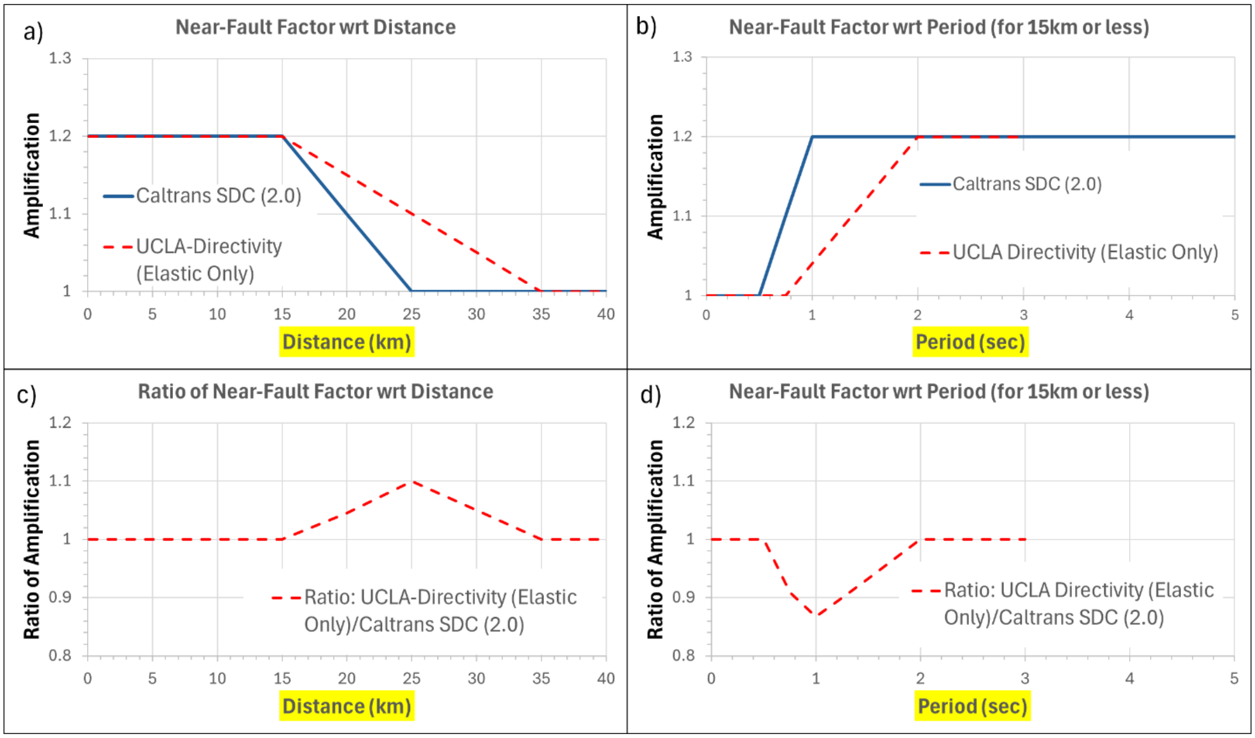

Figure 1-77 *Proposed Simplified Model considering Elastic Response Only – The proposed model applies to T<= 3.0 seconds. a. and b. amplification factor, vs Distance and Period, respectively. c. and d. amplification factor/Caltrans SDC 2.0 factor, vs Distance and Period, respectively*

__Table 1.2__ Recommended Directivity Amplification Factor Considering Elastic response only.

Amp Factor		Distance (km)												
		0.1	1	2.5	5	7.5	10	12.5	15	20	25	30	35	40
Period (sec)	0.01	1	1	1	1	1	1	1	1	1	1	1	1	1
	0.1	1	1	1	1	1	1	1	1	1	1	1	1	1
	0.2	1	1	1	1	1	1	1	1	1	1	1	1	1
	0.3	1	1	1	1	1	1	1	1	1	1	1	1	1
	0.4	1	1	1	1	1	1	1	1	1	1	1	1	1
	0.5	1	1	1	1	1	1	1	1	1	1	1	1	1
	0.75	1	1	1	1	1	1	1	1	1	1	1	1	1
	1	1.04	1.04	1.04	1.04	1.04	1.04	1.04	1.04	1.03	1.02	1.01	1	1
	1.25	1.08	1.08	1.08	1.08	1.08	1.08	1.08	1.08	1.06	1.04	1.02	1	1
	1.5	1.12	1.12	1.12	1.12	1.12	1.12	1.12	1.12	1.09	1.06	1.03	1	1
	1.75	1.16	1.16	1.16	1.16	1.16	1.16	1.16	1.16	1.12	1.08	1.04	1	1
	2	1.2	1.2	1.2	1.2	1.2	1.2	1.2	1.2	1.15	1.1	1.05	1	1
	2.5	1.2	1.2	1.2	1.2	1.2	1.2	1.2	1.2	1.15	1.1	1.05	1	1
	3	1.2	1.2	1.2	1.2	1.2	1.2	1.2	1.2	1.15	1.1	1.05	1	1
	5	NA	NA	NA	NA	NA	NA	NA	NA	NA	NA	NA	NA	NA

__Table 1.3__ Ratio of Recommended Directivity Amplification Factor Considering Elastic response to Caltrans SDC 2.0

Amp Factor Ratio		Distance (km)												
		0.1	1	2.5	5	7.5	10	12.5	15	20	25	30	35	40
Period (sec)	0.01	1	1	1	1	1	1	1	1	1	1	1	1	1
	0.1	1	1	1	1	1	1	1	1	1	1	1	1	1
	0.2	1	1	1	1	1	1	1	1	1	1	1	1	1
	0.3	1	1	1	1	1	1	1	1	1	1	1	1	1
	0.4	1	1	1	1	1	1	1	1	1	1	1	1	1
	0.5	1	1	1	1	1	1	1	1	1	1	1	1	1
	0.75	0.91	0.91	0.91	0.91	0.91	0.91	0.91	0.91	0.95	1	1	1	1
	1	0.87	0.87	0.87	0.87	0.87	0.87	0.87	0.87	0.94	1.02	1.01	1	1
	1.25	0.9	0.9	0.9	0.9	0.9	0.9	0.9	0.9	0.96	1.04	1.02	1	1
	1.5	0.93	0.93	0.93	0.93	0.93	0.93	0.93	0.93	0.99	1.06	1.03	1	1
	1.75	0.97	0.97	0.97	0.97	0.97	0.97	0.97	0.97	1.02	1.08	1.04	1	1
	2	1	1	1	1	1	1	1	1	1.05	1.1	1.05	1	1
	2.5	1	1	1	1	1	1	1	1	1.05	1.1	1.05	1	1
	3	1	1	1	1	1	1	1	1	1.05	1.1	1.05	1	1
	5	NA	NA	NA	NA	NA	NA	NA	NA	NA	NA	NA	NA	NA

1.14. SIMPLIFIED DIRECTIVITY-AMPLIFICATION VS DISTANCE MODEL – ACCOUNTING FOR INELASTIC RESPONSE SPECTRA

The goal of this step is to convert the effect of directivity on elastic response to the effect of directivity on inelastic response with ductility of 3. The ductility of 3 is used as a representative value. Ductility demands for code-designed structures generally range between 1 (for elastic response) and 6 (for ductile systems). Values lower than 2.5 are not expected for designs specially for locations in California. The decision between higher ductilities is not critical, because the yield strength drops significantly when moderate levels of ductility are allowed. But after that, the effect is not as large. **Figure 1-4** shows the effect of ductility on median Cy prediction for damping of 5%, Bilinear Takeda hysteretic model, and Vs30 of 760 m/s. You see that there is a greater change when we go from 1-3 than 3-5.

Treating the effect of directivity as the difference between observed response and median prediction of GMMs, this goal is achieved by developing models between inelastic response and elastic response residuals. The Inelastic-Response Spectra Study produced a set of period- and ductility-dependent adjustment factors to convert effect of directivity on elastic response spectra into the effect of directivity on inelastic response spectra.

The conversion relies on two complementary models. The **first model** was developed from the full dataset of elastic and inelastic response spectra, including records with and without directivity. Because it is trained on the broad dataset, it provides a general relationship between elastic and inelastic residuals. However, when applied specifically to the 137 pulse-like ground motions in the NGA-West2 database, this general model does not fully capture the unique effects that pulse characteristics impose on inelastic response. To address this limitation, the **second model** was developed using only the 137 pulse-like records. This targeted model accounts for the additional inelastic amplification caused by pulses, which the general model misses. Using both models together allows us to quantify directivity amplification factors for inelastic response with greater accuracy.

These amplification factors were plotted as a function of distance for each oscillator period, assuming Vs_{30} = 760 m/s and a return period of 2,475 years, as shown in Figure 1-78. In this figure, it can be observed that directivity amplification of inelastic response spectra exceeds the 5% threshold at an oscillator period of 0.75 seconds—a behavior that was not observed for the elastic response spectra shown previously in Figure 1-47.

The amplification observed at shorter periods for inelastic response spectra is consistent with the concept of period elongation in yielding structures. Accordingly, the proposed directivity amplification model was modified to account for this period-dependent behavior by shifting the minimum period at which amplification is considered from 0.75 seconds to 0.5 seconds. This adjustment aligns the model with the Caltrans SDC, which also uses a 0.5-second threshold. A comparison of the directivity amplification models for inelastic and elastic responses is shown in **Figure 1-78**.

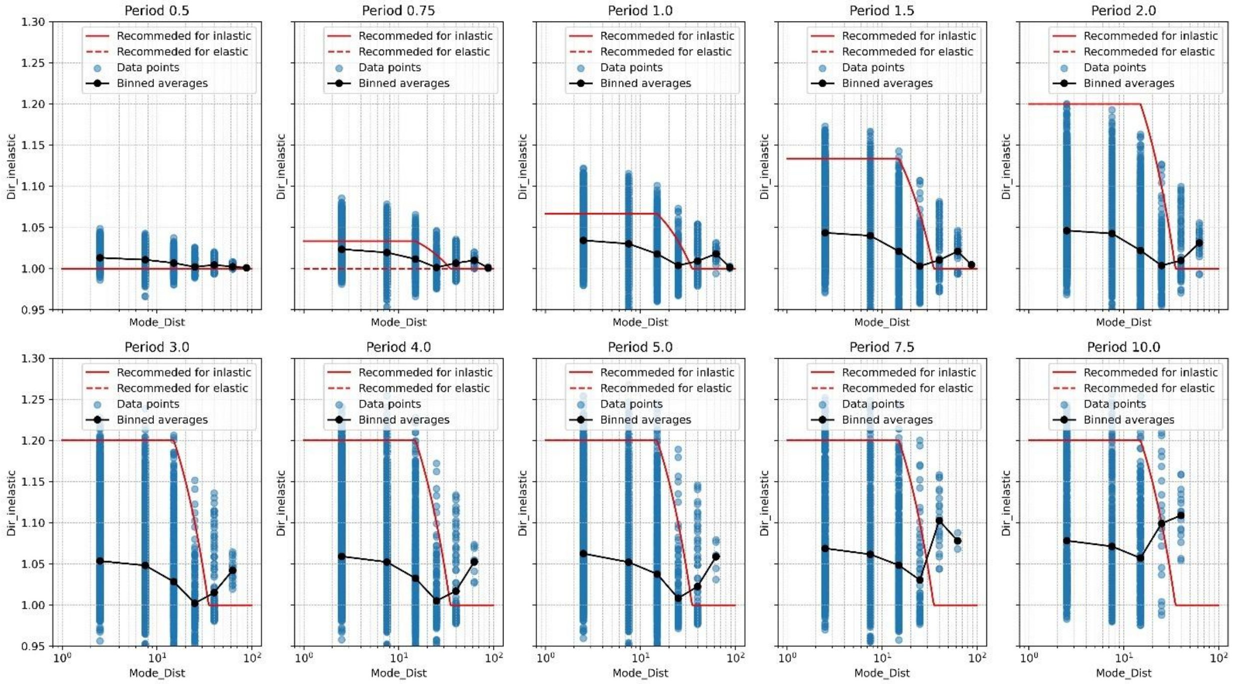

***Figure 1-78** Directivity Amplification Factor for Inelastic Response Spectra (Vs30=760m/s, RP=2475yr)*

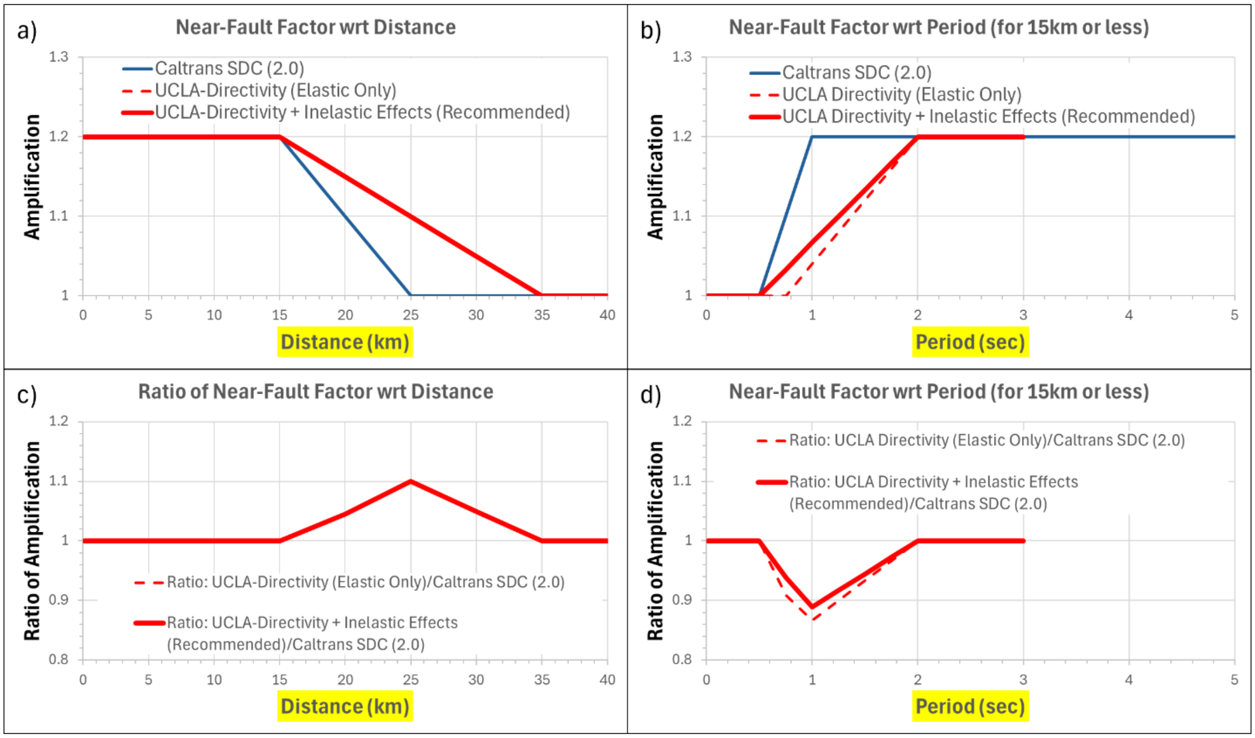

Figure 1-79 *Directivity Amplification Factors considered in Study: Comparison of model which considers only elastic response and model which also considers inelastic response with Caltrans SDC 2.0.*

1.14.1. Comparison of Recommended Model to Data and Models

The recommended model was compared to the data, the period and magnitude-bin dependent model, as well as the current Caltrans NF factor for each individual magnitude bin and period, as shown in **Figure 1-80** through **Figure 1-84** for the Modal data, and **Figure 1-85** through **Figure 1-89** for the Mean Data.

1.14.1.1. Mode

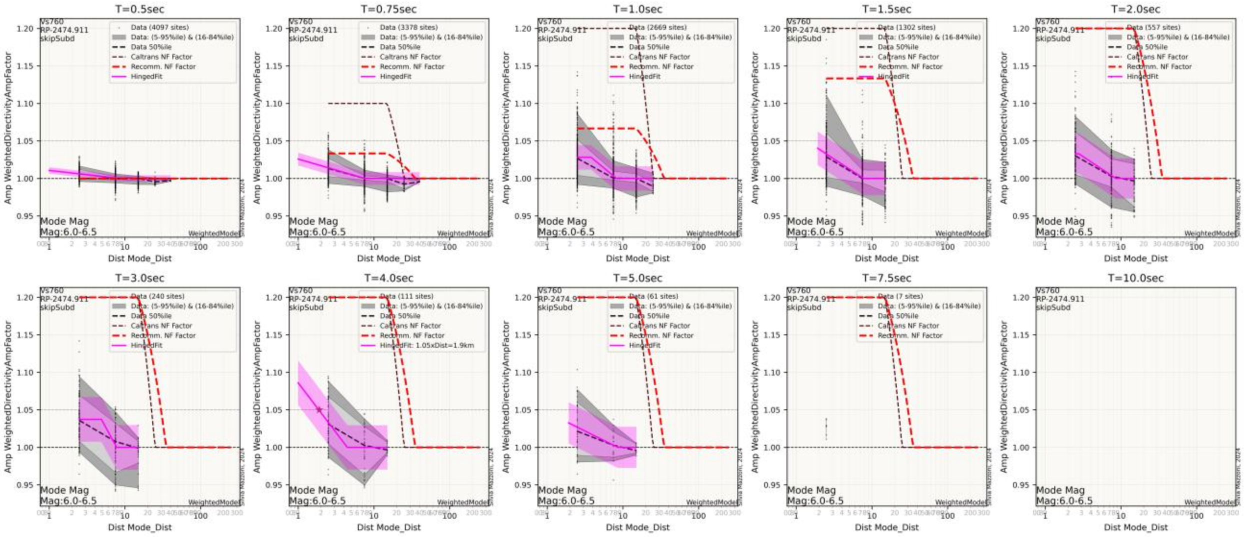

Figure 1-80 *Comparison of recommended model with data, period and magnitude-bin model, and Caltrans model. Modal-Magnitude Bin 6.0-6.5*

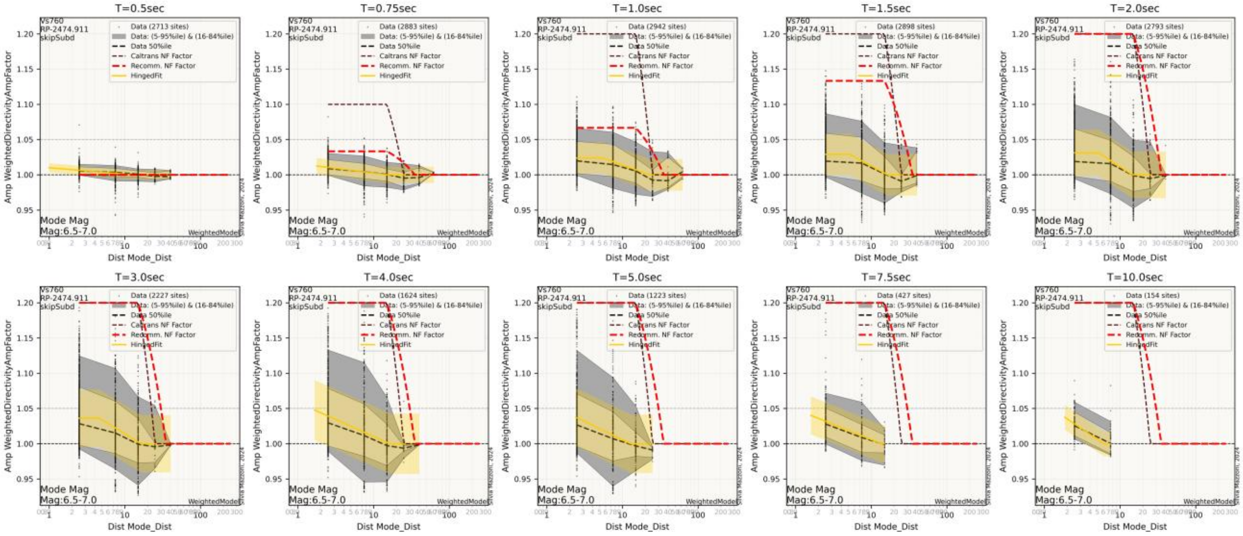

Figure 1-81 *Comparison of recommended model with data, period and magnitude-bin model, and Caltrans model. Modal-Magnitude Bin 6.5-7.0*

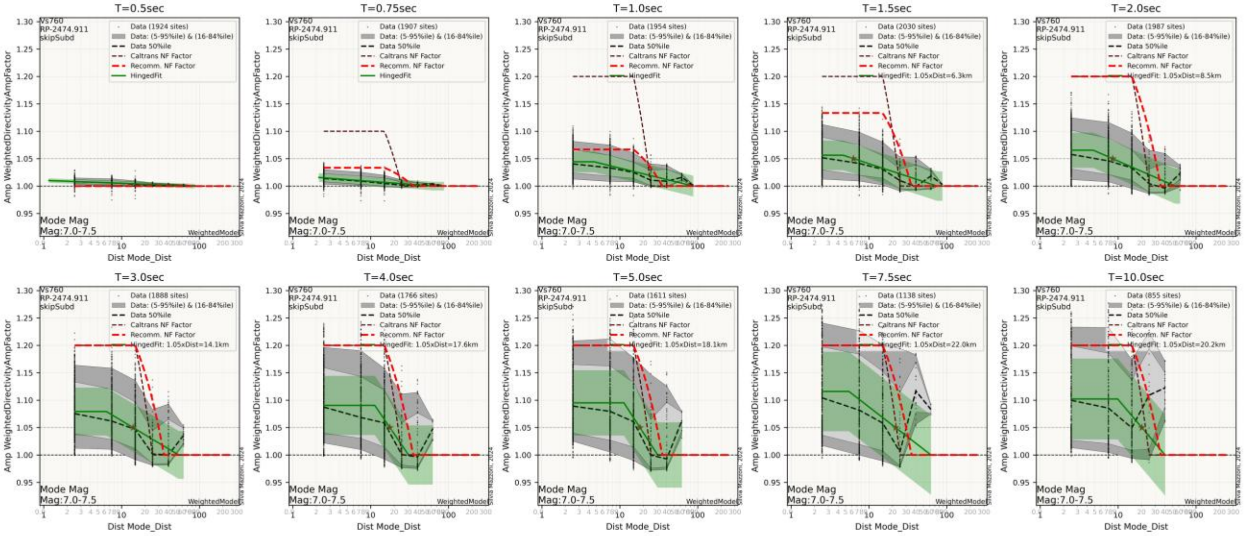

Figure 1-82 *Comparison of recommended model with data, period and magnitude-bin model, and Caltrans model. Modal-Magnitude Bin 7.0-7.5*

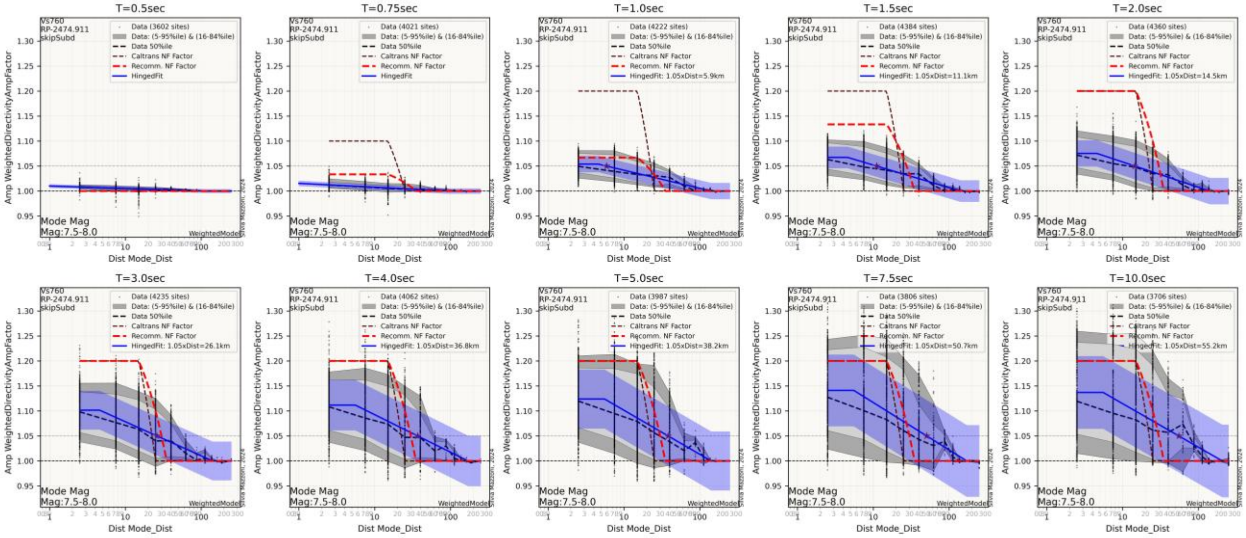

Figure 1-83 Comparison of recommended model with data, period and magnitude-bin model, and Caltrans model. Modal-Magnitude Bin 7.5-8.0

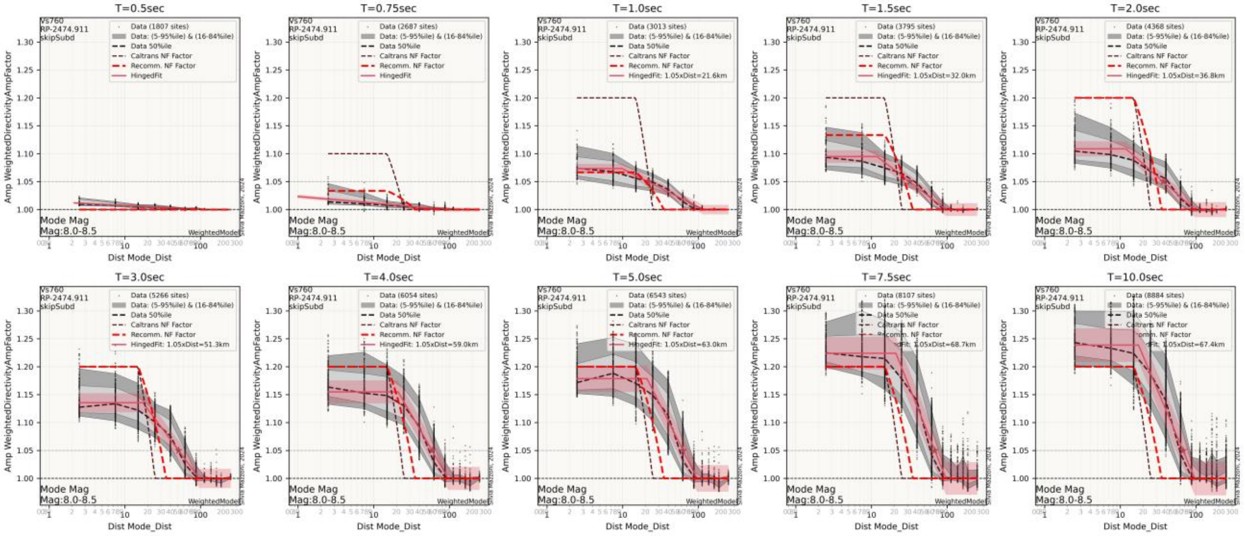

Figure 1-84 Comparison of recommended model with data, period and magnitude-bin model, and Caltrans model. Modal-Magnitude Bin 8.0-8.5

1.14.1.2. Mean

The recommended model was applied to the Mean deaggregation data and compared to the data and other models mentioned above, as shown in **Figure 1-85** through **Figure 1-89**, for each Mean-Magnitude bin.

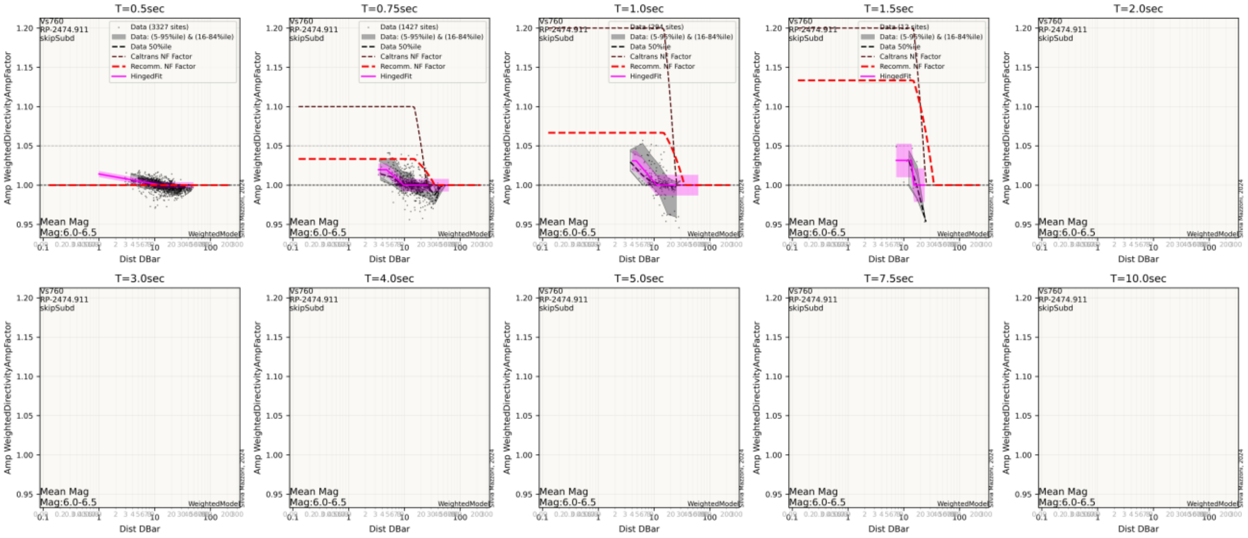

Figure 1-85 *Comparison of recommended model with data, period and magnitude-bin model, and Caltrans model. Mean-Magnitude Bin 6.0-6.5*

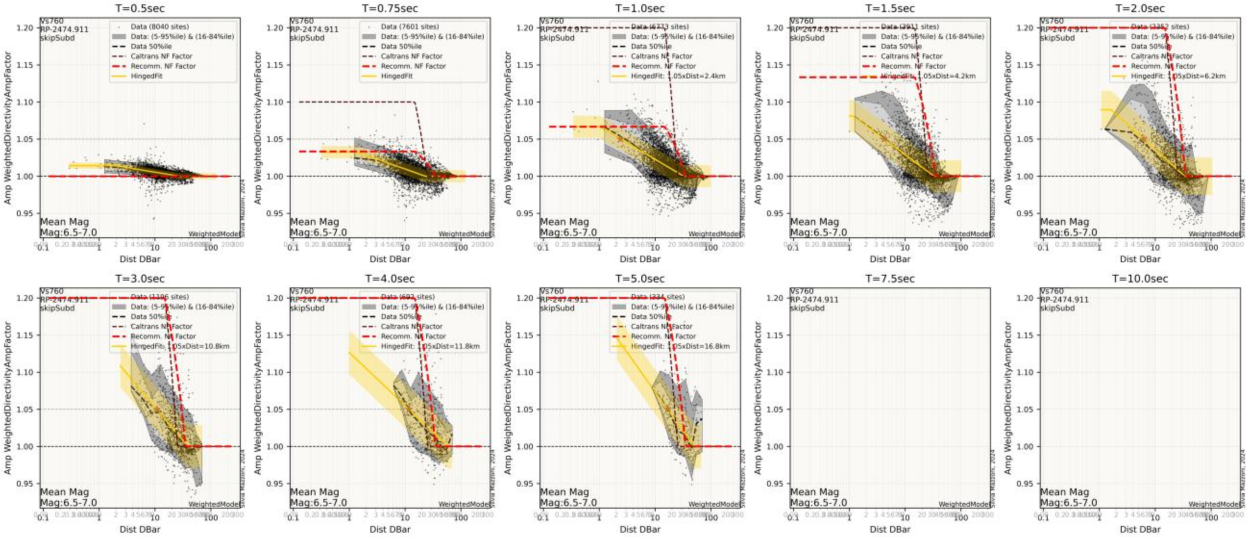

Figure 1-86 *Comparison of recommended model with data, period and magnitude-bin model, and Caltrans model. Mean-Magnitude Bin 6.5-7.0*

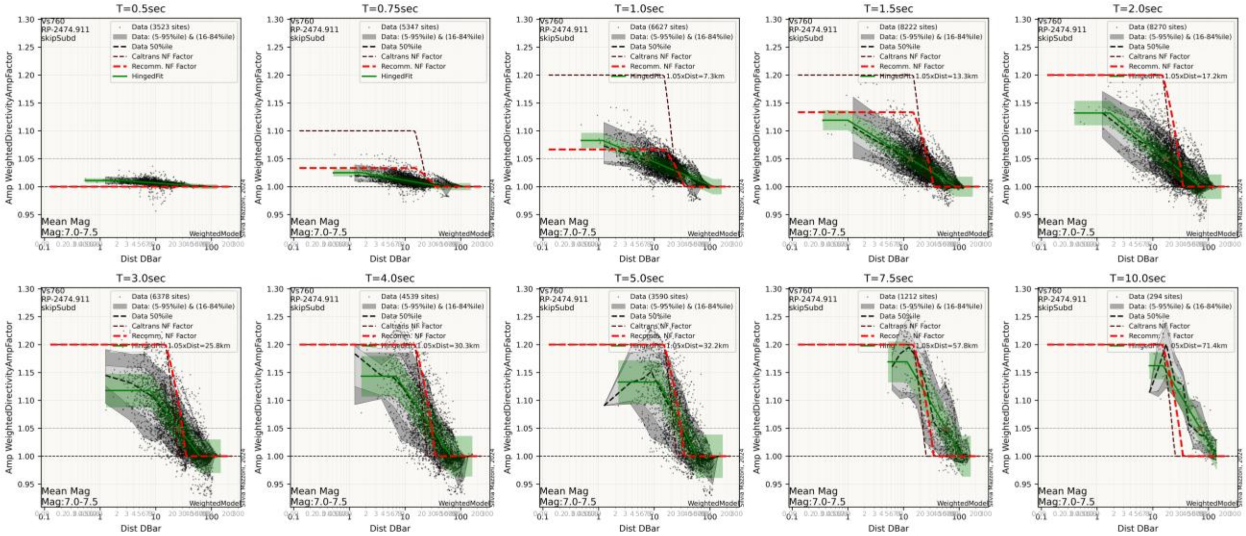

Figure 1-87 Comparison of recommended model with data, period and magnitude-bin model, and Caltrans model. Mean-Magnitude Bin 7.0-7.5

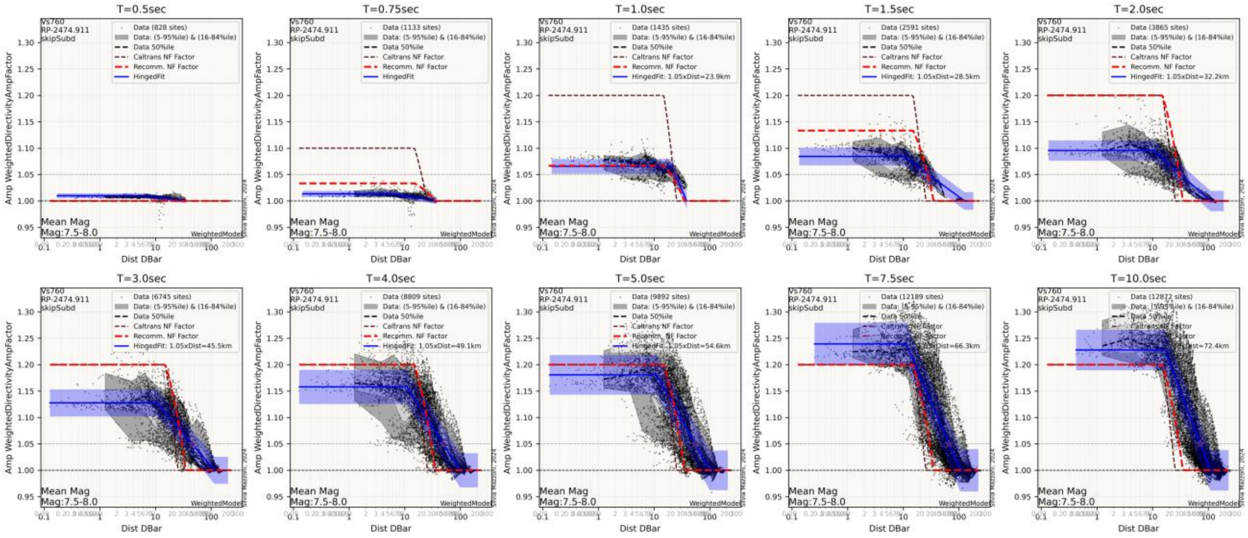

***Figure 1-88** Comparison of recommended model with data, period and magnitude-bin model, and Caltrans model. Mean-Magnitude Bin 7.5-8.0*

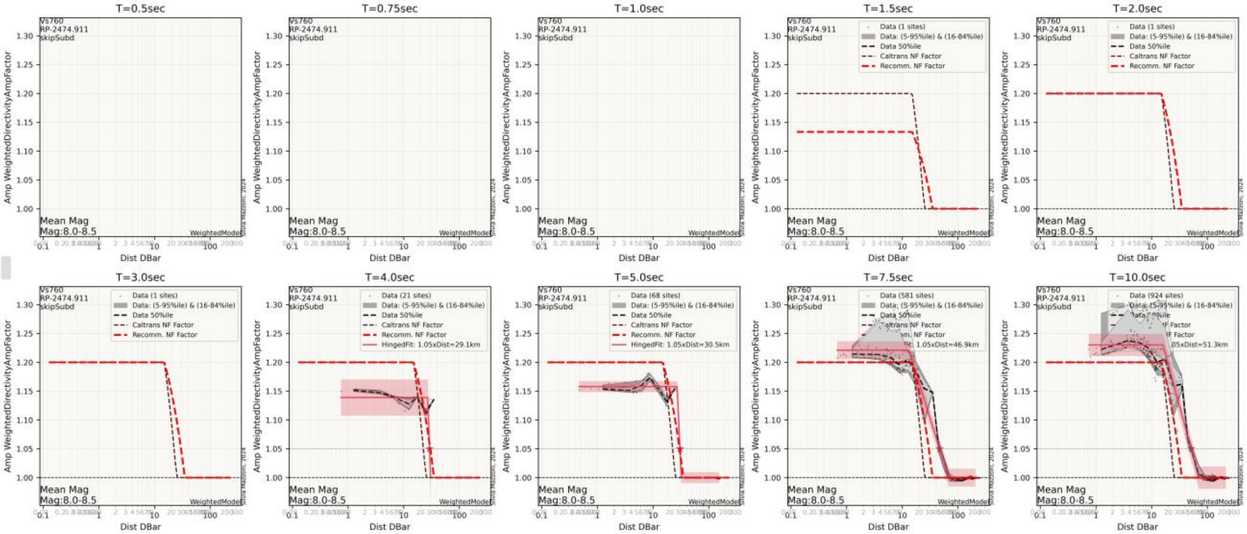

Figure 1-89 *Comparison of recommended model with data, period and magnitude-bin model, and Caltrans model. Mean-Magnitude Bin 8.0-8.5*

1.15. SUMMARY & CONCLUSIONS

Through this study, we leveraged the data and findings from recent UCLA research on both elastic and inelastic response spectra in the near-fault regions to develop recommendations for updating Caltrans near-fault adjustment factors. Multiple models and tools have been developed in this project:

1. **Updated Near-Fault Adjustment Factors:**
   We have enhanced the simplified directivity amplification model currently used by Caltrans engineers during preliminary bridge design. The updated model depends only on distance to the fault and oscillator period, making it easy to apply without requiring extensive site-specific data. The new model includes the near-fault directivity effects on both elastic and inelastic response spectra. The new model is illustrated in panels a. (vs distance) and b. (vs period) of **Figure 1-90**. Numerical values are provided in **Table 1.4**. To help users transition from previous Caltrans design criteria, panel c. (vs distance) and d. (vs period) of **Figure 1-90** and **Table 1.5** provide the ratios between the proposed amplification factors and those specified in SDC 2.0.
2. **Magnitude-Dependent Model:**
   For applications requiring greater accuracy, we developed an additional model that introduces magnitude dependence into the directivity amplification factors. This model remains relatively simple to use while offering improved precision and a wider range of applicability, particularly for large-magnitude earthquake scenarios.
3. **Site-Specific Tool:**
   For cases where a fully site-specific assessment is desired, engineers can access an interactive online tool developed as part of the UCLA NHR3 project. This resource allows users to generate directivity-adjusted response elastic response spectra based on site-specific parameters including location, magnitude, and distance from faults. The tool is publicly available at:
   https://www.risksciences.ucla.edu/nhr3/california-directivity

It is important to note that the primary objective of this study was to develop recommendations for simplified modifications to the current Caltrans SDC 2.0 criteria for computing Near-Fault Adjustment Factors. The figures included in this report provide the main basis for developing these factors. Unless otherwise indicated, the figures correspond to a 2,475-year return period and use the Weighted-Directivity Model described in Section 1.4 of this report. For completeness, additional data plots were generated for the 1,000-year return period as well as for the individual Directivity Models. These supplemental plots are not included here but are be provided in the project web page: https://www.risksciences.ucla.edu/caltrans-directivity-hazard.

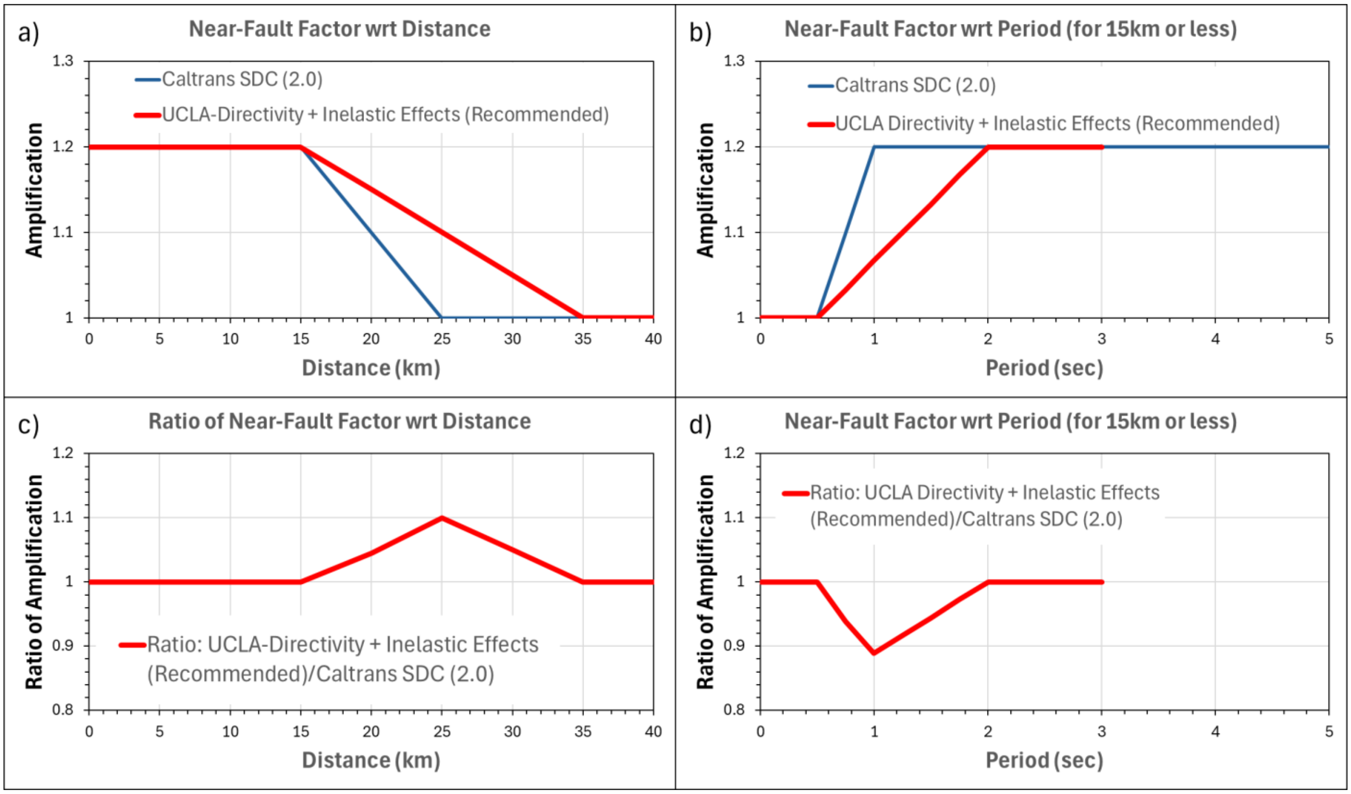

Figure 1-90 *Recommended Directivity-Amplification Factors & Caltrans SDC 2.0 Factors*

Table 1.4 *Recommended Directivity Amplification Factors Accounting for Inelastic Response*

Amp Factor		**Distance (km)**												
		0.1	1	2.5	5	7.5	10	12.5	15	20	25	30	35	40
Period (sec)	0.01	1	1	1	1	1	1	1	1	1	1	1	1	1
	0.1	1	1	1	1	1	1	1	1	1	1	1	1	1
	0.2	1	1	1	1	1	1	1	1	1	1	1	1	1
	0.3	1	1	1	1	1	1	1	1	1	1	1	1	1
	0.4	1	1	1	1	1	1	1	1	1	1	1	1	1
	0.5	1	1	1	1	1	1	1	1	1	1	1	1	1
	0.75	1.033	1.033	1.033	1.033	1.033	1.033	1.033	1.033	1.025	1.017	1.008	1	1
	1	1.067	1.067	1.067	1.067	1.067	1.067	1.067	1.067	1.05	1.033	1.017	1	1
	1.25	1.1	1.1	1.1	1.1	1.1	1.1	1.1	1.1	1.075	1.05	1.025	1	1
	1.5	1.133	1.133	1.133	1.133	1.133	1.133	1.133	1.133	1.1	1.067	1.033	1	1
	1.75	1.167	1.167	1.167	1.167	1.167	1.167	1.167	1.167	1.125	1.083	1.042	1	1
	2	1.2	1.2	1.2	1.2	1.2	1.2	1.2	1.2	1.15	1.1	1.05	1	1
	2.5	1.2	1.2	1.2	1.2	1.2	1.2	1.2	1.2	1.15	1.1	1.05	1	1
	3	1.2	1.2	1.2	1.2	1.2	1.2	1.2	1.2	1.15	1.1	1.05	1	1
	5	NA	NA	NA	NA	NA	NA	NA	NA	NA	NA	NA	NA	NA

***Table 1.5** Ratio of Recommended Directivity Amplification Factors accounting for Inelastic Response to SDC 2.0*

Amp Factor Ratio		**Distance (km)**												
		0.1	1	2.5	5	7.5	10	12.5	15	20	25	30	35	40
Period (sec)	0.01	1	1	1	1	1	1	1	1	1	1	1	1	1
	0.1	1	1	1	1	1	1	1	1	1	1	1	1	1
	0.2	1	1	1	1	1	1	1	1	1	1	1	1	1
	0.3	1	1	1	1	1	1	1	1	1	1	1	1	1
	0.4	1	1	1	1	1	1	1	1	1	1	1	1	1
	0.5	1	1	1	1	1	1	1	1	1	1	1	1	1
	0.75	0.94	0.94	0.94	0.94	0.94	0.94	0.94	0.94	0.98	1.02	1.01	1	1
	1	0.89	0.89	0.89	0.89	0.89	0.89	0.89	0.89	0.95	1.03	1.02	1	1
	1.25	0.92	0.92	0.92	0.92	0.92	0.92	0.92	0.92	0.98	1.05	1.03	1	1
	1.5	0.94	0.94	0.94	0.94	0.94	0.94	0.94	0.94	1	1.07	1.03	1	1
	1.75	0.97	0.97	0.97	0.97	0.97	0.97	0.97	0.97	1.02	1.08	1.04	1	1
	2	1	1	1	1	1	1	1	1	1.05	1.1	1.05	1	1
	2.5	1	1	1	1	1	1	1	1	1.05	1.1	1.05	1	1
	3	1	1	1	1	1	1	1	1	1.05	1.1	1.05	1	1
	5	NA	NA	NA	NA	NA	NA	NA	NA	NA	NA	NA	NA	NA

1.16. REFERENCES

Al Atik, L., Gregor, N., Mazzoni, S. and Bozorgnia, Y. GIRS 2022-12: "Directivity-Based Probabilistic Seismic Hazard Analysis for the State of California: Report 1, No-Directivity Baseline Case" DOI:10.34948/N3KS3B

Al Atik, L., Gregor, N., Bozorgnia, Y., and Mazzoni, S. GIRS 2023-05: Directivity-Based Probabilistic Seismic Hazard Analysis for the State of California: Report 2, Directivity Implementation DOI: 10.34948/N32010

Bayless, J.R. and Somerville, P.G. (2013). Final report of the NGA-West2 directivity working group. Chapter 2, PEER Report No. 2013/09.

Bayless, J.R., Somerville, P.G., and Skarlatoudis, A. (2020). A rupture directivity adjustment model applicable to the NGA-West2 ground motion models and complex fault geometries. Final Technical Report: USGS Award G18AP00092

Chiou B.S.-J., Spudich P. (2013). Final report of the NGA-West2 directivity working group. Chapter 6, PEER Report No. 2013/09.

Mazzoni, S., Al Atik, L., Gregor, N., Bozorgnia, Y. (2023): Directivity-Based Intensity-Measure Interactive Maps. The B. John Garrick Institute for the Risk Sciences. Dataset. https://doi.org/10.34948/N3101P (https://doi.org/10.34948/N3101P)

Mazzoni, S., Al Atik, L., Gregor, N., Bozorgnia, Y. (2023): Directivity-Based PSHA Interactive Tool. The B. John Garrick Institute for the Risk Sciences. Dataset. https://doi.org/10.34948/N34S39 (https://doi.org/10.34948/N34S39)

Mazzoni, S., Al Atik, L., Gregor, N., Bozorgnia, Y. (2023): Directivity-Based Probabilistic Seismic Hazard in California: Data Tables: https://www.risksciences.ucla.edu/nhr3/california-directivity-hazard-data (Accessed 5/17/2025)

California Department of Transportation (2019): Seismic Design Criteria, 2.0.

Bahrampouri, M., Bozorgnia, Y., Campbell, K., and Mazzoni, S. (2024), “Ground motion models for inelastic response spectra using NGA-West2 database.” *Earthquake Spectra*, 1-20. DOI: 10.1177/87552930241249704

2. EFFECTS OF NEAR-FAULT DIRECTIVITY AND GROUND MOTION DIRECTIONALITY ON SEISMIC RESPONSES OF BRIDGES

by Esra Zengin and Yousef Bozorgnia

2.1. EXECUTIVE SUMMARY

This chapter evaluates the impacts of the recently proposed near-fault directivity factors for the Caltrans Seismic Design Criteria (SDC) on the seismic performance of two Caltrans ordinary long-span bridge configurations: one with a single-column bent and the other with a two-column bent. Using nonlinear time history analysis (NTHA), three-dimensional (3D) bridge models were evaluated under 20 bidirectional near-fault ground motions, scaled to three different target spectra: 1) Uniform Hazard Spectrum (UHS) without directivity, 2) UHS with directivity amplification factors based on a weighted average of directivity models (wDir), and 3) UHS with proposed (modified) SDC directivity factors (wDir-SDC$_{mod}$). Analyses were conducted for return periods (T_R) of 1000 and 2475 years in two sites: Los Angeles and Oakland. Both bridge configurations feature zero skew angles and seat-type abutments and explicitly incorporate soil-structure interaction effects in their 3D numerical modeling. However, it is important to note that bridge designs do not reflect site-specific seismicity considerations. The ground motions were rotated to different incidence angles to examine the influence of ground-motion directionality on the transverse and longitudinal responses, specifically column drift ratio (CDR), displacement ductility demand (μ_D), and residual drift ratio (RDR), of the bridges. Finally, the results obtained from different methodologies, including elastic and inelastic analyses of single-degree-of-freedom (SDOF) systems, and NTHA were compared.

The findings demonstrated that in seismic design and analysis of bridges, it is important to include the near-fault directivity factors, as well as the directionality of ground motions. Such effects result in an increased structural demand. Specifically, pulse-like ground motions (wDir and wDir-SDC$_{mod}$ cases) resulted in higher CDR and μ_D compared to nonpulse motions. It was observed that the CDRs at specific incidence angles deviated by 15-35% from their corresponding median values (CDR$_{RotD50}$), with maximum responses typically occurring between 0°-45° for the transverse direction and at 90° for the longitudinal direction. Seismic demands were higher for bridges located in Oakland, a site with higher seismicity than Los Angeles. In Oakland, μ_D values for the two-column bent bridge exceeded Caltrans' design target displacement ductility demand of 5, indicating insufficient capacity to withstand extreme pulse motions. These findings emphasized the critical need for site-specific seismic design strategies in high-seismicity sites. Unlike CDRs, RDRs did not exhibit a clear trend with respect to incidence angle, and their variability was more

pronounced. While mean RDRs often remained within acceptable serviceability limits (e.g., < 1%), 84th percentile values exceeded thresholds, highlighting potential concerns for post-earthquake functionality.

This study also evaluated the effectiveness of a simplified inelastic SDOF model in comparison to the NTHA results. While inelastic SDOF models yielded comparable or slightly conservative CDRs at lower hazard levels (T_R=1000 years), they underestimated demands at T_R =2475 years. Inelastic SDOF models underpredicted RDRs due to limitations in representing hysteretic and multi-directional behavior of the 3D bridge models. Comparing the results from elastic and inelastic SDOF analyses, the equal displacement rule, a common assumption in seismic design, was shown to be unconservative for periods shorter than 1.5 seconds.

In summary, this study highlights the importance of incorporating near-fault directivity and ground motion directionality into seismic bridge design. Our recommendations are: For bridges in high-seismicity regions, target spectra with directivity amplification factors should be adopted, ground motion directionality effects should be considered, and generally we should move beyond a simplified SDOF elastic analysis considering the equal displacement rule. Implementing these measures can improve the resilience of bridges subjected to pulse motions.

2.2. INTRODUCTION

The seismic response of bridges is influenced by the characteristics of the ground motions, including the effects of near-fault forward directivity and the directionality or polarization of seismic waves. Directivity motions differ significantly from far-field motions, exhibiting distinctive features such as short-duration velocity pulses with high-intensity energy bursts (Somerville et al., 1997; Zengin and Abrahamson, 2020). Analytical and experimental investigations have demonstrated that directivity pulses can significantly increase displacement demands and residual drifts in bridge components, potentially exacerbating damage beyond what is predicted by far-field ground motions (Phan et al., 2007; Choi et al., 2010; Sengupta et. al., 2016; Zhong et al., 2020; Zengin et al., 2025a). While directivity is a defining characteristic of near-fault ground motions, directionality, which is defined as the sensitivity of structural response to the angle of incidence of seismic waves, may also be crucial for evaluating seismic demands on bridges. Past studies demonstrated that the incidence angle of ground motion affected the seismic response by intensifying demands on various bridge components (Torbol and Shinozuka, 2012; Wei et al., 2021). This direction-dependent behavior can become more pronounced for skewed bridges under bidirectional loading (Kaviani et al., 2012; Wang et al., 2020).

Caltrans SDC (SDC, 2019) includes a near-fault spectrum adjustment factor to account for amplified shaking at near-fault sites. Ground shaking is represented by a Design Spectrum (DS) based on a 975-year return period (i.e., 7% exceedance in 75 years), representing the Safety Evaluation Earthquake (SEE). The DS uses the latest USGS hazard maps based on RotD50 component, the median spectral accelerations over all orientations. The adjustment factor increases spectral ordinates by up to 20% for structures within 15 km of a fault, tapering linearly to zero at 25 km. For sites within 15 km, amplification applies to spectral periods above 0.5 s, reaching 1.20 at 1.0 s and remaining constant thereafter. While this partially addresses near-fault directivity, it does not capture directionality, pulse features in the time domain, or bidirectional loading effects, which can be important for the accurate seismic response of bridges in near-fault regions.

NTHA is typically applied to important or nonstandard bridges; however, ordinary bridges located near active faults can also experience severe seismic demands due to directivity and directionality effects. Simplified design procedures may underestimate critical responses such as peak displacements and residual drifts and often fail to capture complex behaviors related to directionality. This highlights the need for advanced modeling approaches and focused research efforts to better align design practices with the complex seismic behavior observed in near fault environments.

2.3. SITE-SPECIFIC PROBABILISTIC SEISMIC HAZARD ANALYSIS WITH OR WITHOUT DIRECTIVITY EFFECTS

To assess the impact of varying seismicity levels on seismic responses, the bridges used in this study were assumed to be at high-seismicity sites, namely Oakland (37.805°N, 122.27°W), and a relatively lower seismicity site, Los Angeles (34.054°N, 118.243°W). For each site, the site-specific probabilistic seismic hazard analysis (PSHA) was used to develop three target spectra for ground motion selection and scaling at T_R= 1000 and 2475 years. The site's shear-wave velocity at the top 30 m (Vs_{30}) was assumed to be 400 m/s. This is approximately the "center" of Vs_{30} values in NGA-West2 database (Ancheta et al., 2014). The considered response spectra are as follows:

1. UHS without directivity (woDir),
2. UHS with directivity (wDir), incorporating amplification factors from the weighted average of three directivity models, namely Chiou and Spudich (2013) weighed 0.50, Bayless and Somerville (2013) weighed 0.25, and Bayless et al. (2020) weighed 0.25 Please see details in Chapter 1 of this report.
3. UHS with directivity using modified Caltrans SDC near-fault adjustments, i.e., wDir (SDC_{mod}). Please see details in Chapter 1 of this report.

Figure 2.1(a) illustrates the target spectrum for each site, in which the ground motions were selected and scaled to be "compatible" with the median target spectrum within a period range of 0.8 to 4.0 seconds as the first three modes of the bridges fell between 1.2 and 1.9 seconds, as discussed in the subsequent section. Figure 2.1(b) illustrates the near-fault amplification factors from the UCLA weighted average of the directivity models (https://www.risksciences.ucla.edu/nhr3/california-directivity) and the proposed (modified) Caltrans SDC near-fault adjustments. These adjustment factors were applied to UHS-woDir to obtain the UHS-wDir. As seen in Figure 2.1(b), the wDir adjustment factors show site-dependency, where Oakland tends to have higher factors compared to Los Angeles, while wDir (SDC_{mod}) adjustments are constant and show a 5 to 10% increase between periods 1.5 to 2.0 seconds as compared to site-specific directivity models.

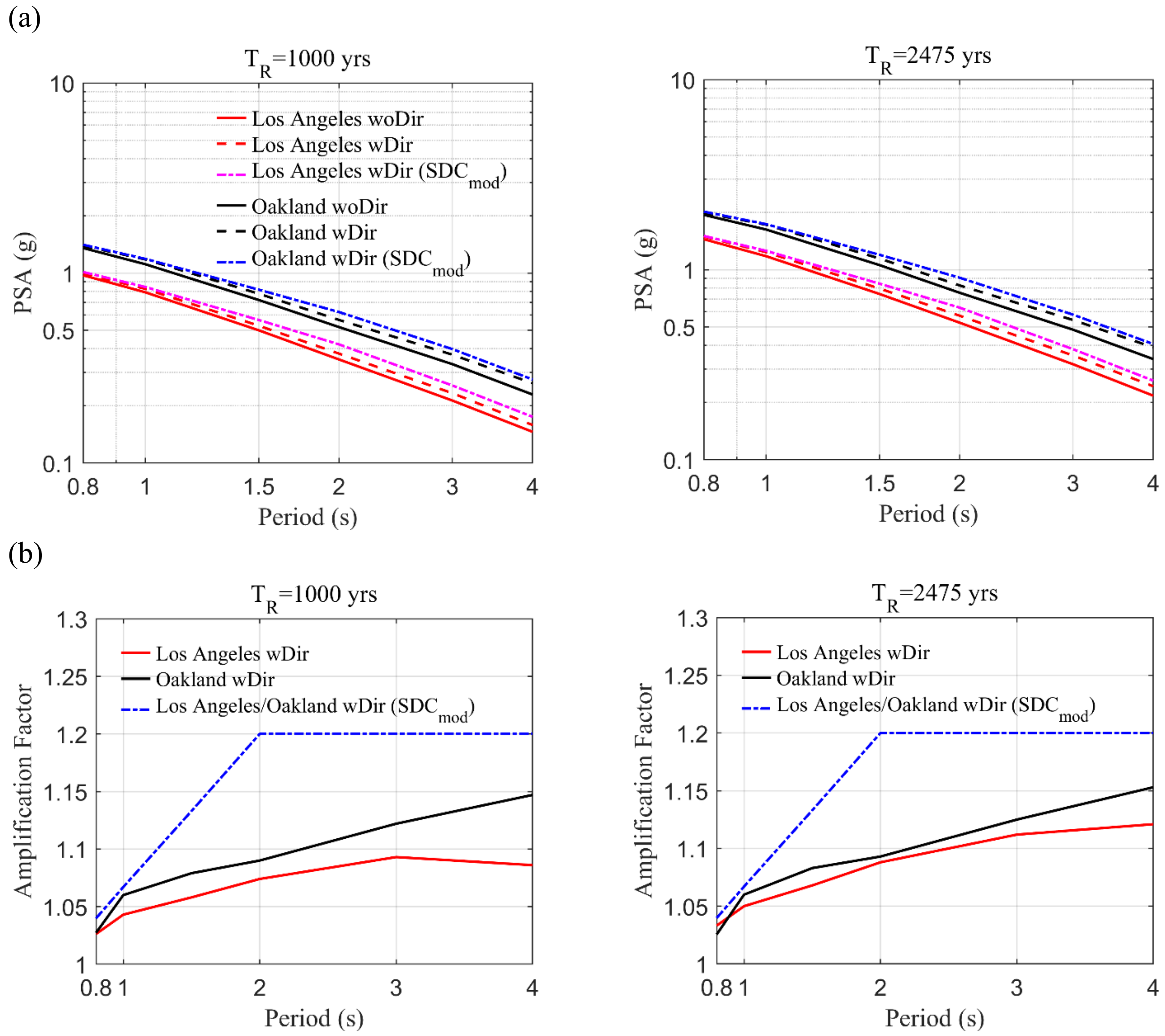

Figure 2-1 *(a) UHS with and without directivity amplification factors in Los Angeles, Oakland, (b) Amplification factor versus period, at the return periods of 1000 and 2475 years.*

2.4. GROUND MOTION SELECTION AND SCALING

The ground motions were selected from the NGA-West2 database (Ancheta et al., 2014) with the following criteria: a moment magnitude (M) greater than 6.5, closest distance to the fault plane R_{rup}< 25 km, the highest usable periods>5.0 seconds, and Vs_{30} values ranging from 180 to 760 m/s. The maximum scale factor was set to 6.0. The ground motions were then classified into pulses and non-pulses. The pulse-like ground motions had pulse periods (T_p) between 0.8 and 4.0 seconds. This range was selected considering the periods of the bridges. The next step was to scale and rank the top candidate motions from each group based on their deviation from the target spectral acceleration. For each target spectrum, the geometric mean of the two horizontal components of the ground motions was used for scaling. The scaling factor was determined by minimizing the deviation between the scaled ground motion spectrum and the target spectral ordinates using the sum of squared errors (SSE) of natural logarithmic differences in spectral accelerations over the specified period range.

When selecting non-pulses, the top 50 to150 candidate ground motions were chosen based on the smallest SSE, while all available pulse motions, typically ranging from 20 to 25 candidates, were considered for selection. With the initial set of top-ranked motions identified, the algorithm proceeded with an iterative greedy selection process. In each iteration, the algorithm evaluated all remaining unselected pulse and non-pulse motions. The algorithm iteratively selected ground motions that minimize the deviation from the target spectral acceleration by evaluating all remaining unselected candidates at each step. The final selection was validated by assessing the mean spectral acceleration of the chosen set against the target spectrum to ensure optimal matching. If only non-pulse motions were required, the pulse motion selection step was skipped entirely.

For both wDir and wDir (SDC_{mod}) cases, 15 pulses out of 20 motions were selected. The proportion of pulses in the set can be estimated as a function of epsilon, where epsilon refers to the number of standard deviations from the median of the GMM, typically spectral acceleration at 1 s at the design seismic hazard level, though peak ground velocity (PGV) is preferably used when available (i.e., the number of standard deviations from the mean of the GMM) and R_{rup} (Hayden et al., 2014). This study ensured that 75% of the ground motions had pulses, corresponding to PSHA disaggregation values of epsilon >1.0 for the 5%-damped spectral acceleration at 1 s, and R_{rup} < 5 km. For the UHS-woDir case, 20 ordinary (non-pulse) ground motions were selected and scaled to be, on average, compatible with the target median. All selected ground motions along with their seismological properties, scale factors, and other relevant details are provided in Appendix 2.B of this report.

Figure 2.2 illustrates an example of the target median spectra for both the woDir and wDir (SDC_{mod}) cases, as well as the scaled record and suite median spectra at a return period of 2475 years in Los Angeles. As seen, the wDir (SDC_{mod}) case demonstrates increased spectral variability for periods longer than 2 seconds. This is due to the distinct spectral characteristics of pulses, in contrast to the woDir case, which includes only ordinary ground motions. The average T_p values in the sets of motions were approximately 2.6 seconds.

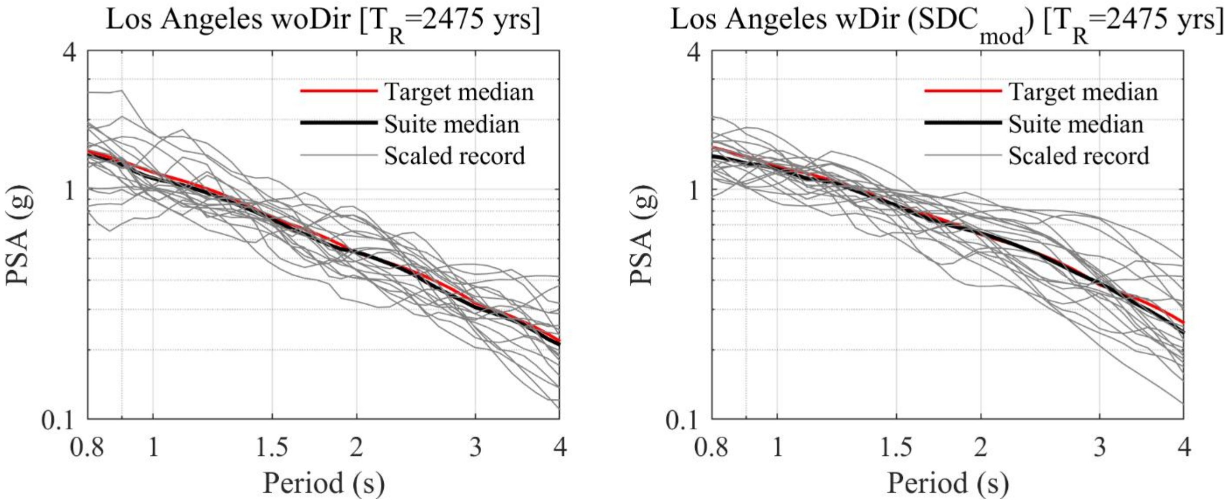

Figure 2-2 *The UHS without and with directivity amplification factors (i.e., woDir and wDir (SDC_{mod})) in Los Angeles at T_R=2475 years. The plots also include the median and individual spectra of 20 scaled ground motions.*

2.5. BRIDGE CONFIGURATIONS AND DESIGN DETAILS

In consultations with Caltrans, two bridges were selected for this study: a three-span bridge with a single-column bent (B-1C) and a three-span bridge with a two-column bent (B-2C). Both bridges have equal side and middle spans, and their key structural and foundation characteristics are summarized in Table 2.1. The superstructures of both bridges consist of five-cell box girders, which are monolithically connected to the piers. The B-1C bridge has an oblong column cross section with longitudinal and transverse reinforcement ratios of 2% and 1%, respectively. The axial load ratio for this bridge is 15%. In contrast, the B-2C bridge has a circular column cross section with longitudinal and transverse reinforcement ratios of 2% and 0.9%, respectively, and an axial load ratio of 13%. Both bridges are supported by seat-type abutments with a skew angle of 0°, which rest on cast-in-drilled-hole (CIDH) piles.

Table 2.1 *Structural and foundation properties of the B-1C and B-2C three-span bridges.*

	Unit	**B-1C Value**	**B-2C Value**
Span Length	Ft	230.0	200.0
Deck Width	Ft	33.0	48.0
Deck Depth	Ft	9.25	8.0
Column Height	Ft	33.0	28.0
Column Section	Ft	5-1/2 × 8-1/4 (Oblong)	5-1/2 (Circular)
Shear Span Ratio	-	3.0 (L) – 2.0 (T)	5.1 (L/T)
Longitudinal Reinforcement	-	72#11 (2%)	44#11 (2%)
Transverse Reinforcement	-	#8@6.0 (1%)	#8@6.0 (0.9%)
Axial Load Ratio	-	15%	13%
Column Foundation Pile Size	In	16 (CIDH)	16 (CIDH)
Column Foundation Pile Number	-	7 × 7	4 × 6

2.6. THREE-DIMENSIONAL NUMERICAL MODELING

To ensure consistency with Caltrans, we used the finite element computer models developed and provided by Caltrans engineers. All numerical analyses were conducted using the OpenSees computational platform (Mazzoni et al., 2006). For representative visualization, Figure 2.3 illustrates the elevation view of the three-span bridge, the modeling scheme of a two-column bent, and the adopted abutment model. For both bridge models, the Concrete02 material model was used to simulate the behavior of concrete under compression and tension, accounting for elastic, inelastic, and post-peak behaviors. The cover concrete has a compressive strength of 5 ksi, while the core concrete (i.e., confined concrete) has a compressive strength of 7.675 ksi, the modulus of elasticity (Ec) was 4030.5 ksi. To simulate the nonlinear responses of columns, nonlinear fiber-section elements (*nonlinearBeamColumn)* were employed. The P-delta effect was included in the bridge model to account for axial load-lateral deformation interaction. The zero-length-section element was used to model the strain penetration effect (*Bond_SP01* material) at both ends of the column. The reinforcement was defined using *Hysteretic* material to capture the force-displacement behavior, including pinching and damage effects, with a yield strength of 68 ksi and an ultimate strength of 89.7 ksi. The superstructure elements, i.e., bridge deck and transverse beams, were modeled using elastic beam-column elements with effective section properties. A spine model was adopted for the superstructure. Rigid links were employed to connect the top of the columns to the deck elements.

Zheng et al. (2021) proposed a refined abutment model by dividing the abutment wall into the backwall and stem wall, allowing for a more accurate spring system. The backfills were modeled using nonlinear springs with hyperbolic backbone, as defined by Xie et al. (2019). Detailed information on the abutment model and backbone curves of the bridge components can be found in Zheng (2021).

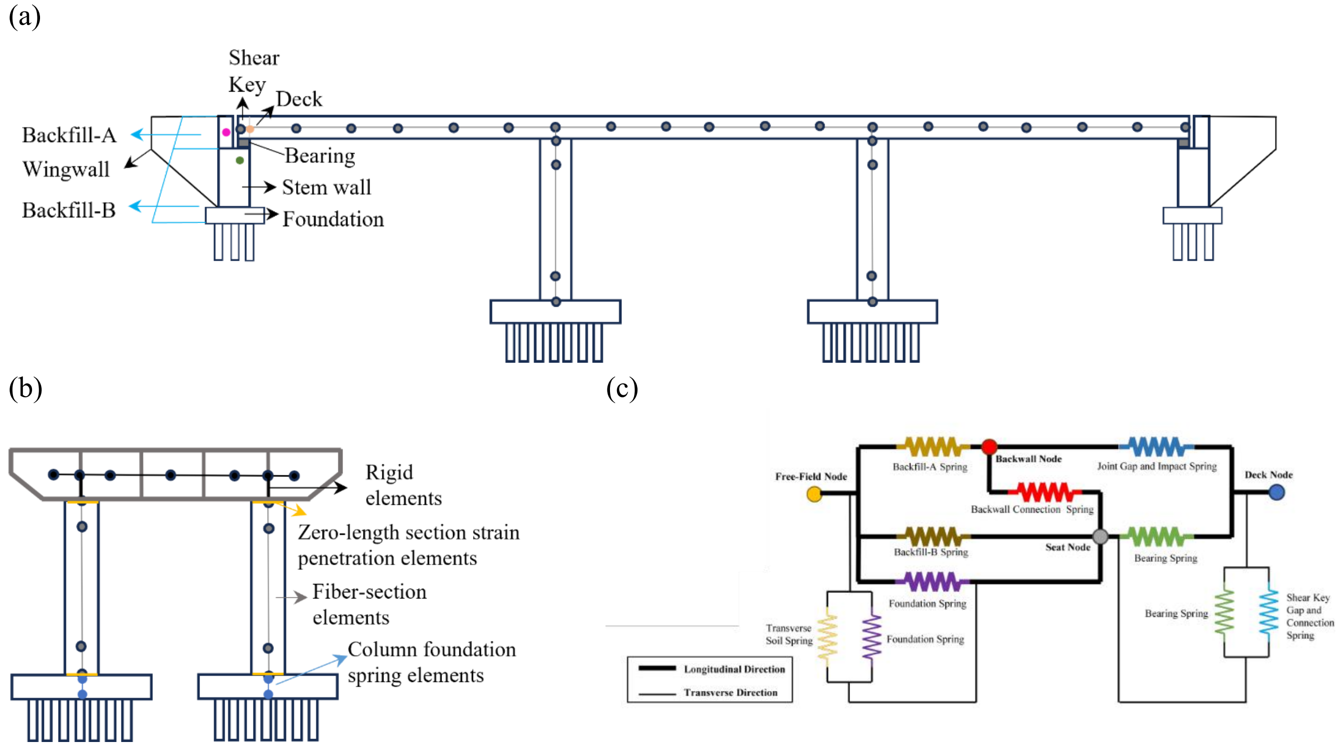

Figure 2-3*(a) Elevation view of the three-span bridge, (b) Modeling scheme of a two-column bent, and (c) Adopted abutment model (after Zheng et al., 2021).*

2.7. MODAL ANALYSIS

Figure 2.4 illustrates the mode shapes and corresponding periods for each bridge model. For the B-1C, the rotational, transverse, and longitudinal periods are 1.88, 1.87, and 1.24 seconds, respectively, while for the B-2C, they are 1.73, 1.41, and 1.34 seconds. Rayleigh damping was implemented using mass-proportional and last committed stiffness-proportional damping. A critical damping ratio of 4.5% was applied to the first and fourth modes of each bridge model. Detailed modal analysis results for the two bridge models are provided in Appendix 2.A of this report.

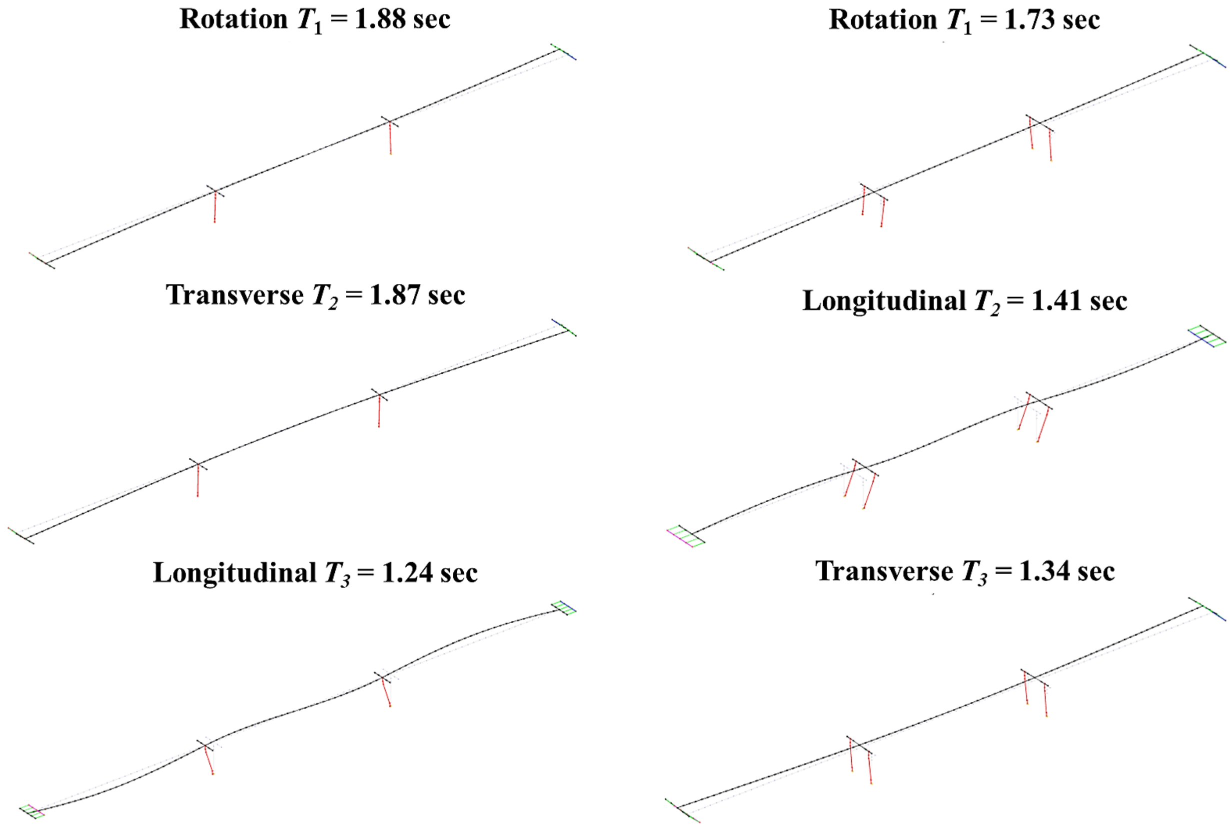

Rotation T_1 = 1.88 sec

Rotation T_1 = 1.73 sec

Transverse T_2 = 1.87 sec

Longitudinal T_2 = 1.41 sec

Longitudinal T_3 = 1.24 sec

Transverse T_3 = 1.34 sec

Figure 2-4 *Mode shapes of the 3D bridge models (Left panel: B-1C, Right panel: B-2C).*

2.8. MOMENT-CURVATURE ANALYSIS

Moment-curvature ($M - \phi$) analyses were performed for the B-1C bridge's oblong column section in both the transverse (strong axis) and longitudinal (weak axis) directions using OpenSees software. The axial load on the column section was 4157 kips. Figure 2.5 depicts the actual and idealized (bilinear) moment-curvature curves for both directions, while Table 2.2 lists the yield curvature, yield displacement, and displacement ductility capacity of the column, obtained from the idealized curve using the formulations in SDC (2019). It was found that the estimated displacement ductility capacities were 14.0 in the transverse direction and 7.5 in the longitudinal direction. For the B-2C bridge, $M - \phi$ analyses were conducted for the circular column section under an axial load of 2240 kips. Figure 2.6 illustrates the actual and idealized (bilinear) moment-curvature curves. Table 2.3 summarizes the key parameters from the idealized curve, with the displacement ductility capacity of the column estimated at approximately 8. Displacement ductility capacities of the three-span bridges were calculated through pushover analysis, as detailed in the following section.

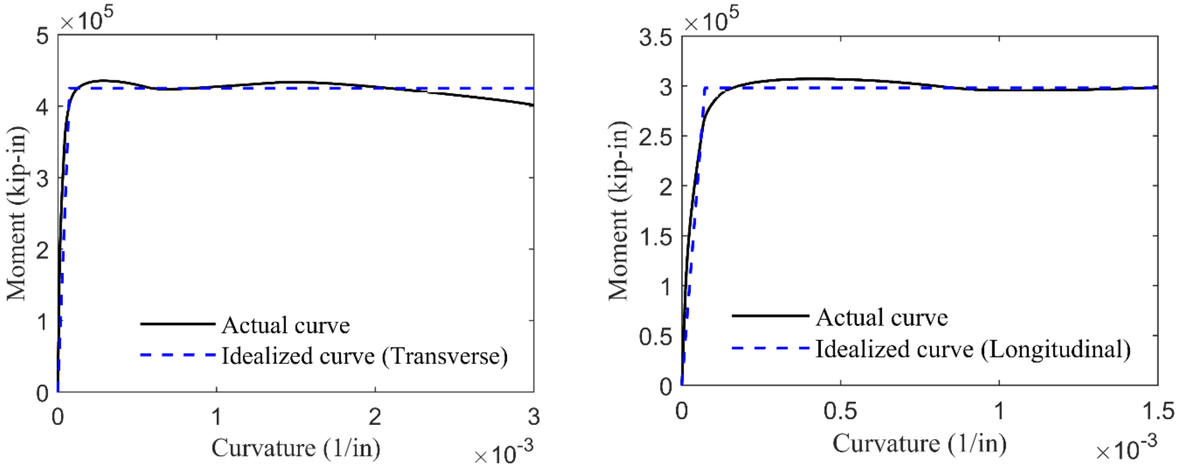

Figure 2-5 *Moment-curvature curves for the B-1C bridge's oblong column section in both the transverse (strong axis) and longitudinal (weak axis) directions*

Table 2.2 *Moment-curvature analysis results based on idealized curve for the B-1C.*

	Transverse	**Longitudinal**
Yield curvature (ϕ_y)	7.37E-5	7.26E-5
Yield displacement (in) (Δ_y)	3.90	3.70
Displacement ductility capacity	14.0	7.5

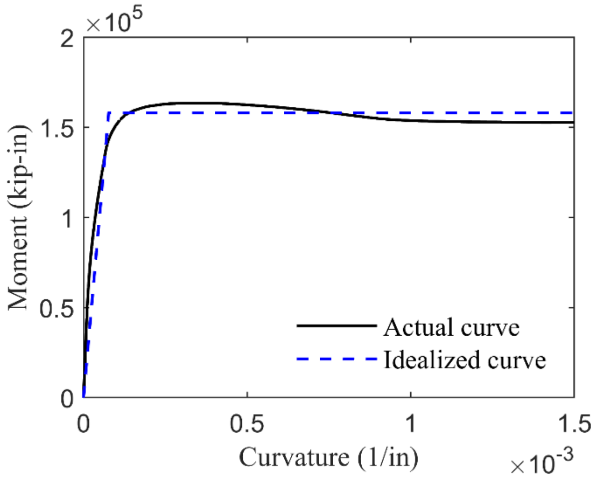

Figure 2-6 *Moment- curvature curves for the circular column section of the B-2C bridge*

Table 2.3 *Moment-curvature analysis results based on idealized curve for the B-2C.*

	Transverse/Longitudinal
Yield curvature (ϕ_y)	7.69E-5
Yield displacement (in) (Δ_y)	3.0
Displacement ductility capacity	7.6

2.9. PUSHOVER ANALYSIS

Displacement-controlled pushover analyses were conducted on the bridge models in both the transverse and longitudinal directions. Incremental loading was applied at the top node of the columns, gradually pushing the bridge to a target displacement of approximately 9% of the total column height (or a drift ratio of 9%). Figure 2.7 illustrates the results of the pushover analysis for the B-1C bridge in both directions. In the transverse direction, the total base shear was determined by summing the base shears for each individual column. For the longitudinal direction, the total base shear included the forces from the abutments and the base shears from the piers. The abutment forces, which include contributions from spring backfills and foundations, were activated once the 2-inch gap between the backwall and deck closed. The pushover curve was approximated by a bilinear relationship using the equal-area method. The ultimate displacement for the bridge was defined as the point at which the base shear dropped to 85% of its peak value. Table 2.4 lists the key parameters from the analysis results. As shown, the displacement ductility capacities of the B-1C bridge, representing the ratio of ultimate displacement to yield displacement, were found to be 6.0 in the transverse direction and 8.0 in the longitudinal direction. The associated column drift ratio capacities were 8% and 9%, respectively.

Figure 2.8 and Table 2.5 present the corresponding results for the B-2C bridge. In comparison, the displacement ductility capacities for the B-2C bridge were found to be slightly lower than those of the B-1C bridge, with values of 5.9 in the transverse direction and 6.1 in the longitudinal direction. The column drift ratio capacities for the B-2C bridge were also slightly lower, with values of 6% and 8%, respectively.

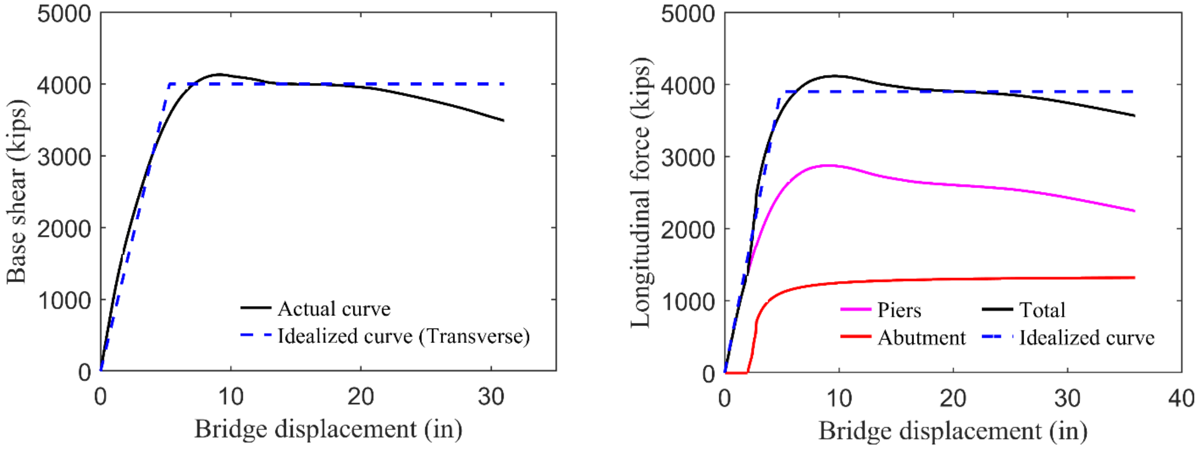

Figure 2-7 *Pushover curves in the transverse (left panel) and longitudinal (right panel) directions for the B-1C.*

Table 2.4 *Pushover analysis results based on idealized curves for the B-2C*

B-1C	Column height (in)	Yield displacement (in)	Ultimate displacement (in)	Displacement ductility capacity	Column drift ratio capacity
Longitudinal	396	4.9	36	8.0	9%
Transverse		5.3	31	6.0	8%

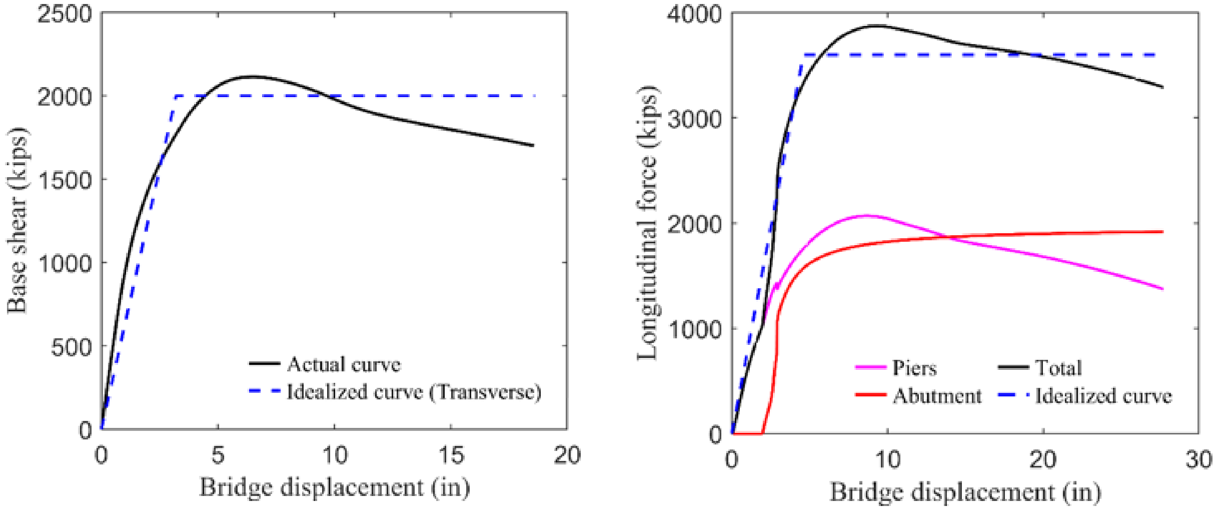

Figure 2-8 *Pushover curves in transverse (left panel) and longitudinal (right panel) directions for the B-2C*

Table 2.5 *Pushover analysis results based on idealized curves for the B-2C*

B-2C	Column height (in)	Yield displacement (in)	Ultimate displacement (in)	Displacement ductility capacity	Column drift ratio capacity
Longitudinal	336	4.6	28	6.10	8%
Transverse		3.2	19	5.90	6%

2.10. NONLINEAR TIME HISTORY ANALYSIS

To investigate the effects of ground motion directionality on bridge responses, the ground motions were rotated in 15° increments over a range of 0° to 90°. The ground motions were first rotated to fault-normal (FN) and fault-parallel (FP) directions. At an incidence angle of 0°, the FN component was applied in the transverse (T) direction and the FP component in the longitudinal (L) direction. At a 90° incidence angle, the FP component was applied in the T- direction and the FN component was applied in the L- direction. The two rotated horizontal components of the ground motion were applied simultaneously to the T- and L- directions of the bridge, i.e., bidirectional loading. Figure 2.9(a) illustrates the scaled (Scale factor=1.36) and 30°-rotated acceleration time series of the 1994 Northridge earthquake (RSN 1013-LA Dam station), representing a 1000-year event in Los Angeles, applied to the transverse and longitudinal directions of the two bridge models. Figure 2.9(b) depicts the resulting displacements in each direction for the B-1C and B-2C models. The CDR was calculated as the ratio of the maximum absolute bridge displacement (measured at the column top) to the column height. B-1C exhibited higher initial stiffness and a longer transverse period (1.87 s), whereas B-2C had lower stiffness but a shorter transverse period (1.34 s). The shorter period of B-2C aligned more closely with the pulse period of the ground motion, leading to dynamic amplification. This resonance effect combined with normalization by its shorter column height resulted in higher CDR for B-2C. It should be noted that this calculation captured only the flexural deformation of the columns, excluding any displacement contributions from rigid body rotation associated with foundation flexibility. The RDR was computed as the ratio of permanent displacement observed at the column top to the height. For this ground motion, while both bridges showed similar permanent displacements in the longitudinal direction, the B-1C model demonstrated better recentering behavior in the transverse direction.

Figure 2.10 illustrates the mean CDR and μ_D responses obtained from the sets of 20 woDir, wDir, and wDir (SDC_{mod}) motions in both the T- and L- directions of the B-1C model for seven different incidence angles, while Figure 2.11 shows the corresponding results for the B-2C model. The case where the CDR exceeded the CDR capacity obtained from pushover analysis was defined as collapse, and the responses from those ground motion were assumed as the capacity CDR values (e.g., 9%) in the computation of the mean responses at each incidence angle. The figures also depict the ratios of the CDRs to CDR_{RotD50}, where CDR_{RotD50} was computed as the median values of CDRs over seven incidence angles. In this context, the RotD50 captures the central tendency of structural responses. This indicates that the responses exhibit variability around their respective medians, highlighting the influence of directional effect on bridge response. Tables 2.6 and 2.7 list the number of collapses at each incidence angle for the B-1C and B-2C, respectively, in Los Angeles.

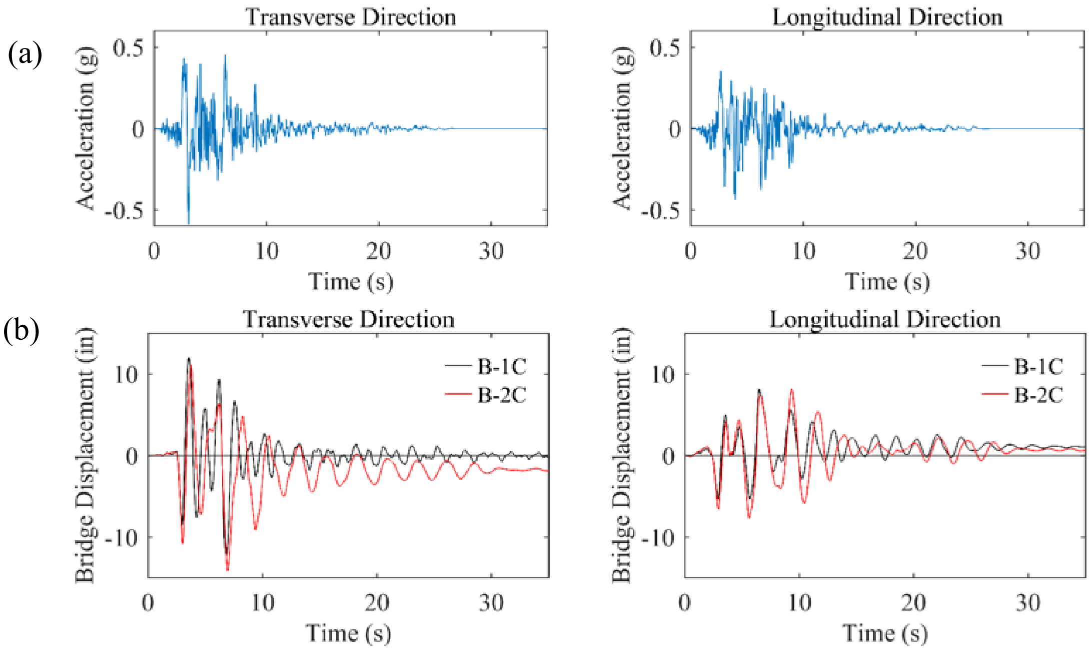

Figure 2-9 *(a) Scaled (Scale factor=1.36) and 30°-rotated 1994 Northridge earthquake record (RSN 1013) representing a 1000-year event in Los Angeles, applied to the transverse and longitudinal directions of the bridge models, (b) Transverse and longitudinal displacements for B-1C and B-2C bridge models*

For the B-1C model, at T_R =1000 years, the average CDR was 3%, with μ_D values ranging from 1.9 to 2.5 in the T- and L- directions, respectively. On average, μ_D values were higher in the L- direction. The critical angle maximizing the transverse response was typically between 0-45°, whereas the maximum longitudinal response occurred at 90°, where the FN components produced the highest CDRs. In the L-direction, CDRs from wDir and wDir (SDC_{mod}) motions underestimated CDR_{RotD50} by approximately 20% between 0-45° but exceeded it by a similar margin between 45-90°. This difference was more pronounced compared to woDir motions. In the T- direction, both wDir and woDir cases showed similar trends, though deviations were larger in wDir cases. The ratio of CDR/CDR_{RotD50} results indicated higher transverse responses between 0-45° and comparable or lower responses between 45-90°. Trends observed in CDR/ CDR_{RotD50} at T_R =1000 years remained consistent at T_R=2475 years. At T_R=2475 years, the average CDR was 5%, with mean μ_D values of 3.3 and 4.0 in the T- and L- directions, respectively. For the woDir motions, CDR variations are approximately 10%, corresponding to an increase in μ_D from 2.9 to 3.3. However, for the wDir (SDC_{mod}) motions, the percentage difference between minimum and maximum CDRs reached approximately 58% in the L- direction and 30% in the T- direction, leading to μ_D values exceeding 3.5. Statistical analysis using a two-sample t-test (ttest2) confirmed that these variations are statistically significant, indicating that the directionality in seismic loading have an impact on responses. These results suggest that the near-fault motions could produce high variation in the response depending on the incidence angle and this effect seemed to be more pronounced when bridge behaves highly nonlinear at higher hazard levels, thus neglecting this effect may impact the accuracy of the seismic performance prediction of the bridges.

For the B-2C model, at T_R=1000 years, CDRs and μ_D values ranged from 3.3-3.7% and 2.45-2.7, respectively, in the L- direction. In the T- direction, CDRs and μ_D values ranged from 3.6-4.0% and 3.8-4.3, respectively. The lower transverse yield displacement compared to the L-direction resulted in higher μ_D values in the T- direction. At T_R=2475 years, CDRs in the T- and L- directions were approximately 5.5% and 6%, respectively. In the L-direction, μ_D values ranged from 4.2 to 4.6, while in the T-direction, they averaged 5.5. This suggests that the bridge may be at risk of significant damage, given that its transverse ductility capacity is limited to 5.9. For the woDir motions, variability around CDR_{RotD50} was within ±10%, but this variability did not show statistical significance in both directions. For the wDir and wDir (SDC_{mod}) motions, responses at incidence angles between 15-60° showed comparable or higher-than-average responses in the T-direction. The critical angle in the L- direction was 90°. Similar to the observations in the B-1C model, the wDir (SDC_{mod}) motions resulted in variations of up to 30% in the T-direction and 50% in the L-direction.

As shown in Tables 2.6 and 2.7, for both bridges, the most collapse cases were observed in the wDir (SDC_{mod}) motions at T_R=2475 years. The collapse behavior demonstrated a dependency on incidence angle, with T-direction collapses predominantly occurring within the 0-45° range and L-direction collapses within 45-90°. Since the two horizontal components of the ground motions were applied simultaneously along the principal axes of the bridges, certain ground motions induced in-plane rotations, amplifying responses in both the T- and L- directions. Specifically, it is possible that the first mode of the bridge, particularly the torsional mode, coupled with the period of pulse-like motions, amplifying the torsional effects. To investigate the origin of torsional excitation, analyses were conducted applying unidirectional ground motion only in the transverse direction (no longitudinal component). This produced negligible in-plane rotation, whereas bidirectional loading induced torsional effects, confirming that torsional excitation primarily results from modal coupling under combined excitation.

As an illustration, Figure 2.12 presents the in-plane torsion for both bridges at incidence angles of 0°, 30°, and 90°, based on the 1994 Northridge earthquake ground motion (RSN1013) in Los Angeles with T_R=1000 years. These rotations were computed as the lateral displacement differences between abutments divided by the total span length of the bridge. The results indicated that directivity motions could exacerbate in-plane rotations, with their impact varying based on the incidence angle and the bridge characteristics.

The results highlight that variations across incidence angles can influence the severity of bridge damage, especially when μ_D >3.5, a condition that tends to occur at high seismic hazard levels (e.g., T_R=2475 years). While woDir motions showed relatively small variations, directivity motions led to significant differences in structural response. Although similar trends were observed across different hazard levels, the extent of ductility demand and collapse cases varied. These findings emphasize that at T_R=2475 years, the choice of incidence angle can be a critical factor in whether a bridge experiences severe damage or even collapse. This underscores the need to account for incidence angle effects in seismic design and assessment particularly for sites located in high seismic regions.

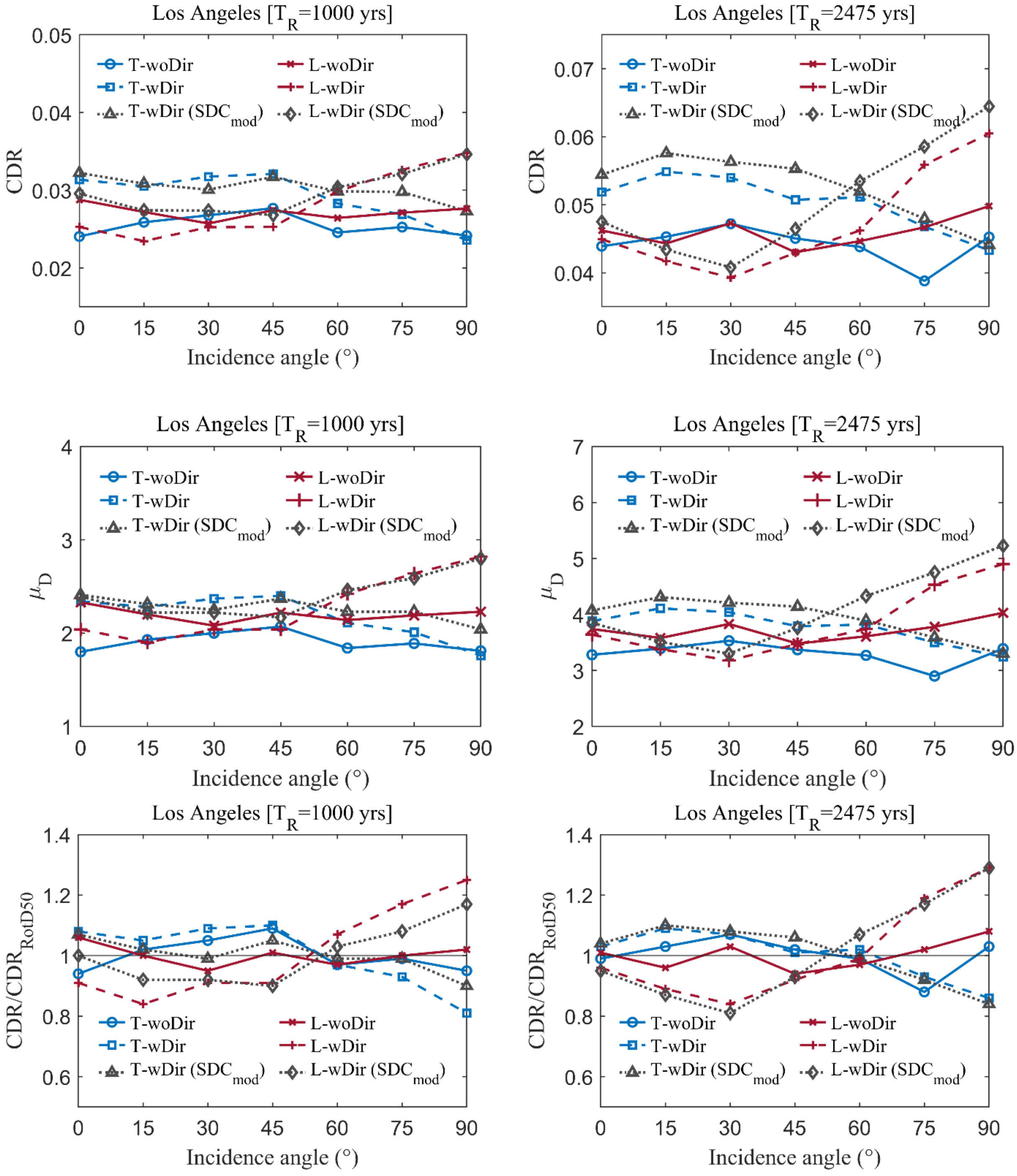

Figure 2-10 *Mean column drift ratio (CDR), and ductility demand (μD) responses from the 20 woDir, wDir, and wDir (SDC$_{mod}$) motions in the T- and L- directions of the B-1C model for seven incidence angles, along with the ratios of the CDR to CDR$_{RotD50}$, in Los Angeles, at T$_R$=1000 years and 2475 years*

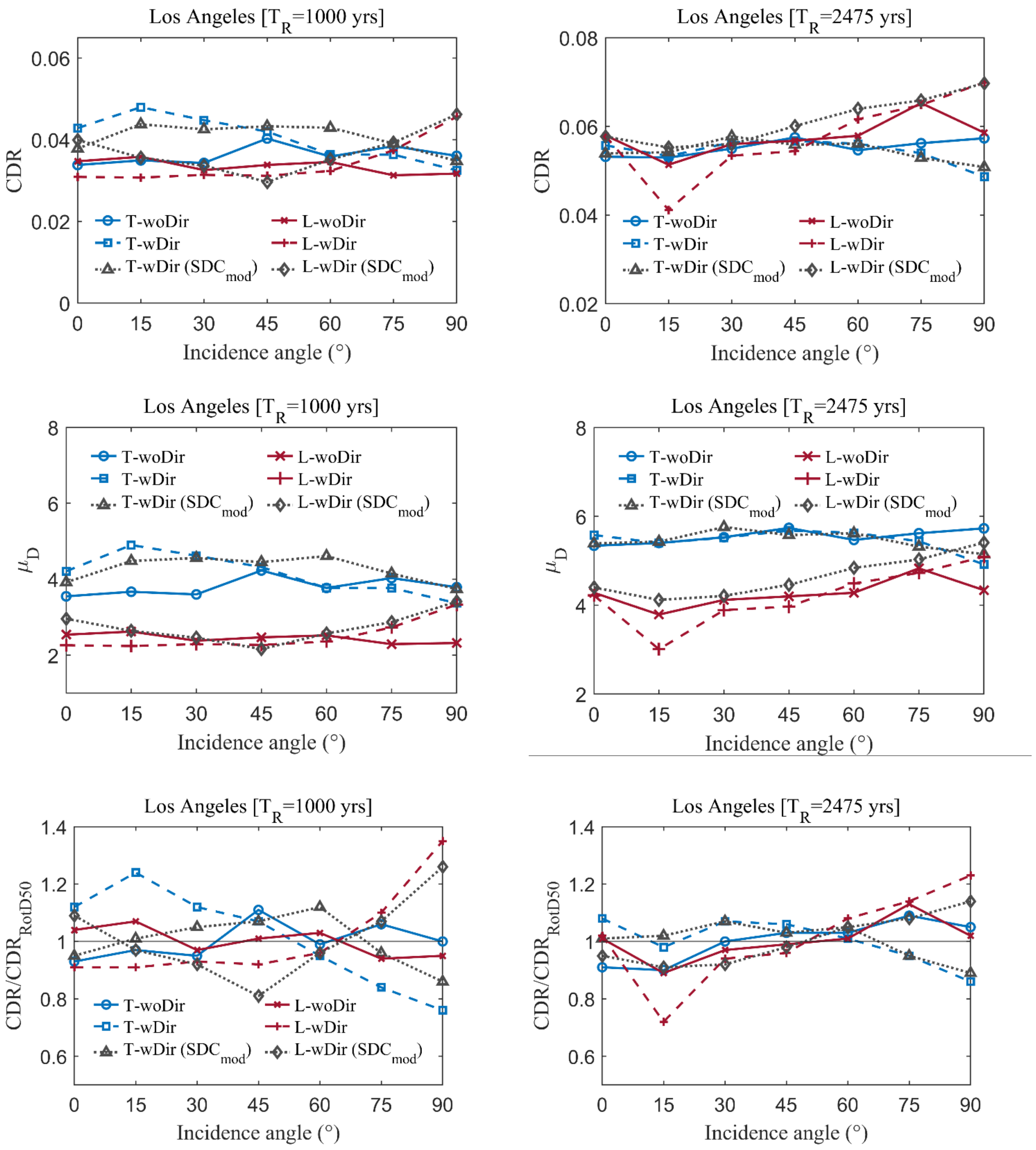

Figure 2-11 *Mean column drift ratio (CDR), and ductility demand (μ_D) responses from the 20 woDir, wDir, and wDir (SDC$_{mod}$) motions in the T- and L- directions of the B-2C model for seven incidence angles, along with the ratios of the CDR to CDR$_{RotD50}$, in Los Angele s, at T_R=1000 years and 2475 years*

Table 2.6 *The number of collapses out of 20 ground motions at each incidence angle in Los Angeles for the B-1C.*

		Incidence Angle (°)						
Los Angeles	**CDR**	**0**	**15**	**30**	**45**	**60**	**75**	**90**
T_R=1000 yrs	**T-woDir**	-	-	-	1	-	-	-
	T-wDir	-	-	-	-	-	-	-
	T-wDir (SDC$_{mod}$)	0	0	0	0	0	1	0
	L-woDir	-	-	-	1	-	-	-
	L-wDir	-	1	1	-	1	1	1
	L-wDir (SDC$_{mod}$)	0	1	1	0	0	0	0
T_R=2475 yrs	**T-woDir**	-	-	1	-	-	-	1
	T-wDir	2	2	-	1	2	1	2
	T-wDir (SDC$_{mod}$)	2	2	2	3	2	1	1
	L-woDir	-	-	2	-	-	1	2
	L-wDir	-	2	1	-	-	2	3
	L-wDir (SDC$_{mod}$)	2	1	1	1	2	3	5

Table 2.7 *The number of collapses out of 20 ground motions at each incidence angle in Los Angeles for the B-2C.*

		Incidence Angle (°)						
Los Angeles	**CDR**	**0**	**15**	**30**	**45**	**60**	**75**	**90**
T_R=1000 yrs	**T-woDir**	-	-	-	-	-	-	-
	T-wDir	2	3	1	1	-	-	-
	T-wDir (SDC$_{mod}$)	0	1	3	2	2	2	1
	L-woDir	-	-	-	-	-	-	-
	L-wDir	-	-	1	1	-	-	1
	L-wDir (SDC$_{mod}$)	1	1	0	0	0	0	1
T_R=2475 yrs	**T-woDir**	1	3	6	8	7	6	6
	T-wDir	7	5	9	9	8	7	5
	T-wDir (SDC$_{mod}$)	9	9	12	12	12	9	8
	L-woDir	3	3	2	3	3	4	3
	L-wDir	3	1	3	2	3	2	4
	L-wDir (SDC$_{mod}$)	5	2	4	3	6	7	10

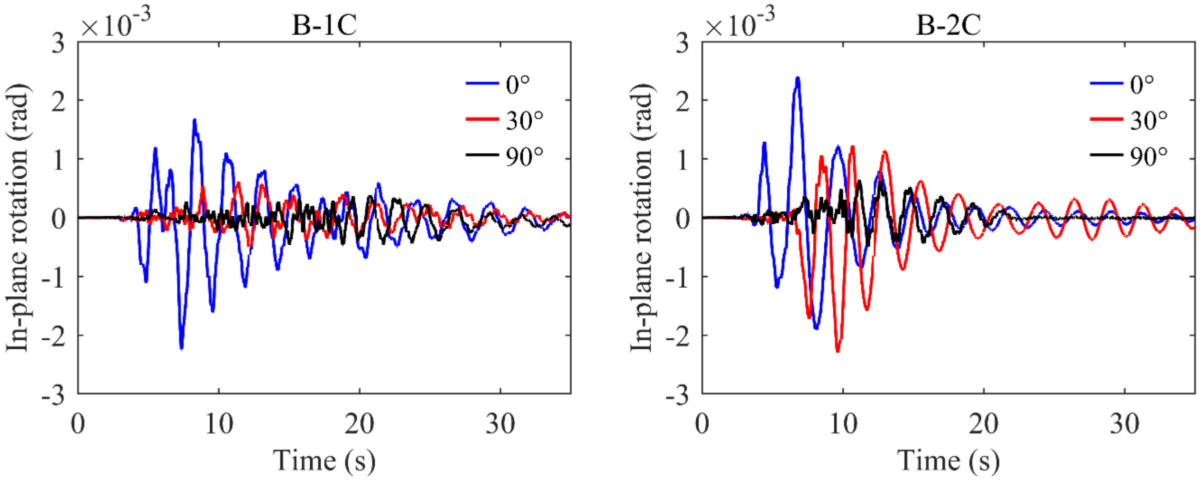

Figure 2-12 *In-plane rotations for the B-1C and B-2C models at incidence angles of 0°, 30°, and 90°, based on the 1994-Northridge earthquake ground motion (RSN1013), representing* T_R*=1000 years in Los Angeles*

The residual displacement, RDR, serves as an important response metric for assessing structural damage and guiding post-earthquake repair decisions, influencing the serviceability and safety of the bridge. Figures 2.13 and 2.14 illustrate the mean RDRs obtained from sets of 20 woDir, wDir, and wDir (SDC_{mod}) motions in both the T- and L- directions for the B-1C and B-2C models, respectively, at seven different incidence angles, for T_R=1000 years and T_R=2475years.

For the B-1C model, RDRs range from 0.2% to 0.35% at T_R=1000 years, and from 0.6% to 0.9% at T_R=2475 years. In general, wDir (SDC_{mod}) and wDir motions tended to produce comparable or slightly higher RDRs than woDir motions, with the increase becoming more significant under higher hazard levels, in line with previous studies (Phan et al. 2007, Choi et al. 2010, Zengin et al. 2025a). Interestingly, no clear trend was observed for RDR/RDR_{RotD50} with respect to incidence angle, although the critical angle for the L- direction tended to align with 90°. It was observed that as the CDR increased, the RDR also increased. However, the high uncertainty in the RDRs prevented a strong alignment with the CDR patterns.

For the B-2C model, the mean RDRs were approximately 0.5% at T_R=1000 years and around 1.0% at T_R=2475 years. While the average RDRs remained below the 1% post-earthquake serviceability limit set by some design codes such as those from Japan (JSCE, 2000), the large dispersion, especially in wDir (SDC_{mod}) and wDir motions, suggested that the 84th percentile of RDRs could exceed this threshold. This increased exceedance risk at T_R=2475 years needs attention to the long-term functionality of the bridges. The subsequent section further explores dispersion in RDRs.

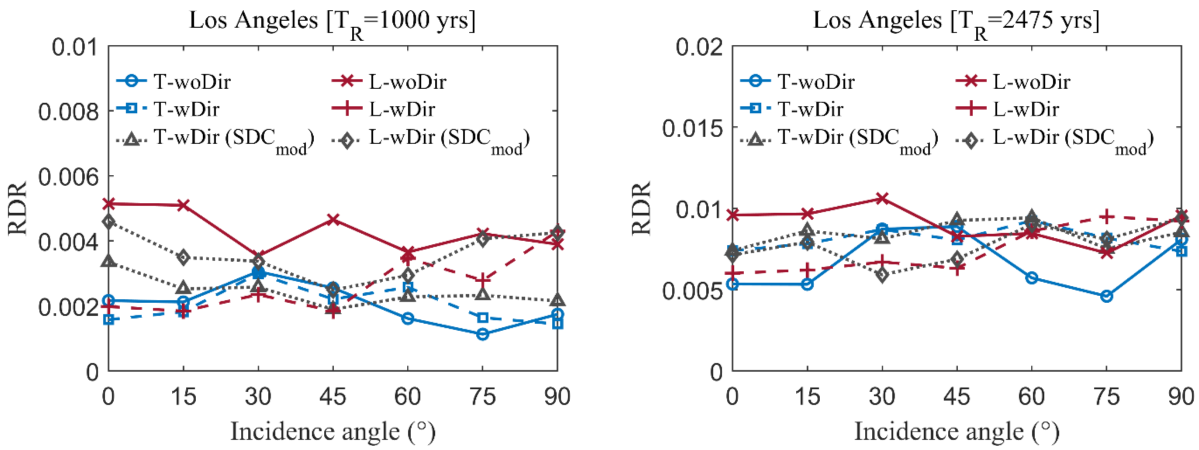

***Figure 2-13** Mean residual drift ratio (RDR) obtained from sets of 20 woDir, wDir, and wDir (SDCmod) motions in both the transverse (T) and longitudinal (L) directions for the B-1C model, at seven different incidence angles, for T_R=1000 years and 2475years.*

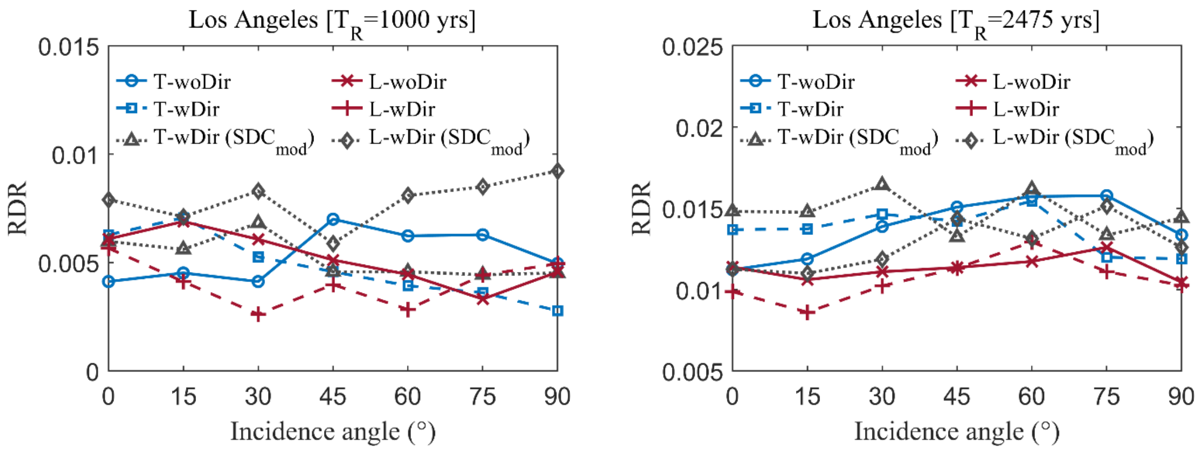

***Figure 2-14** Mean residual drift ratio (RDR) obtained from sets of 20 woDir, wDir, and wDir (SDCmod) motions in both the transverse (T) and longitudinal (L) directions for the B-2C model, at seven different incidence angles, for T_R=1000 years and 2475years*

Figures 2.15 and 2.16 illustrate the standard deviations of the natural logarithms of CDR ($\sigma_{ln(CDR)}$)) and RDR ($\sigma_{\ln(RDR)}$), for the B-1C and B-2C models, respectively. It was observed that $\sigma_{ln(CDR)}$ values ranged from 0.3 to 0.5, with wDir and wDir (SDC$_{mod}$) motions generally producing the highest variability in both the T- and L- directions. A slight reduction in $\sigma_{ln(CDR)}$ was observed at T_R=2475 years, as these standard deviations were estimated based on the pooled collapse and non-collapse responses. When estimating the probability of collapse or exceeding some damage limit state, it is important to separate collapse and non-collapse data for accuracy. The probability of exceeding a specific response parameter threshold at a given seismic hazard level should first be calculated using non-collapse responses to account for its variability. The collapse probability at that level can be estimated by the fraction of collapse responses. To determine the overall probability of exceeding damage or collapse limit, the probabilities from both collapse and non-collapse cases can be summed. The use of pooled data allows for a general assessment of the bridges overall seismic behavior under different ground motions, as the probabilistic evaluation of limit state exceedance is outside the scope of this study.

For $\sigma_{\ln(RDR)}$, the values ranged from 0.75 to 2.0, with the high dispersion not consistently associated with wDir or wDir (SDC_{mod}) motions. The woDir motions might produce comparable variability depending on the incidence angles and response directions. The higher dispersions observed in RDRs compared to CDR (or μ_D), are in line with the findings of Zengin et. al. (2025b). As noted, since the 84th percentile of RDRs may affect bridge functionality and serviceability, the variation in standard deviation due to incidence angle highlights the importance of considering this factor in seismic bridge design.

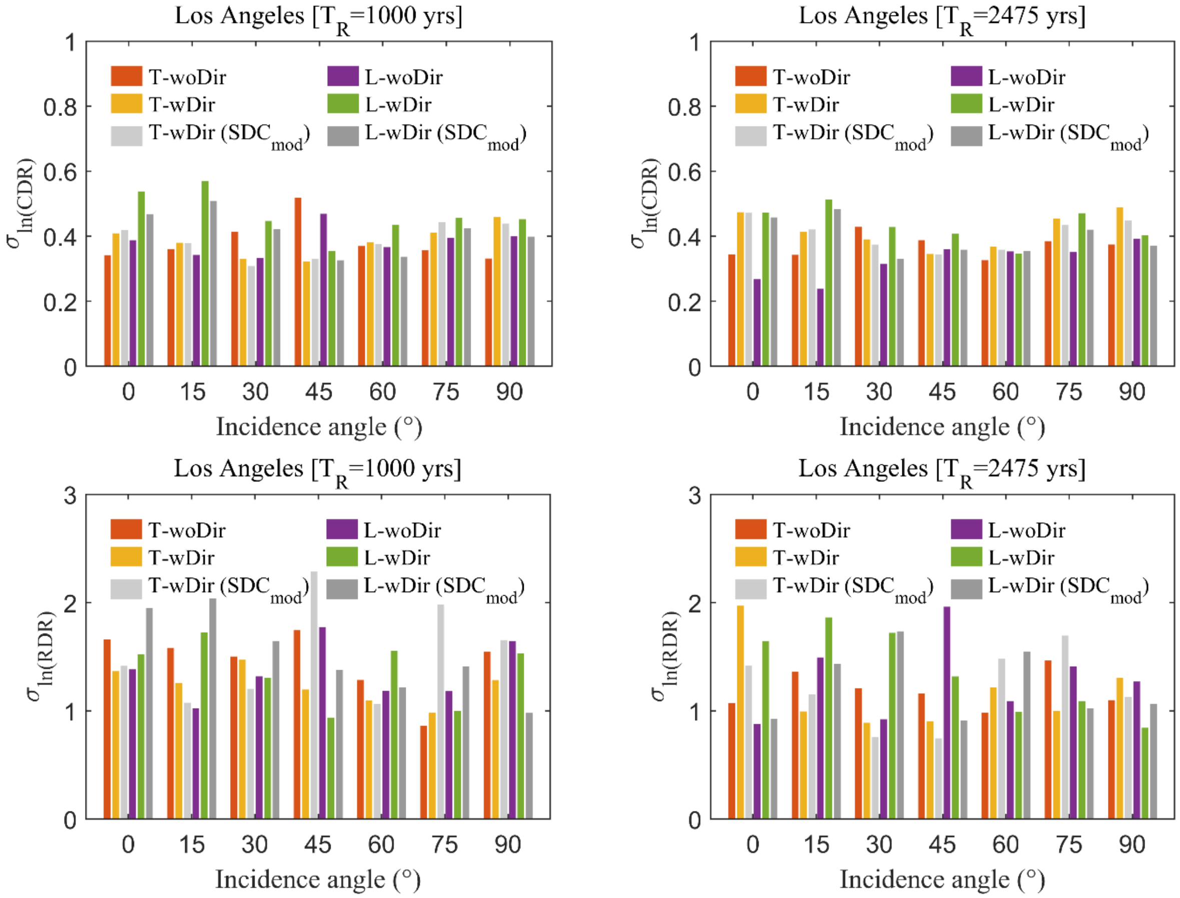

Figure 2-15 *Standard deviations of the natural logarithms of CDR and RDR for the B-1C model, in Los Angeles, at T_R=1000 years and 2475 years.*

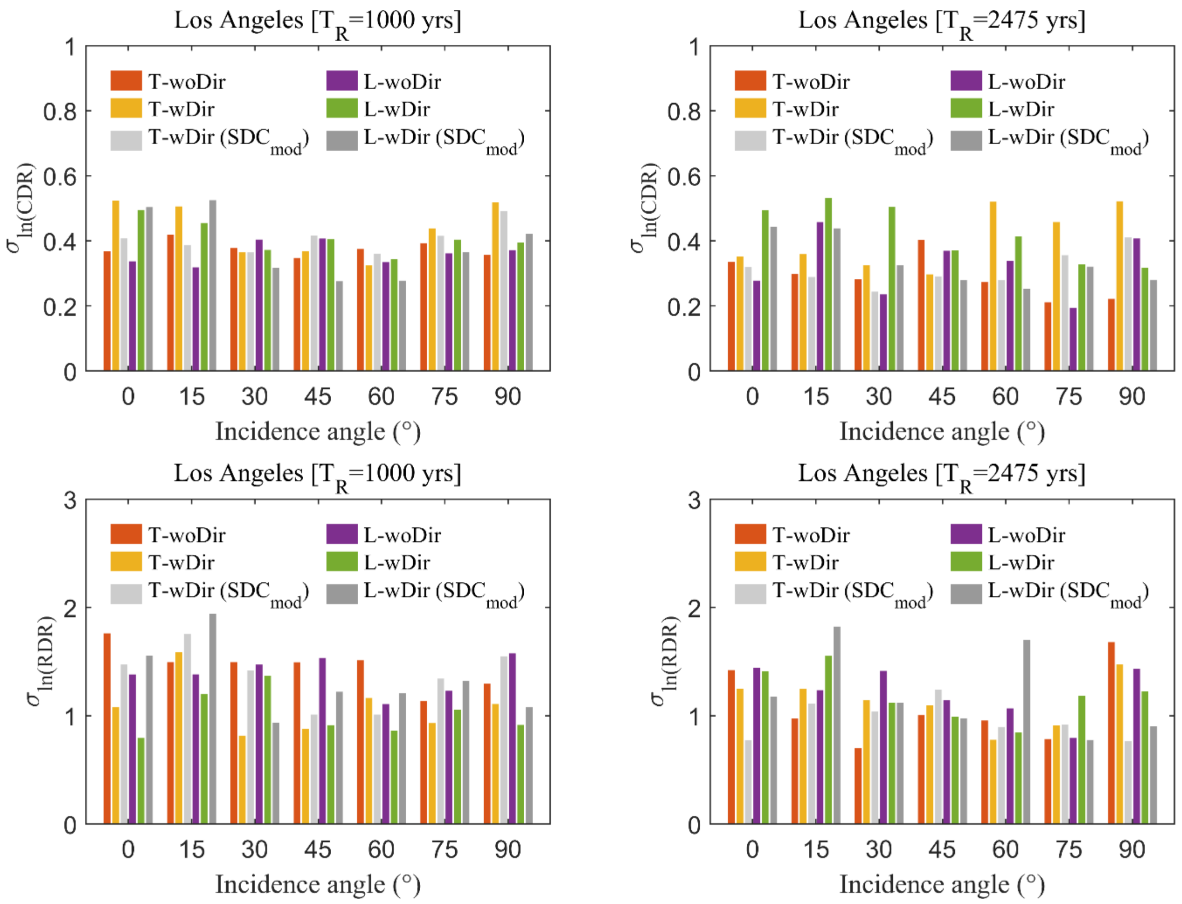

Figure 2-16 *Standard deviations of the natural logarithms of CDR and RDR for the B-2C model, in Los Angeles, at T_R=1000 years and 2475years.*

Figure 2.17 illustrates the mean CDR, μ_D, CDR/CDR_{RotD50}, and RDR responses obtained from the sets of 20 woDir, wDir, and wDir (SDC_{mod}) motions in both the T- and L- directions of the B-1C model for seven different incidence angles, T_R=1000 years, in Oakland. Table 2.8 lists the number of collapses at each incidence angle in Oakland. As seen in Figure 2.17, while woDir and wDir ground motions produced similar CDRs on average, wDir (SDC_{mod}) resulted in approximately 10% higher CDRs, with an average of around 5%. The μ_D values were between 3.0 and 5.0. The number of collapses observed in Oakland at T_R=1000 years was higher than in Los Angeles, consistent with Oakland's higher seismicity. Similar to the observations in Los Angeles, most collapse cases resulted from wDir (SDC_{mod}) motions. Trends observed for the CDR/CDR_{RotD50} were also consistent with those in Los Angeles. Critical responses in the T-direction were concentrated between 0-45°, while the highest CDRs in the L- direction were associated with 90° or the FN component. Note that at T_R=2475 years, the elastic spectral ordinates nearly doubled, leading to numerous collapses and non-convergence issues for most ground motions. This indicates a risk of severe damage and possible collapse at the Oakland site; thus, the results are not reported due to unreliable statistics. Similarly, for the B-2C model, μ_D values exceeded Caltrans' target ductility demand limit of 5, indicating that this bridge model lacks sufficient capacity to withstand Oakland's high seismic demands. This underscores the need for site-specific seismic design in high-seismic zones like Oakland, where extreme events significantly increase the risk to bridges located in near-fault regions. The RDR values ranged between 0.7% and 0.9%. RDRs from wDir (SDC$_{mod}$) were about 20% higher than woDir in the T-direction, while woDir had 10% higher RDRs in the L- direction. The results suggest that given the large dispersion in RDRs, combined with the presence of very small values (e.g., RDR <1%) the differences in mean values across incidence angles are unlikely to significantly influence post-earthquake decision-making regarding structural usability or repairability.

Figure 2.18 illustrates the standard deviations of the natural logarithms of CDR and RDR in Oakland, displaying similar trends with those observed in Figures 2.15 and 2.16. The results suggest that the variations in dispersion of RDRs with respect to ground motion incidence angle are higher than those observed in CDRs.

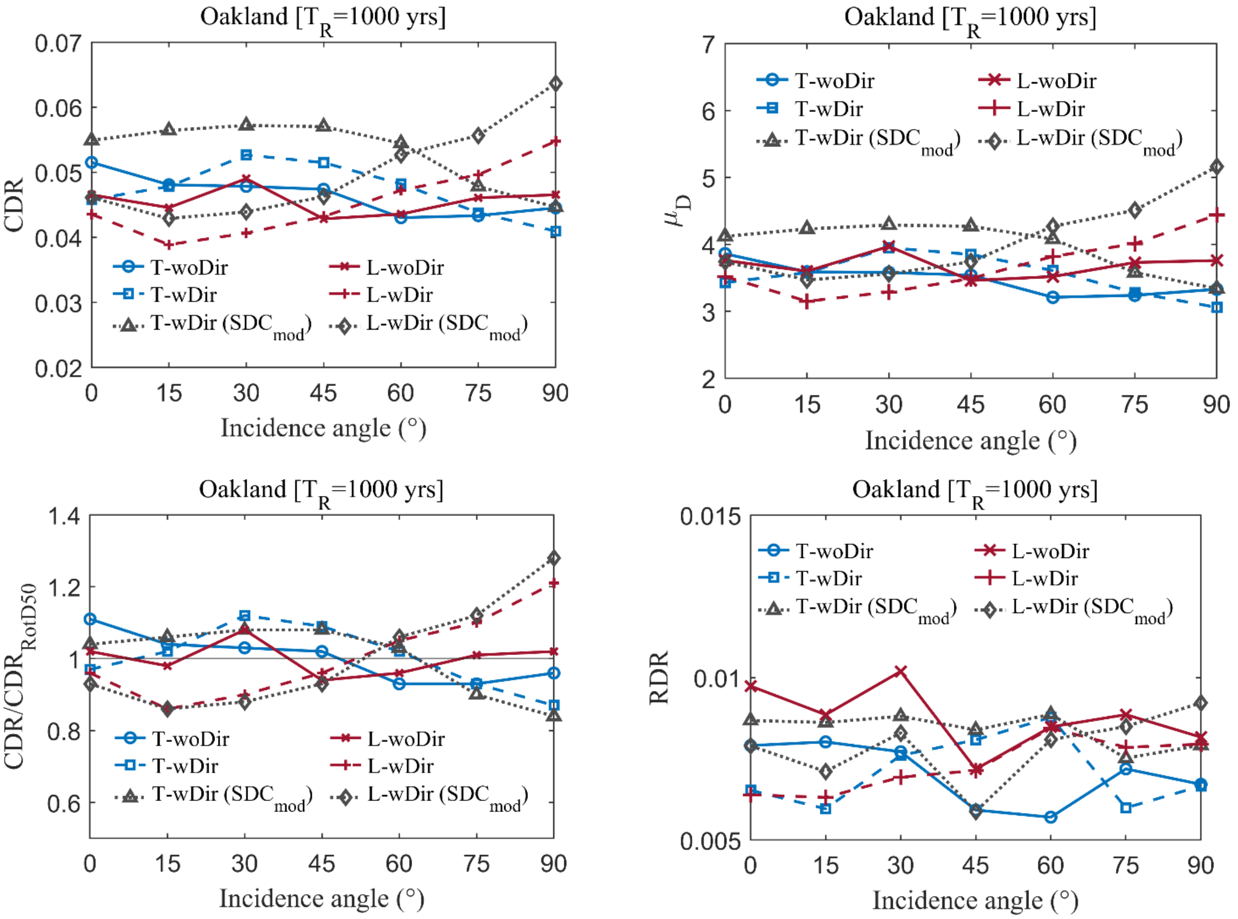

Figure 2-17 *Mean column drift ratio (CDR), and ductility demand (μ_D), ratios of the CDR to CDR$_{RotD50}$, and residual drift ratio (RDR) from the 20 woDir, wDir, and wDir (SDC$_{mod}$) motions in the T- and L-directions of the B-1C model for seven incidence angles, in Oakland, at T_R=1000 years.*

Table 2.8 *The number of collapses out of 20 ground motions at each incidence angle in Oakland for the B-1C.*

		Incidence Angle (°)						
Oakland	CDR	**0**	**15**	**30**	**45**	**60**	**75**	**90**
T_R=1000 yrs	**T-woDir**	2	0	1	0	0	1	0
	T-wDir	2	2	4	2	1	1	1
	T-wDir (SDC$_{mod}$)	4	4	6	2	3	2	2
	L-woDir	1	0	1	0	0	2	1
	L-wDir	1	1	2	1	2	1	3
	L-wDir (SDC$_{mod}$)	2	2	2	2	2	2	5

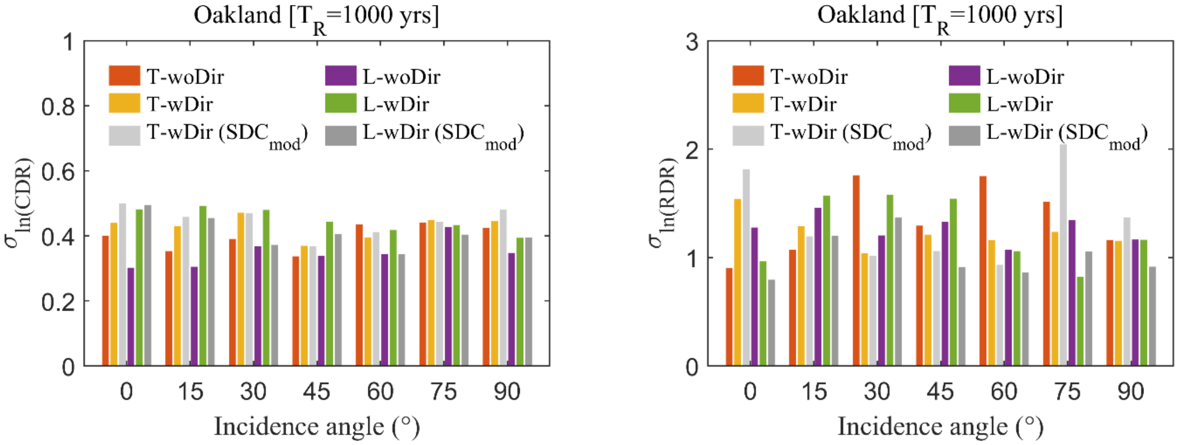

Figure 2-18 *Standard deviations of the natural logarithms of CDR and RDR for the B-1C model, in Oakland, at TR=1000 years.*

2.11. COMPARISONS BETWEEN NTHA AND SDOF ANALYSES RESULTS

This section presents a comparison between the CDRs and RDRs obtained from NTHA and the inelastic SDOF systems. The validity of the equal displacement rule between elastic and inelastic responses is also assessed. The inelastic SDOF systems, characterized based on the Takeda hysteretic model (Takeda et al., 1970), were analyzed. The behavior of these systems was defined using the seismic coefficient (Cy), which represents the ratio of the yield force to the total weight of the bridge, along with a post-yield stiffness that incorporates a 2% strain-hardening effect. A viscous damping ratio of 5% was applied. From the pushover analysis, the Cy values for the B-1C were found to be nearly identical in both the T- and L- directions (see Figure 2.7), with values of approximately 0.37. For the B-2C, Cy in the T- and L- directions were 0.22 and 0.32, respectively. Instead of relying on a single effective period for the SDOF system, we examined six distinct periods ranging from 0.8 to 2.0 seconds to assess the sensitivity of the results to period variations and period lengthening. The CDRs for the SDOF systems were determined by dividing the maximum inelastic displacement by the column height of the bridge.

Figure 2.19 compares the transverse CDR (CDR_T) and longitudinal CDR (CDR_L) for the B-1C, obtained from inelastic SDOF analysis and NTHA. The comparisons were made using sets of 20 wDir (SDC_{mod}) motions in Los Angeles at T_R= 1000 years and 2475 years. In the inelastic SDOF analyses, the ground motions were applied separately to the T- and L- directions. The solid lines represent the inelastic SDOF results over the period range at seven incidence angles, while the cross marks represent the corresponding 3D bridge responses. Results for the B-2C are shown in Figure 2.20. Inelastic CDRs exhibited an increasing trend with respect to the period. The results revealed that the effects of incidence angles on the CDRs were consistent with those observed in the NTHA, where the maximum transverse responses occurred within the 0-45° range, and the maximum longitudinal responses were observed at 90°. Additionally, the CDRs from NTHA were more accurately represented by the inelastic CDRs at shorter periods, which are compatible with the expectation that the periods of the equivalent SDOF systems would be shorter than those of the 3D bridge model. For both bridges, depending on the response direction, inelastic SDOF analyses produced CDRs that were either comparable to or slightly higher than the NTHA results at T_R=1000 years. However, at T_R=2475 years, the inelastic SDOF analyses underestimated the NTHA CDRs. These discrepancies can be attributed to multiple factors. At T_R= 1000 years, the fixed-base SDOF system may overestimate inelastic responses compared to NTHA, as it does not account for foundation flexibility or multi-directional load redistribution, which can reduce displacement demands in the 3D model. In contrast, at T_R=2475 years, increased nonlinearity, multi-directional interactions, period elongation, and P-delta effects in NTHA may lead to larger deformations than the SDOF model predicts, causing underestimation.

Figures 2.21 and 2.22 compare the transverse RDR (RDR_T) and longitudinal RDR (RDR_L) from inelastic SDOF analysis and NTHA, for the B-1C and B-2C, respectively. The results showed that inelastic SDOF analyses significantly underestimated the RDRs compared to the NTHA results. It is well known that RDRs can be highly sensitive to various factors, including material properties and computational models. Additionally, representing the SDOF system as a single mode may fail to capture coupling effects arising from bidirectional loading, as observed in the 3D bridge models. The absence of pinching, ductility, and energy damage parameters in the simplified Takeda hysteretic model further limited its ability to accurately predict residual displacement demand. The results indicate that RDRs are more sensitive to these parameters than CDRs. While calibrating the hysteretic model parameters was outside the scope of this study, incorporating these factors could improve the accuracy of RDR predictions.

Figure 2.23 illustrates the RotD50 CDR ratios of elastic and inelastic SDOF systems to the RotD50 CDR of the B-1C 3D bridge model, using wDir (SDC_{mod}) motions at T_R=1000 years and 2475 years in Los Angeles, and at T_R=1000 years in Oakland. Figure 2.24 depicts the RotD50 CDR ratios of elastic and inelastic SDOF systems compared to the RotD50 CDR of the B-2C bridge, using wDir (SDC_{mod}) motions at T_R=1000 years and 2475 years in Los Angeles. It was observed that, for both bridges, elastic SDOF analyses tended to underestimate the NTHA results for periods below 1.5 seconds, with the underestimation being more significant at shorter periods. Conversely, for periods longer than 1.5 seconds, elastic analyses yielded CDRs that were either comparable to or higher than those from NTHA. This behavior may be attributed to the increasing influence of the superstructure's high axial stiffness in more flexible bridges, which acts to limit longitudinal deformation, an effect that is not captured in simplified SDOF models. For the B-1C, inelastic SDOF analyses slightly overestimated the NTHA CDRs at T_R=1000 years in Los Angeles, but at T_R=2475 years, it underestimated them by 10 to 15%. In Oakland, the inelastic SDOF analysis slightly underestimated the NTHA CDRs. For the B-2C, inelastic SDOF analyses showed a more pronounced underestimation of the NTHA results at T_R=2475 years. These discrepancies highlight the limitations of the inelastic SDOF analysis for capturing the nonlinear dynamic behaviors of the 3D bridge models subjected to pulse-like motions, particularly at higher return periods and for more complex multi-directional effects. Additionally, a comparison of the elastic and inelastic analysis responses between 0.8 and 1.5 seconds revealed that the elastic CDRs were lower than the inelastic CDRs. This indicates that the equal displacement rule (Veletsos and Newmark, 1960) may underestimate inelastic displacement demands, potentially resulting in unconservative estimates. Consequently, relying on the equal displacement rule for ordinary long-span (long-period) bridges in high-seismicity sites may lead to unsafe design practices. These findings support the conclusions of previous studies by Bozorgnia et al. (2010), Bahrampouri et al. (2023), and Zengin et al. (2023).

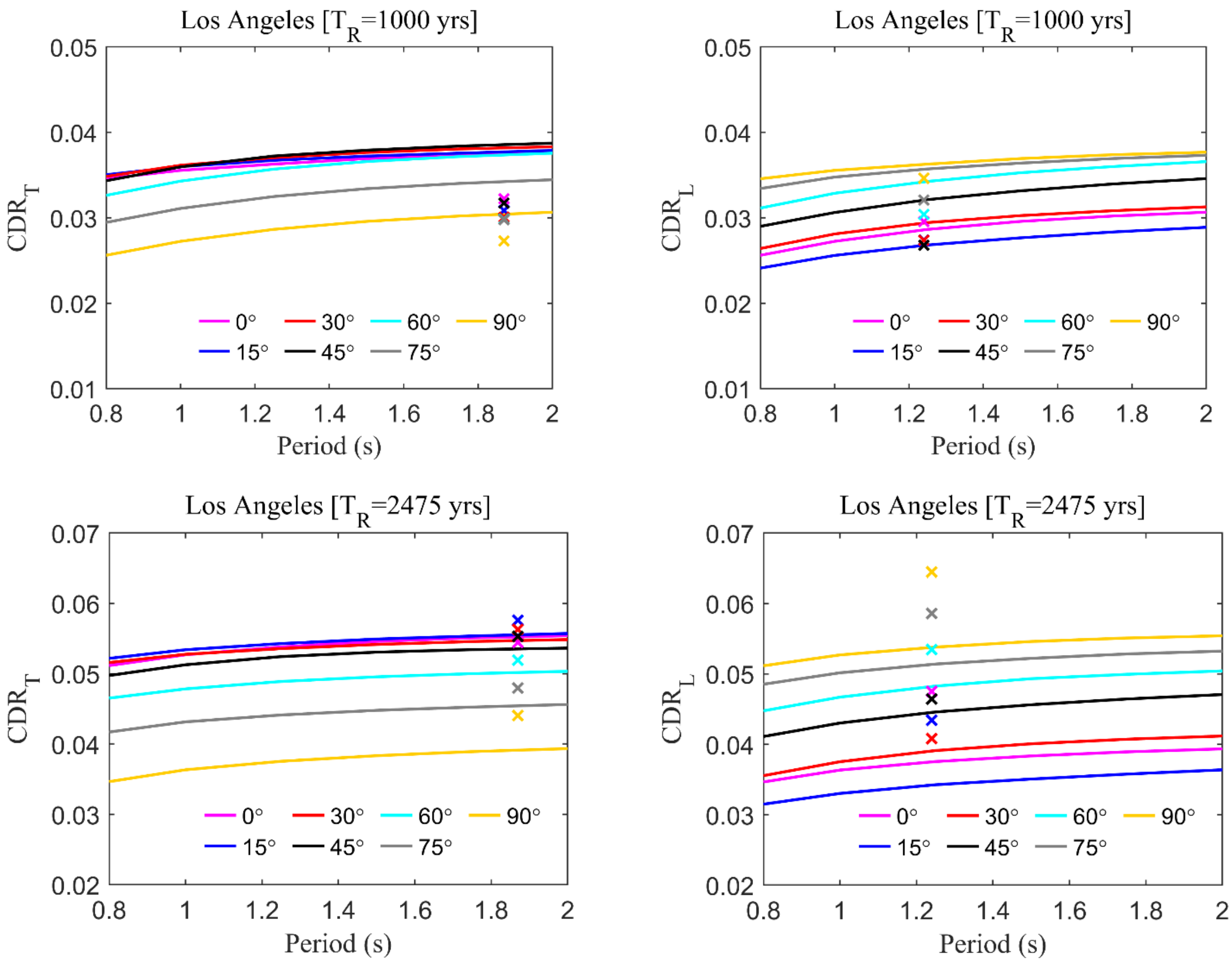

Figure 2-19 *Comparison of transverse (CDR_T) and longitudinal (CDR_L) CDR for the B-1C from inelastic SDOF analysis and NTHA, using 20 wDir (SDC_{mod}) motions at seven different incidence angles, in Los Angeles with T_R = 1000 and 2475 years. Solid lines show inelastic SDOF results, and cross marks represent 3D bridge responses.*

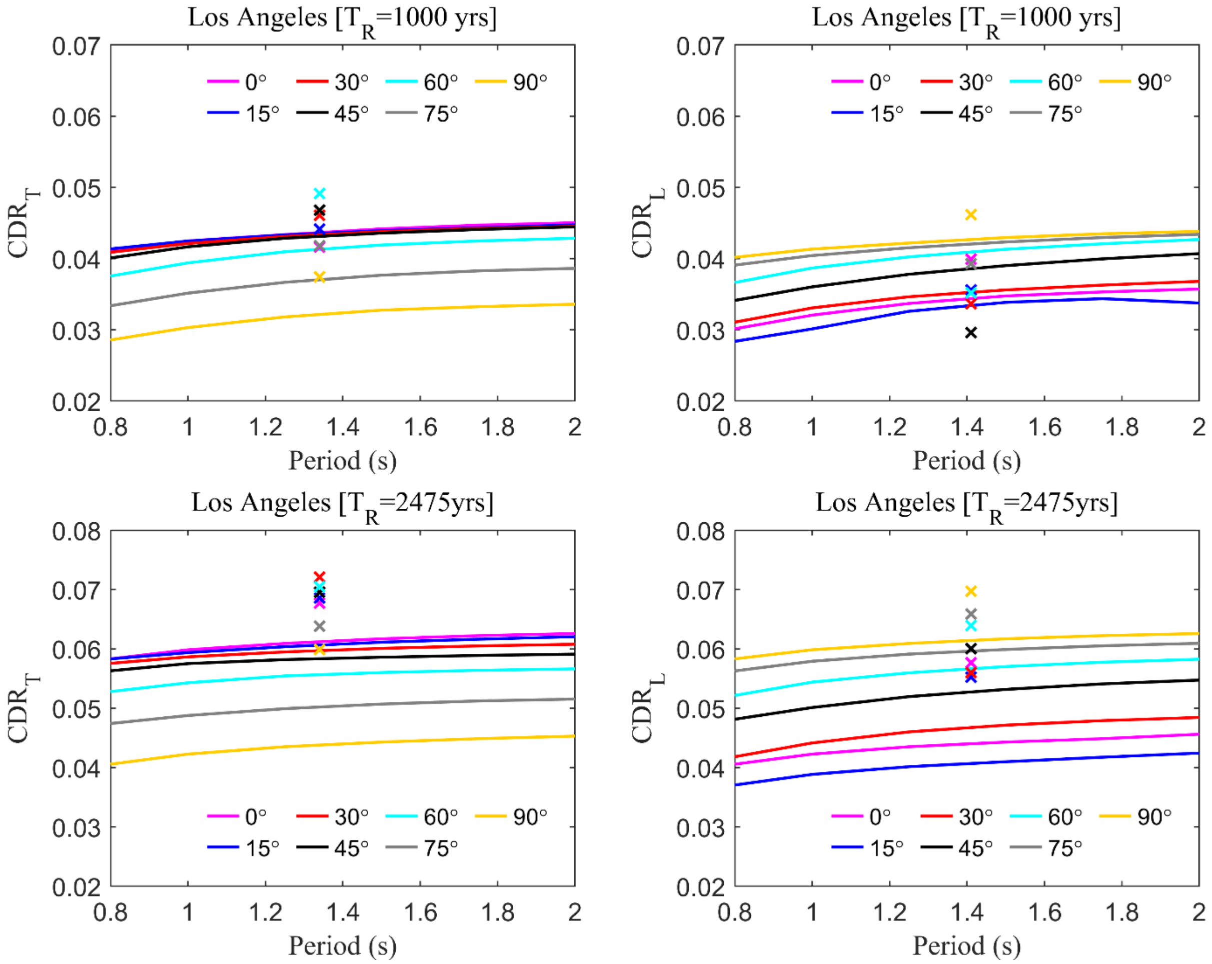

Figure 2-20 *Comparison of transverse (CDR_T) and longitudinal (CDR_L) CDR for the B-2C from inelastic SDOF analysis and NTHA, using 20 wDir (SDC_{mod}) motions at seven different incidence angles, in Los Angeles with T_R = 1000 and 2475 years. Solid lines show inelastic SDOF results, and cross marks represent 3D bridge responses.*

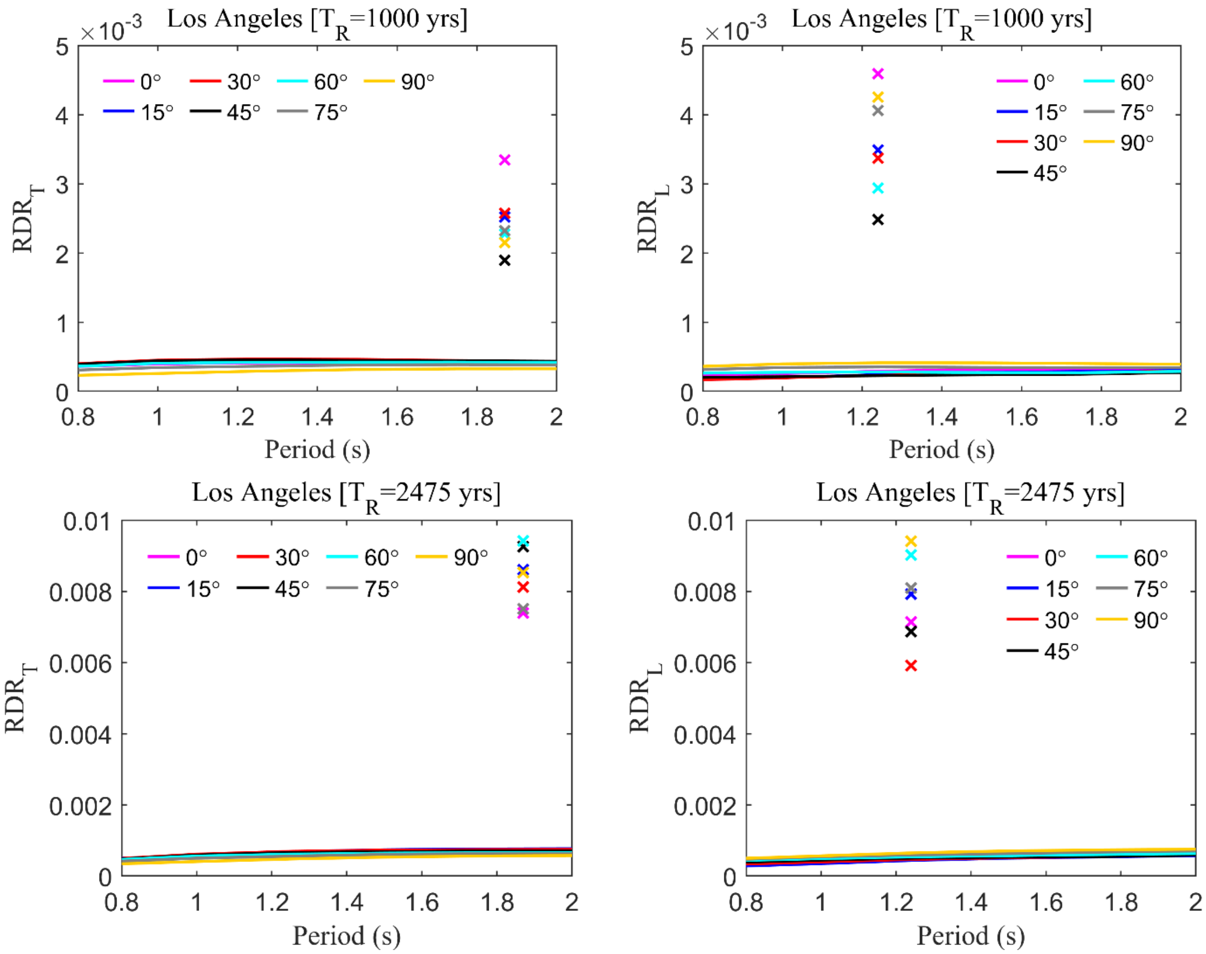

Figure 2-21 *Comparison of transverse (RDR_T) and longitudinal (RDR_L) RDR for the B-1C from inelastic SDOF analysis and NTHA, using 20 wDir (SDC_{mod}) motions at seven different incidence angles, in Los Angeles with T_R = 1000 and 2475 years. Solid lines show inelastic SDOF results, and cross marks represent 3D bridge responses.*

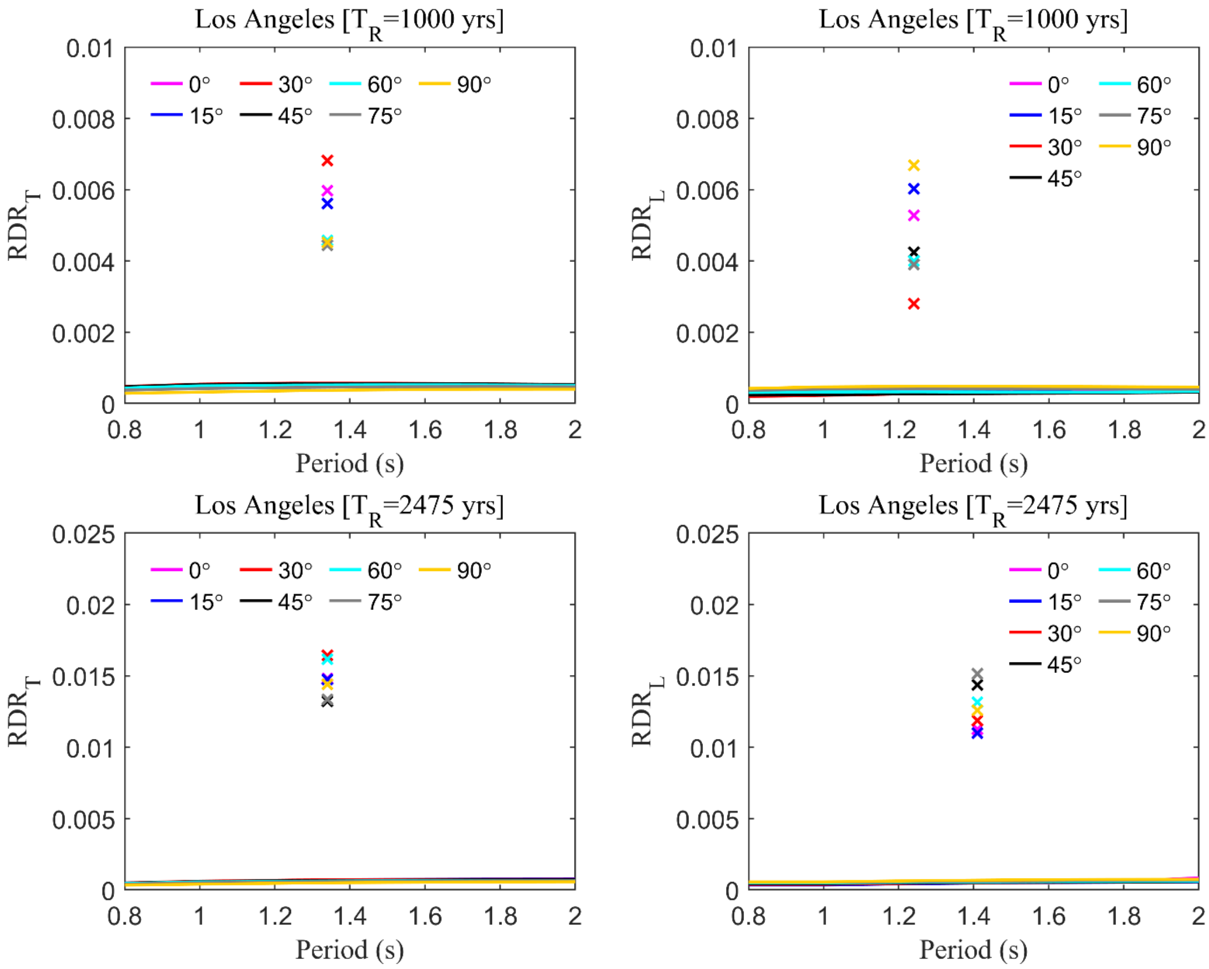

Figure 2-22 *Comparison of transverse (RDR_T) and longitudinal (RDR_L) RDR for the B-2C from inelastic SDOF analysis and NTHA, using 20 wDir (SDC_{mod}) motions at seven different incidence angles, in Los Angeles with T_R = 1000 and 2475 years. Solid lines show inelastic SDOF results, and cross marks represent 3D bridge responses.*

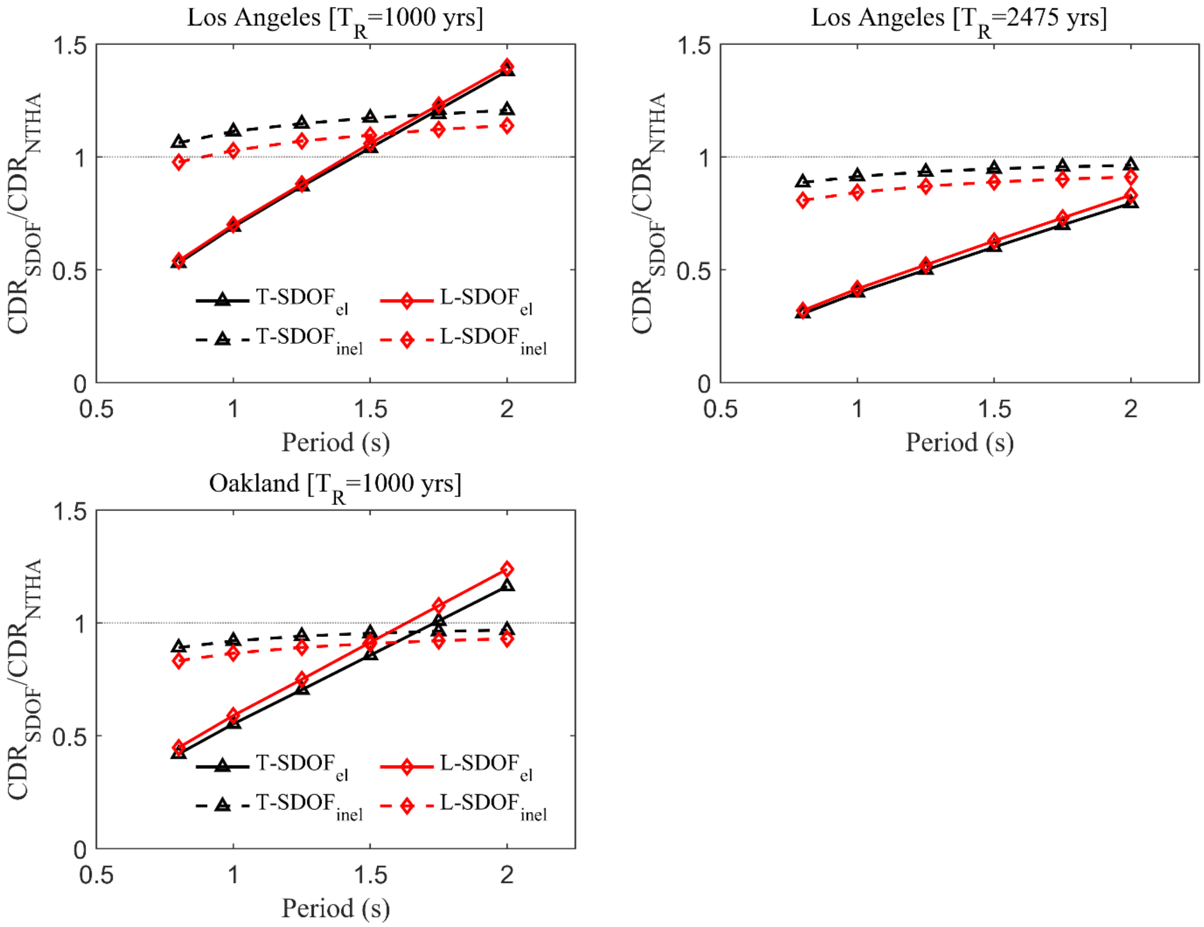

Figure 2-23 *Ratios of the RotD50 CDR from elastic and inelastic SDOF systems to the RotD50 CDR of the* <u>*B-1C*</u> *3D bridge model, using wDir (SDC$_{mod}$) motions at T_R=1000 and 2475 years in Los Angeles, and T_R=1000 years in Oakland.*

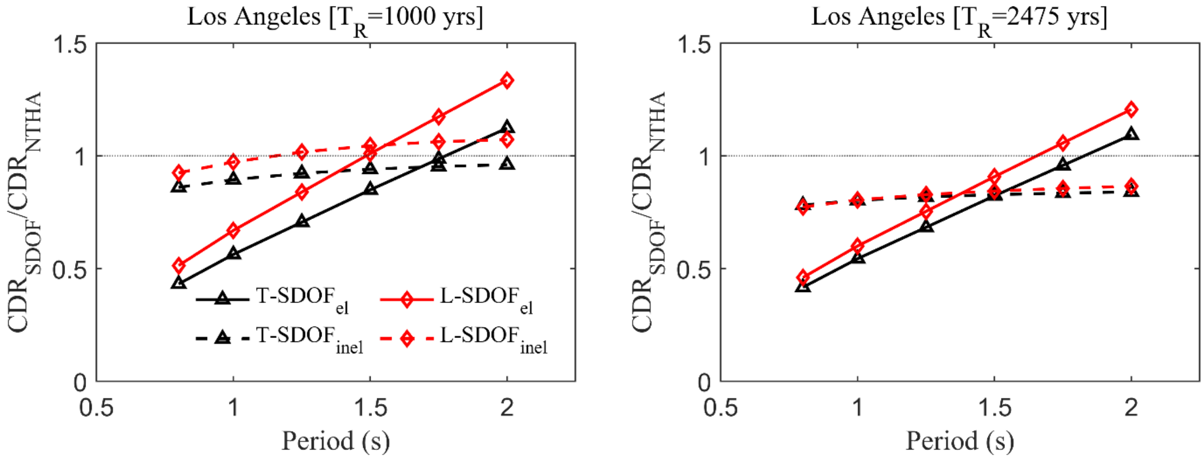

Figure 2-24 *Ratios of the RotD50 CDR from elastic and inelastic SDOF systems to the RotD50 CDR of the* <u>*B-2C*</u> *3D bridge model, using wDir (SDC$_{mod}$) motions at T_R=1000 and 2475 years in Los Angeles.*

2.12. CONCLUSIONS AND RECOMMENDATIONS

This study investigated the effects of ground motion directivity and directionality on the seismic responses of two three-span long-period ordinary bridges, i.e., one-column bent bridge, and two-column bent bridge. Nonlinear time history analyses (NTHA) were performed on both three-dimensional (3D) numerical models using bidirectional ground motions rotated from 0° to 90° in 15° increments. Analyses were conducted using three ground motion sets, i.e., motions without directivity (woDir), with directivity obtained from weighted average of three directivity models (wDir), and modified SDC directivity model (wDir-$\mathrm{SDC}_{\mathrm{mod}}$), at return periods ($T_R$) of 1000 and 2475 years in two sites with varying seismicity: Los Angeles and Oakland.

Responses were evaluated for both transverse (T) and longitudinal (L) directions, and the results revealed that wDir and wDir ($\mathrm{SDC}_{\mathrm{mod}}$) motions produced consistently higher seismic demands compared to woDir motions. The ground motion incidence angle was found to significantly influence response, especially for pulse motions, with maximum displacement ductility demand (μ_D) and column drift ratios (CDRs), and collapse occurrences generally occurring between 0°-45° in the T-direction and at 90° in the L-direction. The results indicated that the interaction between bidirectional ground-motion components and the structural characteristics of the bridges induced torsional responses, which, in turn, might amplify the seismic responses in both the T- and L- directions. A key observation was that CDRs computed at specific incidence angles deviated by 15-35% from those computed using the median CDRs over seven incidence angles, i.e., $\mathrm{CDR}_{\mathrm{RotD50}}$, suggesting that neglecting directional effects could lead to inaccurate estimates of seismic demands. Furthermore, the number of collapses was affected by these directional effects, especially at T_R=2475 years, underscoring the importance of considering directionality in seismic design and assessments. The findings revealed that at high-seismicity sites like Oakland, the two-column bent bridge model lacked sufficient capacity to withstand extreme ground motions. This emphasizes the necessity of site-specific design and analysis to mitigate the risk of severe damage and collapse.

Unlike CDR and μ_D, the residual drift ratios (RDRs) did not demonstrate a clear dependence on the incidence angle. RDRs showed high dispersion, despite average values remaining below the 1% serviceability threshold, 84th percentile RDRs often exceeded it at T_R =2475 years, raising concerns for post-earthquake bridge functionality.

To assess the efficacy of simplified models, inelastic single-degree-of-freedom (SDOF) analyses using Takeda hysteretic model were compared to the NTHA results. The SDOF models incorporated variations in structural period (0.8-2.0 seconds) and used seismic coefficient (Cy) values derived from pushover analyses of the bridges. Results demonstrated that:

- At T_R =1000 years, inelastic SDOF models produced CDRs comparable to or slightly higher than NTHA, particularly at shorter periods. This is likely due to the SDOF model's simplified assumptions, such as fixed-base boundary condition and lack of multidirectional load redistribution. At $T_R = 2475$ years, NTHA CDRs exceeded inelastic SDOF predictions by 10–15%, owing to greater period elongation, bidirectional interaction, and P-delta effects in the 3D bridge models.

- The RDRs from SDOF models underestimated NTHA results. The SDOF systems, particularly those using idealized hysteretic behavior like the Takeda model, were inadequate for capturing residual drift demands, especially under multi-directional loading conditions. Comparisons of elastic vs. inelastic SDOF analyses further revealed that the equal displacement rule may underestimate inelastic displacements, especially for periods shorter than 1.5 seconds, potentially leading to unconservative seismic design.

Incorporating near-fault directivity and ground motion directionality into seismic bridge design is important for improving performance under extreme events. Based on our findings, we recommend that bridges in high-seismicity regions should adopt target spectra with directivity amplification factors, account for ground motion directionality effects, and move beyond simplified SDOF elastic analysis based on the equal displacement rule. Implementing these measures can improve the resilience of bridges subjected to severe ground motions. Future work should investigate the effects of bridge skew angles and 3D ground motion components, including vertical motions, on seismic response and collapse risk.

2.13. REFERENCES

Ancheta, T. D., Darragh, R. B., Stewart, J. P., Seyhan, E., Silva, W. J., Chiou, B. S. J., Wooddell, K. E., Graves, R. W., Kottke, A. R., Boore, D. M., Kishida, T., Donahue, J. L. (2014). PEER NGAWest2 database, Earthquake Spectra 30, 989–1006.

Bahrampouri, M., Bozorgnia, Y., Mazzoni, S., Campbell, K. (2023). Use of Inelastic Response Spectra in Seismic Hazard Analysis and Design. https://doi.org/10.34948/N38G6K.

Bayless, J.R., Somerville, P.G. (2013). Final report of the NGA-West2 directivity working group. Chapter 2, PEER Report No. 2013/09.

Bayless, J.R., Somerville, P.G., Skarlatoudis, A. (2020). A rupture directivity adjustment model applicable to the NGA-West2 ground motion models and complex fault geometries. Final Technical Report: USGS Award G18AP00092.

Bozorgnia, Y., Hachem, M. M., and Campbell, K. W. (2010). Ground Motion Prediction Equation (“Attenuation Relationship”) for Inelastic Response Spectra. Earthquake Spectra 26 (1): 1–23. https://doi.org/10.1193/1.3281182.

Chiou, B.S.J., Spudich, P. (2013). The Chiou and Spudich Directivity Predictor DPP, in Chapter 6 of PEER Report No. 2013/09, Spudich P. (Editor), Pacific Earthquake Engineering Research Center, Berkeley, CA.

Choi, H., Saiidi, M. S., Somerville, P., and El-Azazy, S. (2010). Experimental study of reinforced concrete bridge columns subjected to near-fault ground motions. ACI Structural Journal, 107(1), 3.

Hayden, C. P., Bray, J. D., Abrahamson, N. A. (2014). Selection of near-fault pulse motions. Journal of Geotechnical and Geoenvironmental Engineering, 140(7), 04014030.

JSCE. (2000). Earthquake Resistant Design Codes in Japan. Tokyo, Japan: Japan Society of Civil Engineers, Earthquake Engineering Committee.

Kaviani, P., Zareian, F., Taciroglu, E. (2012). Seismic behavior of reinforced concrete bridges with skew-angled seat-type abutments. Engineering Structures, *45*, 137-150.

Mazzoni, S., McKenna, F., Scott, M. H., and Fenves, G. L. (2006). OpenSees command language manual. Pacific earthquake engineering research (PEER) center, 264(1), 137-158.

Phan, V., Saiidi, M. S., Anderson, J., and Ghasemi, H. (2007). Near-fault ground motion effects on reinforced concrete bridge columns. Journal of structural engineering, 133(7), 982-989

SDC. (2019). Seismic Design Criteria Version 2.0. Sacramento, CA: California Department of Transportation (Caltrans).

Sengupta, A., Quadery, L., Sarkar, S., Roy, R. (2016). Influence of bidirectional near-fault excitations on RC bridge piers. Journal of Bridge Engineering, 21(7), 04016034.

Somerville, P. G., Smith, N. F., Graves, R. W., Abrahamson, N. A. (1997). Modification of empirical strong ground motion attenuation relations to include the amplitude and duration effects of rupture directivity. *Seismological research letters*, *68*(1), 199-222.

Takeda, T., Sozen, M. A., Nielsen, N. N. (1970). Reinforced concrete response to simulated earthquakes. Journal of the structural division, 96(12), 2557-2573.

Torbol, M., Shinozuka, M. (2012). Effect of the angle of seismic incidence on the fragility curves of bridges. Earthquake engineering and structural dynamics, 41(14), 2111-2124.

Veletsos, A. S., a Newmark, N. M. (1960). Effect of inelastic behavior on the response of simple systems to earthquake motions. Department of Civil Engineering, University of Illinois.

Wang, Y., Ibarra, L., Pantelides, C. (2020). Effect of incidence angle on the seismic performance of skewed bridges retrofitted with buckling-restrained braces. Engineering Structures, 211, 110411.

Wei, B., Hu, Z., Zuo, C., Wang, W., Jiang, L. (2021). Effects of horizontal ground motion incident angle on the seismic risk assessment of a high-speed railway continuous bridge. Archives of Civil and Mechanical Engineering, 21, 1-20.

Xie, Y., Zheng, Q., Yang, C. S. W., Zhang, W., DesRoches, R., Padgett, J. E., Taciroglu, E. (2019). Probabilistic models of abutment backfills for regional seismic assessment of highway bridges in California. Engineering Structures, 180, 452-467.

Zengin, E., Abrahamson, N. A. (2020). A vector-valued intensity measure for near-fault ground motions. Earthquake Engineering and Structural Dynamics, 49(7), 716-734.

Zengin, E., Saiidi S., Bozorgnia, Y. (2023). Influence of Ground Motion Selection and Scaling Approaches on Seismic Performance Assessment of Bridges. GIRS-2023-11. https://doi.org/10.34948/N3Z30Q.

Zengin, E., Saiidi, S., Bozorgnia, Y. (2025a). Evaluation of the Impacts of Different Ground Motion Selection and Scaling Approaches on Seismic Performance of Bridges. Journal of Earthquake Engineering, 1-19.

Zengin, E., Bozorgnia, Y., Mazzoni, S., Campbell, K. (2025b). Residual displacement ground-motion model. Soil Dynamics and Earthquake Engineering, 190, 109121.

Zheng, Q. (2021) Advanced seismic risk assessment of california box-girder bridges using emerging modeling techniques and innovative risk models. Georgia Institute of Technology.

Zheng, Q., Yang, C. S. W., Xie, Y., Padgett, J., DesRoches, R., Roblee, C. (2021). Influence of abutment straight backwall fracture on the seismic response of bridges. Earthquake Engineering and Structural Dynamics, 50(7), 1824-1844.

Zhong, J., Jiang, L., Pang, Y., Yuan, W. (2020). Near-fault seismic risk assessment of simply supported bridges. Earthquake Spectra, 36(4), 1645-1669.

APPENDIX 2.A: MODAL ANALYSIS REPORTS

The modal analysis uses the kip–inch–second system. Translational mass is in kip·s²/in; rotational mass (moment of inertia) in kip·in·s². Center of mass is in inches. Eigenvalues are in (rad/s)²; angular frequencies in rad/s; frequencies in Hz; periods in seconds. Modal participation factors are in inches (translations) and radians (rotations). Modal participation masses match total mass units, and modal mass ratios are percentages (%).

MODAL ANALYSIS REPORT (B1-C)

```
 1. DIRECTIONS:

X-Longitudinal, Y-Vertical, Z-Transverse

 2. EIGENVALUE ANALYSIS:
        MODE        LAMBDA        OMEGA     FREQUENCY        PERIOD
 ------------- ------------- ------------- ------------- -------------
             1       11.1682       3.34188      0.531877       1.88013
             2       11.2243       3.35027      0.533212       1.87543
             3       25.5385       5.05356        0.8043       1.24332
             4        29.053       5.39008      0.857858       1.16569

 3. TOTAL MASS OF THE STRUCTURE:
 The total masses (translational and rotational) of the structure
 including the masses at fixed DOFs (if any).
          MX            MY            MZ           RMX           RMY           RMZ
 ------------- ------------- ------------- ------------- ------------- -------------
       28.0719       28.0719       28.0719        412564   1.63023e+08   1.62704e+08

 4. TOTAL FREE MASS OF THE STRUCTURE:
 The total masses (translational and rotational) of the structure
 including only the masses at free DOFs.
          MX            MY            MZ           RMX           RMY           RMZ
 ------------- ------------- ------------- ------------- ------------- -------------
       28.0719       28.0719       28.0719        412564   1.63023e+08   1.62704e+08

 5. CENTER OF MASS:
 The center of mass of the structure, calculated from free masses.
           X             Y             Z
 ------------- ------------- -------------
          4140             0             0
 6. MODAL PARTICIPATION FACTORS:
 The participation factor for a certain mode 'a' in a certain direction 'i'
 indicates how strongly displacement along (or rotation about)
 the global axes is represented in the eigenvector of that mode.
        MODE            MX            MY            MZ           RMX           RMY           RMZ
 ------------- ------------- ------------- ------------- ------------- ------------- -------------
             1             0  -8.05698e-06    7.8522e-08    2.7379e-07       4711.27             0
             2  -4.82252e-05             0      -1.45394      -4.82286   0.000272573     0.0116278
```

```
          3    0.830997            0   3.25108e-05    0.00047924            0      -708.154
          4           0    -0.505302             0             0   -0.0598262             0
```

7. MODAL PARTICIPATION MASSES:

The modal participation masses for each mode.

```
       MODE           MX           MY           MZ          RMX          RMY          RMZ
------------- ------------- ------------- ------------- ------------- ------------- -------------
          1            0            0            0            0   1.57602e+08            0
          2            0            0      13.8731      152.648            0   0.000887316
          3      23.1874            0            0            0            0   1.68387e+07
          4            0      3.08472            0            0    0.0432411            0
```

8. MODAL PARTICIPATION MASSES (cumulative):

The cumulative modal participation masses for each mode.

```
       MODE           MX           MY           MZ          RMX          RMY          RMZ
------------- ------------- ------------- ------------- ------------- ------------- -------------
          1            0            0            0            0   1.57602e+08            0
          2            0            0      13.8731      152.648   1.57602e+08   0.000887316
          3      23.1874            0      13.8731      152.648   1.57602e+08   1.68387e+07
          4      23.1874      3.08472      13.8731      152.648   1.57602e+08   1.68387e+07
```

9. MODAL PARTICIPATION MASS RATIOS (%):

The modal participation mass ratios (%) for each mode.

```
       MODE           MX           MY           MZ          RMX          RMY          RMZ
------------- ------------- ------------- ------------- ------------- ------------- -------------
          1            0   1.64194e-09            0            0      96.6744            0
          2   5.43696e-08            0      49.4199    0.0369998            0   5.45357e-10
          3      82.6001            0   1.26426e-07   1.86925e-09            0      10.3493
          4            0      10.9886            0            0   2.65245e-08            0
```

10. MODAL PARTICIPATION MASS RATIOS (%) (cumulative):

The cumulative modal participation mass ratios (%) for each mode.

```
       MODE           MX           MY           MZ          RMX          RMY          RMZ
------------- ------------- ------------- ------------- ------------- ------------- -------------
          1            0   1.64194e-09            0            0      96.6744            0
          2   5.43696e-08   1.64194e-09      49.4199    0.0369998      96.6744   5.45357e-10
          3      82.6001   1.64194e-09      49.4199    0.0369998      96.6744      10.3493
          4      82.6001      10.9886      49.4199    0.0369998      96.6744      10.3493
```

MODAL ANALYSIS REPORT (B2-C)

```
1. DIRECTIONS:
 X-Longitudinal, Y-Vertical, Z-Transverse

2. EIGENVALUE ANALYSIS:
        MODE        LAMBDA        OMEGA     FREQUENCY        PERIOD
 ------------- ------------- ------------- ------------- -------------
            1      13.2535      3.64053      0.579408        1.7259
            2      19.9421      4.46565      0.710731         1.407
            3      22.0834       4.6993      0.747917       1.33705
            4      40.3824      6.35471       1.01138      0.988744

 3. TOTAL MASS OF THE STRUCTURE:
 The total masses (translational and rotational) of the structure
 including the masses at fixed DOFs (if any).
          MX            MY            MZ           RMX           RMY           RMZ
------------- ------------- ------------- ------------- ------------- -------------
      30.2762       30.2762       30.2762        878711    1.3397e+08   1.33175e+08

 4. TOTAL FREE MASS OF THE STRUCTURE:
 The total masses (translational and rotational) of the structure
 including only the masses at free DOFs.
          MX            MY            MZ           RMX           RMY           RMZ
 ------------- ------------- ------------- ------------- ------------- -------------
      30.2762       30.2762       30.2762        878711    1.3397e+08   1.33175e+08

 5. CENTER OF MASS:
 The center of mass of the structure, calculated from free masses.
           X            Y            Z
 ---------------- ----------------------
         3600            0            0

6. MODAL PARTICIPATION FACTORS:
The participation factor for a certain mode 'a' in a certain direction 'i'
 indicates how strongly displacement along (or rotation about)
 the global axes is represented in the eigenvector of that mode.
        MODE            MX            MY            MZ           RMX           RMY           RMZ
 ------------- ------------- ------------- ------------- ------------- ------------- -------------
            1             0  -1.01383e-08   6.16411e-08   3.37159e-07      -3791.01   3.13986e-06
            2     -0.970077  -1.35186e-08   4.04041e-07   2.57589e-07  -3.34359e-06       274.615
```

```
    3  7.79216e-07           0     1.57413      1.07053  0.000128178  -0.000277089
    4  1.33665e-08   -0.497981           0            0   8.6929e-05  -0.000137209
```

7. MODAL PARTICIPATION MASSES:

The modal participation masses for each mode.

```
        MODE           MX           MY           MZ          RMX          RMY          RMZ
------------- ------------- ------------- ------------- ------------- ------------- -------------
           1            0            0            0            0  1.33458e+08            0
           2      29.2677            0            0            0            0  2.34544e+06
           3            0            0      23.2422      10.7495            0            0
           4            0      3.20959            0            0            0            0
```

8. MODAL PARTICIPATION MASSES (cumulative):

The cumulative modal participation masses for each mode.

```
        MODE           MX           MY           MZ          RMX          RMY          RMZ
------------- ------------- ------------- ------------- ------------- ------------- -------------
           1            0            0            0            0  1.33458e+08            0
           2      29.2677            0            0            0  1.33458e+08  2.34544e+06
           3      29.2677            0      23.2422      10.7495  1.33458e+08  2.34544e+06
           4      29.2677      3.20959      23.2422      10.7495  1.33458e+08  2.34544e+06
```

9. MODAL PARTICIPATION MASS RATIOS (%):

The modal participation mass ratios (%) for each mode.

```
        MODE           MX           MY           MZ          RMX          RMY          RMZ
------------- ------------- ------------- ------------- ------------- ------------- -------------
           1            0            0            0            0      99.6181            0
           2      96.6692            0            0            0            0      1.76117
           3            0            0      76.7672   0.00122333            0            0
           4            0      10.6011            0            0            0            0
```

10. MODAL PARTICIPATION MASS RATIOS (%) (cumulative):

The cumulative modal participation mass ratios (%) for each mode.

```
        MODE           MX           MY           MZ          RMX          RMY          RMZ
------------- ------------- ------------- ------------- ------------- ------------- -------------
           1            0            0            0            0      99.6181            0
           2      96.6692            0            0            0      99.6181      1.76117
           3      96.6692            0      76.7672   0.00122333      99.6181      1.76117
           4      96.6692      10.6011      76.7672   0.00122333      99.6181      1.76117
```

APPENDIX 2.B: LISTS OF SELECTED GROUND MOTIONS

Table B.1. Los Angeles woDir motions (T_R= 1000 years).

RSN	Earthquake name	Year	Station name	M	R_{rup} (km)	Vs_{30} (m/s)	Scale Factor	PGA (g)	PGV (cm/s)
763	Loma Prieta	1989	Gilroy - Gavilan Coll.	6.93	9.96	730	4.68	0.34	27.37
162	Imperial Valley-06	1979	Calexico Fire Station	6.53	10.45	231	4.48	0.24	21.31
5829	El Mayor-Cucapah	2010	RIITO	7.2	13.71	242	2.01	0.39	46.36
1158	Kocaeli, Turkey	1999	Duzce	7.51	15.37	282	1.33	0.32	56.11
4742	Wenchuan, China	2008	Maoxiannanxin	7.9	21.85	430	3.37	0.40	27.25
4740	Wenchuan, China	2008	Maoxiandiban	7.9	22.31	638	5.07	0.33	24.74
164	Imperial Valley-06	1979	Cerro Prieto	6.53	15.19	472	4.00	0.17	15.88
1208	Chi-Chi, Taiwan	1999	CHY046	7.62	24.1	442	2.99	0.17	22.13
4218	Niigata, Japan	2004	NIG028	6.63	9.79	431	2.56	0.65	35.75
163	Imperial Valley-06	1979	Calipatria Fire Station	6.53	24.6	206	6.00	0.10	14.29
4859	Chuetsu-oki	2007	Mitsuke Kazuiti Arita Town	6.8	20.33	274	2.76	0.13	20.10
495	Nahanni, Canada	1985	Site 1	6.76	9.6	605	2.04	1.16	40.41
286	Irpinia, Italy-01	1980	Bisaccia	6.9	21.26	496	3.85	0.08	18.54
754	Loma Prieta	1989	Coyote Lake Dam (Downst)	6.93	20.8	295	4.57	0.16	19.18
1198	Chi-Chi, Taiwan	1999	CHY029	7.62	10.96	545	2.46	0.27	36.09
1116	Kobe, Japan	1995	Shin-Osaka	6.9	19.15	256	2.11	0.23	27.11
4798	Wenchuan, China	2008	Anxiantashui	7.9	0.05	376	2.25	0.25	31.03
988	Northridge-01	1994	LA - Century City CC North	6.69	23.41	278	3.45	0.23	21.98
4881	Chuetsu-oki	2007	Nagaoka Kouiti Town	6.8	20.77	294	3.60	0.19	12.92
5818	Iwate	2008	Kurihara City	6.9	12.85	512	1.97	0.59	48.58

Table B.2. Los Angeles wDir motions (T_R= 1000 years).

RSN	Earthquake name	Year	Station name	M	R_{rup} (km)	Vs_{30} (m/s)	Scale Factor	PGA (g)	PGV (cm/s)	T_p (s)
767	Loma Prieta	1989	Gilroy Array #3	6.93	12.82	350	2.48	0.50	43.52	2.64
723	Superstition Hills-02	1987	Parachute Test Site	6.54	0.95	349	1.06	0.43	102.22	2.39
162	Imperial Valley-06	1979	Calexico Fire Station	6.53	10.45	231	4.68	0.24	21.31	-
1182	Chi-Chi, Taiwan	1999	CHY006	7.62	9.76	438	1.32	0.36	55.82	2.57
68	San Fernando	1971	LA - Hollywood Stor FF	6.61	22.77	316	4.33	0.22	20.47	-
1063	Northridge-01	1994	Rinaldi Receiving Sta	6.69	6.5	282	0.72	0.71	114.40	1.25
1013	Northridge-01	1994	LA Dam	6.69	5.92	629	1.30	0.35	67.13	1.62
1100	Kobe, Japan	1995	Abeno	6.9	24.85	256	4.28	0.21	21.15	-
4228	Niigata, Japan	2004	NIGH11	6.63	8.93	375	2.13	0.51	48.15	1.80
1086	Northridge-01	1994	Sylmar - Olive View Med FF	6.69	5.3	441	0.93	0.64	94.53	2.44
164	Imperial Valley-06	1979	Cerro Prieto	6.53	15.19	472	4.18	0.17	15.88	-
1045	Northridge-01	1994	Newhall - W Pico Canyon Rd.	6.69	5.48	286	1.02	0.36	99.73	2.98
1104	Kobe, Japan	1995	Fukushima	6.9	17.85	256	1.60	0.19	34.17	-
2114	Denali, Alaska	2002	TAPS Pump Station #10	7.9	2.74	329	1.06	0.32	94.23	3.16
828	Cape Mendocino	1992	Petrolia	7.01	8.18	422	1.04	0.62	71.56	3.00
1114	Kobe, Japan	1995	Port Island (0 m)	6.9	3.31	198	0.93	0.32	73.09	2.83
171	Imperial Valley-06	1979	El Centro - Meloland Geot. Array	6.53	0.07	265	1.40	0.31	83.52	3.42
1044	Northridge-01	1994	Newhall - Fire Sta	6.69	5.92	269	0.90	0.65	86.67	1.37
982	Northridge-01	1994	Jensen Filter Plant Administrative Building	6.69	5.43	373	0.70	0.52	97.62	3.16
983	Northridge-01	1994	Jensen Filter Plant Generator Building	6.69	5.43	526	1.03	0.76	68.37	3.54

Table B.3. Los Angeles woDir motions (T_R= 2475 years).

RSN	Earthquake name	Year	Station name	M	R_{rup} (km)	Vs_{30} (m/s)	Scale Factor	PGA (g)	PGV (cm/s)
162	Imperial Valley-06	1979	Calexico Fire Station	6.53	10.45	231	6.00	0.24	21.31
1208	Chi-Chi, Taiwan	1999	CHY046	7.62	24.1	442	4.46	0.17	22.13
1104	Kobe, Japan	1995	Fukushima	6.9	17.85	256	2.28	0.19	34.17
5265	Chuetsu-oki	2007	NIG019	6.8	23.36	372	6.00	0.41	34.12
164	Imperial Valley-06	1979	Cerro Prieto	6.53	15.19	472	5.96	0.17	15.88
1158	Kocaeli, Turkey	1999	Duzce	7.51	15.37	282	1.98	0.32	56.11
5829	El Mayor-Cucapah	2010	RIITO	7.2	13.71	242	2.99	0.39	46.36
4740	Wenchuan, China	2008	Maoxiandiban	7.9	22.31	638	6.00	0.33	24.74
1198	Chi-Chi, Taiwan	1999	CHY029	7.62	10.96	545	3.67	0.27	36.09
1116	Kobe, Japan	1995	Shin-Osaka	6.9	19.15	256	3.14	0.23	27.11
286	Irpinia, Italy-01	1980	Bisaccia	6.9	21.26	496	5.73	0.08	18.54
4742	Wenchuan, China	2008	Maoxiannanxin	7.9	21.85	430	5.02	0.40	27.25
988	Northridge-01	1994	LA - Century City CC North	6.69	23.41	278	5.14	0.23	21.98
1499	Chi-Chi, Taiwan	1999	TCU060	7.62	8.51	375	3.48	0.15	41.86
5818	Iwate	2008	Kurihara City	6.9	12.85	512	2.94	0.59	48.58
4863	Chuetsu-oki	2007	Nagaoka	6.8	16.27	514	2.52	0.31	32.67
4798	Wenchuan, China	2008	Anxiantashui	7.9	0.05	376	3.36	0.25	31.03
1006	Northridge-01	1994	LA - UCLA Grounds	6.69	22.49	398	4.99	0.39	21.99
4859	Chuetsu-oki	2007	Mitsuke Kazuiti Arita Town	6.8	20.33	274	4.12	0.13	20.10
1494	Chi-Chi, Taiwan	1999	TCU054	7.62	5.28	461	3.03	0.17	45.15

Table B.4. Los Angeles wDir motions (T_R= 2475 years).

RSN	Earthquake name	Year	Station name	M	R_{rup} (km)	Vs_{30} (m/s)	Scale Factor	PGA (g)	PGV (cm/s)	T_p (s)
767	Loma Prieta	1989	Gilroy Array #3	6.93	12.82	350	3.72	0.50	43.52	2.64
723	Superstition Hills-02	1987	Parachute Test Site	6.54	0.95	349	1.60	0.43	102.22	2.39
68	San Fernando	1971	LA - Hollywood Stor FF	6.61	22.77	316	6.00	0.22	20.47	-
1104	Kobe, Japan	1995	Fukushima	6.9	17.85	256	2.41	0.19	34.17	-
1086	Northridge-01	1994	Sylmar - Olive View Med FF	6.69	5.3	441	1.40	0.64	94.53	2.44
1114	Kobe, Japan	1995	'Port Island (0 m)'	6.9	3.31	198	1.40	0.32	73.09	2.83
1182	Chi-Chi, Taiwan	1999	CHY006	7.62	9.76	438	1.98	0.36	55.82	2.57
1100	Kobe, Japan	1995	Abeno	6.9	24.85	256	6.00	0.21	21.15	-
982	Northridge-01	1994	Jensen Filter Plant Administrative Building	6.69	5.43	373	1.05	0.52	97.62	3.16
1013	Northridge-01	1994	LA Dam	6.69	5.92	629	1.96	0.35	67.13	1.62
162	Imperial Valley-06	1979	Calexico Fire Station	6.53	10.45	231	6.00	0.24	21.31	-
4207	Niigata, Japan	2004	NIG017	6.63	12.81	274	6.00	0.43	41.13	-
828	Cape Mendocino	1992	Petrolia	7.01	8.18	422	1.56	0.62	71.56	3.00
2114	Denali, Alaska	2002	TAPS Pump Station #10	7.9	2.74	329	1.59	0.32	94.23	3.16
4228	Niigata, Japan	2004	NIGH11	6.63	8.93	375	3.20	0.51	48.15	1.80
171	Imperial Valley-06	1979	El Centro - Meloland Geot. Array	6.53	0.07	265	2.10	0.31	83.52	3.42
1044	Northridge-01	1994	Newhall - Fire Sta	6.69	5.92	269	1.35	0.65	86.67	1.37
983	Northridge-01	1994	Jensen Filter Plant Generator Building	6.69	5.43	526	1.55	0.76	68.37	3.54
1063	Northridge-01	1994	Rinaldi Receiving Sta	6.69	6.5	282	1.09	0.71	114.40	1.25
181	Imperial Valley-06	1979	El Centro Array #6	6.53	1.35	203	1.87	0.45	87.82	3.77

Table B.5. Los Angeles wDir (SDC_{mod}) motions (T_R= 1000 years).

RSN	Earthquake name	Year	Station name	M	R_{rup} (km)	Vs_{30} (m/s)	Scale Factor	PGA (g)	PGV (cm/s)	Tp (s)
723	Superstition Hills-02	1987	Parachute Test Site	6.54	0.95	349	1.11	0.43	102.22	2.40
162	Imperial Valley-06	1979	Calexico Fire Station	6.53	10.45	231	4.88	0.24	21.309	-
1013	Northridge-01	1994	LA Dam	6.69	5.92	629	1.36	0.35	67.133	1.62
68	San Fernando	1971	LA - Hollywood Stor FF	6.61	22.77	316	4.52	0.22	20.472	-
1182	Chi-Chi, Taiwan	1999	CHY006	7.62	9.76	438	1.37	0.36	55.819	2.5
1045	Northridge-01	1994	Newhall - W Pico Canyon Rd.	6.69	5.48	286	1.07	0.36	99.734	2.98
767	Loma Prieta	1989	Gilroy Array #3	6.93	12.82	350	2.58	0.50	43.521	2.64
1100	Kobe, Japan	1995	Abeno	6.9	24.85	256	4.48	0.2	21.151	-
983	Northridge-01	1994	Jensen Filter Plant Generator Building	6.69	5.43	526	1.07	0.76	68.372	3.54
754	Loma Prieta	1989	Coyote Lake Dam (Downst)	6.93	20.8	295	4.98	0.16	19.181	-
2114	Denali, Alaska	2002	TAPS Pump Station #10	7.9	2.74	329	1.11	0.32	94.23	3.16
495	Nahanni, Canada	1985	Site 1	6.76	9.6	605	2.25	1.16	40.405	-
1086	Northridge-01	1994	Sylmar - Olive View Med FF	6.69	5.3	441	0.97	0.64	94.527	2.44
1114	Kobe, Japan	1995	Port Island (0 m)	6.9	3.31	198	0.97	0.32	73.092	2.83
982	Northridge-01	1994	'Jensen Filter Plant Administrative Building'	6.69	5.43	373	0.73	0.52	97.617	3.16
171	Imperial Valley-06	1979	El Centro - Meloland Geot. Array	6.53	0.07	265	1.47	0.3	83.519	3.42
1044	Northridge-01	1994	Newhall - Fire Sta	6.69	5.92	269	0.93	0.65	86.674	1.37
4228	Niigata, Japan	2004	NIGH11	6.63	8.93	375	2.21	0.51	48.15	1.80
181	Imperial Valley-06	1979	El Centro Array #6	6.53	1.35	203	1.30	0.45	87.818	3.77
1119	Kobe, Japan	1995	Takarazuka	6.9	0.27	312	0.95	0.654	72.739	1.81

Table B.6. Los Angeles wDir (SDC_{mod}) motions (T_R= 2475 years).

RSN	Earthquake name	Year	Station name	M	R_{rup} (km)	Vs_{30} (m/s)	Scale Factor	PGA (g)	PGV (cm/s)	T_p (s)
723	Superstition Hills-02	1987	Parachute Test Site	6.54	0.95	349	1.66	0.43	102.22	2.39
767	Loma Prieta	1989	Gilroy Array #3	6.93	12.82	350	3.85	0.50	43.52	2.64
68	San Fernando	1971	LA - Hollywood Stor FF	6.61	22.77	316	6.00	0.22	20.47	-
983	Northridge-01	1994	Jensen Filter Plant Generator Building	6.69	5.43	526	1.60	0.76	68.37	3.54
1114	Kobe, Japan	1995	Port Island (0 m)	6.9	3.31	198	1.45	0.32	73.09	2.83
2114	Denali, Alaska	2002	TAPS Pump Station #10	7.9	2.74	329	1.65	0.32	94.23	3.16
1104	Kobe, Japan	1995	Fukushima	6.9	17.85	256	2.50	0.19	34.17	-
1086	Northridge-01	1994	Sylmar - Olive View Med FF	6.69	5.3	441	1.45	0.64	94.53	2.44
1100	Kobe, Japan	1995	Abeno	6.9	24.85	256	6.00	0.21	21.15	-
1013	Northridge-01	1994	LA Dam	6.69	5.92	629	2.03	0.35	67.13	1.62
1045	Northridge-01	1994	Newhall - W Pico Canyon Rd.	6.69	5.48	286	1.60	0.36	99.73	2.98
495	Nahanni, Canada	1985	Site 1	6.76	9.6	605	3.36	1.16	40.41	-
721	Superstition Hills-02	1987	El Centro Imp. Co. Cent	6.54	18.2	192	3.74	0.26	43.67	-
1182	Chi-Chi, Taiwan	1999	CHY006	7.62	9.76	438	2.04	0.36	55.82	2.57
171	Imperial Valley-06	1979	El Centro - Meloland Geot. Array	6.53	0.07	265	2.19	0.31	83.52	3.42
1044	Northridge-01	1994	Newhall - Fire Sta	6.69	5.92	269	1.39	0.65	86.67	1.37
4228	Niigata, Japan	2004	NIGH11	6.63	8.93	375	3.30	0.51	48.15	1.80
292	Irpinia, Italy-01	1980	Sturno (STN)	6.9	10.84	382	3.03	0.28	52.80	3.27
1119	Kobe, Japan	1995	Takarazuka	6.9	0.27	312	1.42	0.65	72.74	1.81
181	Imperial Valley-06	1979	El Centro Array #6	6.53	1.35	203	1.94	0.45	87.82	3.77

Table B.7. Oakland woDir motions (T_R= 1000 years).

RSN	Earthquake name	Year	Station name	M	R_{rup} (km)	Vs_{30} (m/s)	Scale Factor	PGA (g)	PGV (cm/s)
162	Imperial Valley-06	1979	Calexico Fire Station	6.53	10.45	231	6.00	0.24	21.31
1208	Chi-Chi, Taiwan	1999	CHY046	7.62	24.1	442	4.28	0.17	22.13
4742	Wenchuan, China	2008	Maoxiannanxin	7.9	21.85	430	4.82	0.40	27.25
1198	Chi-Chi, Taiwan	1999	CHY029	7.62	10.96	545	3.53	0.27	36.09
4740	Wenchuan, China	2008	Maoxiandiban	7.9	22.31	638	6.00	0.33	24.74
4859	Chuetsu-oki	2007	Mitsuke Kazuiti Arita Town	6.8	20.33	274	3.92	0.13	20.10
4798	Wenchuan, China	2008	Anxiantashui	7.9	0.05	376	3.21	0.25	31.03
5829	El Mayor-Cucapah	2010	RIITO	7.2	13.71	242	2.88	0.39	46.36
1158	Kocaeli, Turkey	1999	Duzce	7.51	15.37	282	1.88	0.32	56.11
5265	Chuetsu-oki	2007	NIG019	6.8	23.36	372	6.00	0.41	34.12
1494	Chi-Chi, Taiwan	1999	TCU054	7.62	5.28	461	2.89	0.17	45.15
763	Loma Prieta	1989	Gilroy - Gavilan Coll.	6.93	9.96	730	6.00	0.34	27.37
5818	Iwate	2008	Kurihara City	6.9	12.85	512	2.80	0.59	48.58
164	Imperial Valley-06	1979	Cerro Prieto	6.53	15.19	472	5.68	0.17	15.88
4882	Chuetsu-oki	2007	Ojiya City	6.8	23.44	430	6.00	0.29	23.27
495	Nahanni, Canada	1985	Site 1	6.76	9.6	605	2.92	1.16	40.41
286	Irpinia, Italy-01	1980	Bisaccia	6.9	21.26	496	5.46	0.08	18.54
68	San Fernando	1971	LA - Hollywood Stor FF	6.61	22.77	316	5.90	0.22	20.47
1006	Northridge-01	1994	LA - UCLA Grounds	6.69	22.49	398	4.76	0.39	21.99
988	Northridge-01	1994	LA - Century City CC North	6.69	23.41	278	4.90	0.23	21.98

Table B.8. Oakland wDir motions (T_R= 1000 years).

RSN	Earthquake name	Year	Station name	M	R_{rup} (km)	Vs_{30} (m/s)	Scale Factor	PGA (g)	PGV (cm/s)	T_p (s)
723	Superstition Hills-02	1987	Parachute Test Site	6.54	0.95	349	1.54	0.43	102.22	2.39
68	San Fernando	1971	LA - Hollywood Stor FF	6.61	22.77	316	6.00	0.22	20.47	-
767	Loma Prieta	1989	Gilroy Array #3	6.93	12.82	350	3.57	0.50	43.52	2.64
983	Northridge-01	1994	Jensen Filter Plant Generator Building	6.69	5.43	526	1.49	0.76	68.37	3.54
1100	Kobe, Japan	1995	Abeno	6.9	24.85	256	6.00	0.21	21.15	-
982	Northridge-01	1994	Jensen Filter Plant Administrative Building	6.69	5.43	373	1.00	0.52	97.62	3.16
162	Imperial Valley-06	1979	Calexico Fire Station	6.53	10.45	231	6.00	0.24	21.31	-
2114	Denali, Alaska	2002	TAPS Pump Station #10	7.9	2.74	329	1.53	0.32	94.23	3.16
495	Nahanni, Canada	1985	Site 1	6.76	9.6	605	3.12	1.16	40.41	-
721	Superstition Hills-02	1987	El Centro Imp. Co. Cent	6.54	18.2	192	3.48	0.26	43.67	-
1182	Chi-Chi, Taiwan	1999	CHY006	7.62	9.76	438	1.90	0.36	55.82	2.57
292	Irpinia, Italy-01	1980	Sturno (STN)	6.9	10.84	382	2.81	0.28	52.80	3.27
1044	Northridge-01	1994	Newhall - Fire Sta	6.69	5.92	269	1.29	0.65	86.67	1.37
1114	Kobe, Japan	1995	Port Island (0 m)	6.9	3.31	198	1.34	0.32	73.09	2.83
181	Imperial Valley-06	1979	El Centro Array #6	6.53	1.35	203	1.80	0.45	87.82	3.77
4228	Niigata, Japan	2004	NIGH11	6.63	8.93	375	3.07	0.51	48.15	1.80
1013	Northridge-01	1994	LA Dam	6.69	5.92	629	1.88	0.35	67.13	1.62
3746	Cape Mendocino	1992	Centerville Beach, Naval Fac	7.01	18.31	459	2.32	0.45	50.40	1.97
828	Cape Mendocino	1992	Petrolia	7.01	8.18	422	1.48	0.62	71.56	3.00
171	Imperial Valley-06	1979	El Centro - Meloland Geot. Array	6.53	0.07	265	2.04	0.31	83.52	3.42

Table B.9. Oakland wDir (SDC$_{mod}$) motions (T$_R$= 1000 years).

RSN	Earthquake name	Year	Station name	M	R_{rup} (km)	Vs_{30} (m/s)	Scale Factor	PGA (g)	PGV (cm/s)	T_p (s)
723	Superstition Hills-02	1987	Parachute Test Site	6.54	0.95	349	1.54	0.43	102.22	2.39
68	San Fernando	1971	LA - Hollywood Stor FF	6.61	22.77	316	6.00	0.22	20.47	-
767	Loma Prieta	1989	Gilroy Array #3	6.93	12.82	350	3.57	0.50	43.52	2.64
983	Northridge-01	1994	Jensen Filter Plant Generator Building	6.69	5.43	526	1.49	0.76	68.37	3.54
1100	Kobe, Japan	1995	Abeno	6.9	24.85	256	6.00	0.21	21.15	-
982	Northridge-01	1994	Jensen Filter Plant Administrative Building	6.69	5.43	373	1.00	0.52	97.62	3.16
162	Imperial Valley-06	1979	Calexico Fire Station	6.53	10.45	231	6.00	0.24	21.31	-
2114	Denali, Alaska	2002	TAPS Pump Station #10	7.9	2.74	329	1.53	0.32	94.23	3.16
495	Nahanni, Canada	1985	Site 1	6.76	9.6	605	3.12	1.16	40.41	-
721	Superstition Hills-02	1987	El Centro Imp. Co. Cent	6.54	18.2	192	3.48	0.26	43.67	-
1182	Chi-Chi, Taiwan	1999	CHY006	7.62	9.76	438	1.90	0.36	55.82	2.57
292	Irpinia, Italy-01	1980	Sturno (STN)	6.9	10.84	382	2.81	0.28	52.80	3.27
1044	Northridge-01	1994	Newhall - Fire Sta	6.69	5.92	269	1.29	0.65	86.67	1.37
1114	Kobe, Japan	1995	Port Island (0 m)	6.9	3.31	198	1.34	0.32	73.09	2.83
181	Imperial Valley-06	1979	El Centro Array #6	6.53	1.35	203	1.80	0.45	87.82	3.77
4228	Niigata, Japan	2004	NIGH11	6.63	8.93	375	3.07	0.51	48.15	1.80
1013	Northridge-01	1994	LA Dam	6.69	5.92	629	1.88	0.35	67.13	1.62
3746	Cape Mendocino	1992	Centerville Beach, Naval Fac	7.01	18.31	459	2.32	0.45	50.40	1.97
828	Cape Mendocino	1992	Petrolia	7.01	8.18	422	1.48	0.62	71.56	3.00
171	Imperial Valley-06	1979	El Centro - Meloland Geot. Array	6.53	0.07	265	2.04	0.31	83.52	3.42